"Always acknowledge a fault. This will throw those in authority off their guard and give you an opportunity to commit more."

-Mark Twain (1835 - 1910)

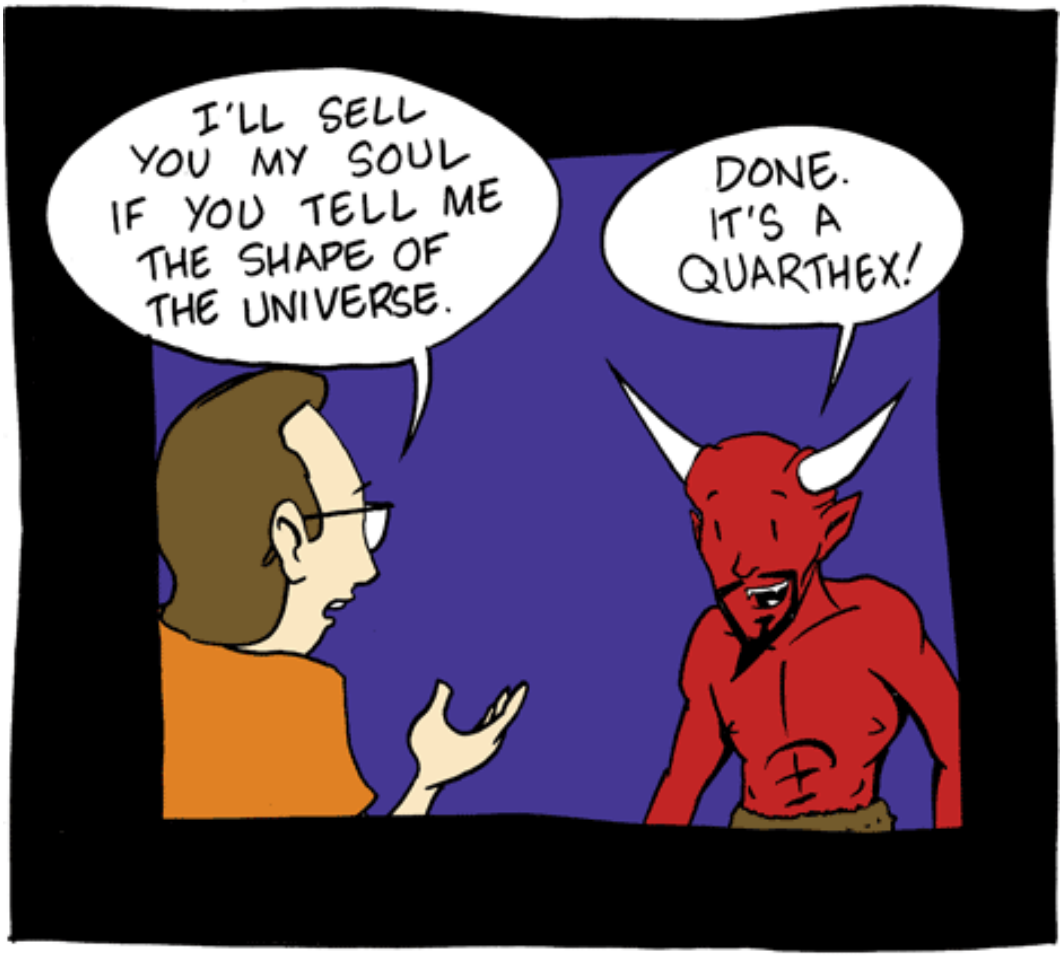

Figure 1: Used with permission of Zach Weinersmith. Taken from `http://www.smbc-comics.com/index.php?id=854`

University of Alberta

Confrontation of CMB data and multiconnected models of constant positive curvature universes

by

Nelson Knutson

A thesis submitted to the Faculty of Graduate Studies and Research
in partial fulfillment of the requirements for the degree of

Master of Science

Department of Physics

Fall 2013
Edmonton, Alberta

Abstract

Multiconnected Universes can possibly explain the low multipole suppression observed in Cosmic Microwave Background data. We compare complete predicted correlation patterns of the temperature fluctuations in the multiconnected models with constant positive curvature to what is observed in WMAP experiment. Likelihood for three models is computed as the function of the curvature which controls the size of the multiconnected Universe relative to distance travelled by CMB photons. As curvature increases from zero for the Universe that is nearly flat and infinite, the size of the multiconnected space becomes smaller than photon horizon. There, predicted correlation patterns change from featureless to more complex. Our analysis gives no evidence for such small topological spaces. During transition likelihood curves for all three investigated spaces show similar features, attributed to the alignment of model correlation patterns to random features in the unique observed CMB realization, and not selective of a specific multiconnected space.

Acknowledgements

We acknowledge the use of the Legacy Archive for Microwave Background Data Analysis (LAMBDA), part of the High Energy Astrophysics Science Archive Center (HEASARC). HEASARC/LAMBDA is a service of the Astrophysics Science Division at the NASA Goddard Space Flight Center. We would like to acknowledge the use of the `HEALPix` software package. We acknowledge the use of the results obtained by the WMAP/NASA science team. Lastly would like to acknowledge Dr. Dmitri Pogosyan, for all the help.

Contents

List of Tables

List of Figures

Chapter 1

Introduction

Modern observations of distant galaxies show us that the Universe is expanding [Hubble 1936]. If we follow this expansion back in time, to the early Universe, we reach an epoch when the Universe was dense and hot. According to the Big Bang theory the Universe began with a singularity at $z = \infty$[1] or at $t = 0$. This changed with the introduction of the idea that the hot Big Bang stage was preceded by the inflationary era of almost exponential expansion, driven in the simplest of models by the vacuum energy of some scalar field. This era is estimated to have happened around $t \approx 10^{-35}s$. The introduction of the inflationary era into the Big Bang model resolves some of the paradoxes that exist, such as the horizon problem, the flatness problem and the magnetic-monopole problem.

Scalar potential fields have quantum fluctuations. During the inflationary era these quantum fluctuations were frozen in and expanded with the space to larger scales, over time these fluctuations formed the perturbations in the matter density that we see today. The evolution and properties of these matter density fluctuations as the Universe continued to expand after inflation, is of particular interest as they contain information about the structure of the Universe. These perturbations are also the seeds for the structure of the distribution of matter that we observe in our Universe today and are imprinted as fluctuations of temperature and polarization into Cosmic Microwave Background Radiation (CMB for short).

At the end of inflation the Universe reheats and subsequently cools adiabatically as it expands. After $t \approx 10^{-3}$ s, once the temperature was at or below $T \sim 10^{13}K$, baryons were able to condense from the quark plasma. The Universe at this time was fully ionized and contained primordial photons. These photons were strongly coupled to the matter through Compton scattering, this strong coupling gave rise to the conception of the photon-baryon fluid, the physics of which are detailed in e.g., [Seager et al. 2000]. This strong coupling explains the perfect blackbody

[1] z is the measure of red-shift $z = \frac{\lambda_{observed} - \lambda_{emited}}{\lambda_{emited}} = \frac{a_{emited}}{a_{observed}}$ where a is the scale factor of the Universe [Carroll 2004].

frequency spectrum of the emitted photons [Fixsen et al. 1996]. Figure 1.1 is the blackbody spectrum of the CMB as measured by the COBE FIRAS experiment. Due to the thermodynamic equilibrium the information about the early Universe is obscured, this is the reason for which the specific processes of that time do not concern us.

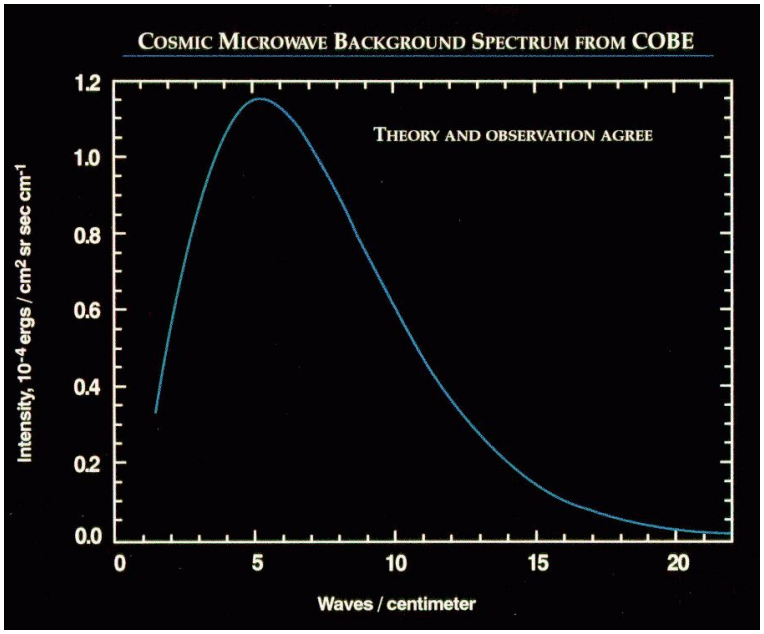

Figure 1.1: The modern observation of the CMB photon emission spectrum as measured by the COBE FIRAS experiment. This graph contains both the data points and the theoretical blackbody curve. The error bars of the data points are smaller than the width of the line of the theoretical blackbody curve, and is why the CMB has one of the best blackbody spectrums ever observed. We would like to acknowledge the NASA science team and LAMBDA for production of image. Taken from `http://lambda.gsfc.nasa.gov/product/cobe/cobe_images/firas_spectrum.jpg`

The evolution of inhomogeneities during this stage is driven by the balance of the pressure provided by the photons and the gravitational force exerted on the matter as it falls into the potential wells. The interplay between these two forces causes near harmonic oscillations similar to a spring in a constant gravitational field [Hu & Dodelson 2002]. The oscillations behave like standing acoustic waves [Hu & White 1996], where their spectrum is well understood and left an imprint on the CMB and in the distribution of the matter that we see in the Universe today, called baryon acoustic oscillations (BAO) [Beutler et al. 2011]. The analysis of these acoustic like oscillations is used to determine the cosmological parameters of the Universe. This methodology is analogous to sand on the surface of a vibrating drum, [Luminet 2006] by analyzing the density patterns of the sand we can determine the properties such as the tension and the density of the drum head, even its shape. Strong coupling of the photons to the matter, means that

the density fluctuations are represented as the temperature fluctuations of the photons for the CMB sky.

As the Universe continued to expand it eventually reached a temperature of $T \approx 3000$, at this time the ions and electrons could combine to form neutral atoms, this is called the time of recombination and occurred at around a redshift of $z \approx 1000$,[2]. Ionized hydrogen combines to become atomic hydrogen at $T \approx 10000K$ but this is just an energy estimation and does not include the effect that there are 10^9 photons per baryon at that time. As such when this and other physical effects are incorporated we obtain a more physical value of $T \approx 3000$, the physics of this decoupling is described in, e.g., [Seager et al. 2000]. When the ions formed neutral atoms the photons were no longer strongly coupled to the matter. The decoupling of the photons allowed their travel throughout the Universe virtually unimpeded. These photons are emitted from what is called the horizon of last scattering, and form what we observe as the Cosmic Microwave Background Radiation.

1.1 Temperature Fluctuations

The temperature fluctuations that we see on the sky are actually the combination of two effects on the photons. The first is the temperature fluctuations that existed at the time of recombination and the second is the interactions that the photon experiences as it traveled across the visible Universe to the observer. This section will briefly go over some of the basics of how the temperature fluctuations are created and how the cosmological parameters of the Universe affect their observed temperature, ending with the equation that we use in the analysis of the Universe's topology. This section is intended as a simple overview, for a more in-depth exposition of the theory of CMB fluctuations see, e.g., [Hu 1996; Hu & White 1996] and the references therein.

Two components are required to analyze the physics of the perturbations in the plasma of the early universe. Kinetic theory, which focuses on the transport of the photons through the perturbed space, and perturbation theory, which is used to determine the evolution of these fluctuations. The perturbed metric of the Universe is given as follows in spherical comoving coordinates,

$$ds^2 = a^2(\eta)\left[(1+2\Phi)d\eta^2 - (1-2\Psi)(d\chi^2 + S_k^2(\chi)d\Omega^2)\right] \tag{1.1}$$

$$\begin{aligned} S_k(\chi) &= R_0 \sin(\chi/R_0)\,, & k &= +1 \\ &= \chi\,, & k &= 0 \\ &= R_0 \sinh(\chi/R_0)\,, & k &= -1 \end{aligned}$$

[2] $T(z) = T(z=0)(1+z), \Rightarrow T(1000) \approx 3.0K \times 1000$

R_0 is the curvature of the 3-space, a is the scale factor of expansion, χ is the radial comoving distance and $d\eta = dt/a(t)$ is the conformal time. Ψ describes the perturbations in spatial curvature, and Φ is the Newtonian potential field.

From the kinetic theory we have the Boltzmann equation [Hu & Dodelson 2002].

$$\left[\frac{\partial}{\partial\eta} + \frac{\partial x^i}{\partial\eta}\frac{\partial}{\partial x^i} + \frac{\partial\gamma^i}{\partial\eta}\frac{\partial}{\partial\gamma^i}\right]\Theta = S_g + S_s \quad , \tag{1.2}$$

x^i is the i'th component of the position, γ^i is the i'th component of the directional unit vector of the photon's momentum, and $\Theta(\eta, \mathbf{x}, \gamma) = \frac{\Delta T}{T}$ are the temperature fluctuations. S_g and S_s are the source functions from the gravitational and scattering effects respectively, these source functions contain the physics that affects the observed temperature of the photons.

The anisotropies that we observe are small, as such we can approximate the evolution of these fluctuations to the first linear order. The photon distribution is a uniform blackbody [Fixsen et al. 1996] and the lack of distortions in the blackbody spectrum confirms that the approximation to first order is valid [Hu & Dodelson 2002]. As in General Relativity there is a certain gauge freedom, we need to specify a relation between the idealized unperturbed background space-time and our perturbed physical space-time. Though the final observables are gauge independent, there is a subtlety here which means the gauge has to be fixed before calculations can proceed. Two popular gauge choices are the free falling synchronous gauge and the longitudinal gauge, which can be more physically intuitive. For details on the gauge choice and effects see, e.g., [Hu 1996]. This discussion occurs in the longitudinal gauge, which is also known as the Newtonian gauge.

The first order evolution equation for the Fourier component k of the photon temperature in a flat space is given by [Hu 1996].

$$\frac{d}{d\eta}(1+R)\dot{\Theta}_0 + \frac{k^2}{3}\Theta_0 = -\frac{k^2}{3}(1+R)\Psi - \frac{d}{d\eta}(1+R)\dot{\Phi} \tag{1.3}$$

Θ_0 is the locally isotropic (monopole with respect to the photon's momentum) temperature fluctuation in the electron's frame, $R = \frac{3\rho_B}{4\rho_\gamma}$ is the measure of baryon to photon ratio. The dot represents the derivative with respect to the conformal time and we have set the speed of light $c = 1$.

This equation is similar to the equation for a driven harmonic oscillator with an effective mass $m_{eff} = (1 + R)$. To visualize these fluctuations, for sufficiently high k we can neglect the slow time variation of R, Ψ and Φ. Then, using that $s = \sqrt{\frac{dP_\gamma}{d(\rho_b+\rho_\gamma)}} = \frac{1}{\sqrt{3(1+R)}}$ is the speed of sound we obtain,

$$\ddot{\Theta}_0 + k^2 s^2 \Theta_0 = -\frac{k^2}{3}\Psi \quad . \tag{1.4}$$

This is the equation for a simple oscillator in a constant gravitational field, and has the following solution,

$$\Theta_0(\eta) = [\Theta_0(0) + (1+R)\Psi]\cos kr_s + \frac{1}{ks}\dot{\Theta}_0(0)\sin kr_s - (1+R)\Psi \tag{1.5}$$

$r_s \approx s\eta$, which is the sound horizon. Perturbations beyond the size of the sound horizon are not acoustical oscillations, at these large scales these perturbations are the frozen perturbations that originate from the scalar field during the inflationary era. The initial values $\Theta_0(0)$ and $\dot{\Theta}_0(0)$ are set in very early Universe, when the scales of all the relevant perturbations were much larger than the horizon.

Using the photon continuity equation we can similarly obtain for the local dipole term Θ_1 in the temperature, due to electron velocity,

$$\Theta_1(\eta) = 3[\Theta_0 + (1+R)\Psi]s\sin kr_s + \frac{3}{k}\dot{\Theta}_0(0)\cos kr_s \tag{1.6}$$

Equations 1.5 and 1.6 contain all the effects that dominate the anisotropies before recombination also known as primary anisotropies [Hu 1996]. We ignore the dipole effects as these only come into play at smaller scale anisotropies.

The first effect we will analyze is only the effect due to the falling down a gravitational well. In the early Universe was radiation dominant $\Rightarrow R \approx 0$. The perturbations that follow the growing adiabatic mode are frozen outside the horizon that corresponds to $\dot{\Theta}_0(0) = 0$. The solution in the equation 1.5 then becomes $\Theta_0(\eta) = [\Theta_0(0) + \Psi]\cos kr_s - \Psi$. The last term $-\Psi$ is simply a blue or red shift that occurs when light falls into or climbs from the potential well. We are interested in the effective temperature fluctuations $\Theta_{eff} = \Theta_0 + \Psi$, that is the temperature fluctuations that incorporates this frequency shift experienced by the light as it escapes the potential well.

$$[\Theta_0 + \Psi](\eta) = [\Theta_0(0) + \Psi]\cos kr_s$$

During the matter dominated epoch $[\Theta_0 + \Psi](\eta_m) = \frac{1}{3}\Psi(\eta_m)$ (in a large scale limit, η_m is some late time moment in matter dominated epoch) [Sachs & Wolfe 1967]. The solution then becomes $[\Theta_0 + \Psi](\eta) = \frac{1}{3}\Psi(\eta_m)\cos kr_s$. These oscillations are acoustic standing waves, therefore we can look at their spectrum, which is the square of the amplitude as the function of k, at any particular time. When $\cos kr_s = 1$ or -1 we see that $[\Theta_0 + \Psi](\eta)$ is at a maximum or minimum, respectively, while when $\cos kr_s = 0$ effective temperature fluctuations vanish. The peaks in our spectrum occur at $k = \frac{\pi}{s\eta}$ at time η, thus are the modes of maximum compression and maximum rarefaction for the odd and even peaks respectively.

Changing the baryon density ratio will affect the spectrum. All terms are affected for equation 1.3, except for the pressure term. The solution in the limit of constant R is then [Hu & Dodelson 2002],

$$[\Theta_0 + (1+R)\Psi](\eta) = [\Theta_0(0) + (1+R)\Psi](\eta_m)\cos kr_s$$

Changing the ratio changes the sound horizon r_s, due to the change in the speed of sound s, as such we can expect a shift in the spectrum. Analogous to adding mass to the end of a spring, our oscillations will have a larger amplitude due to this increased effective mass. The effective temperature fluctuation being $\Theta + \Psi$ we will obtain a shift in the equilibrium position from $\Theta = -\Psi$ to $\Theta = -(1+R)\Psi$, this shift is not symmetric. As such we see an enhancement of the compression modes in the well, and thus only every other peak in our spectrum is enhanced [Hu 1996]. These results also hold even when R is not in the limit of being varied constantly in time [Hu & Dodelson 2002].

The change in the equation of state as Universe expands causes the potential wells to change in time. When Universe transitions from radiation to matter domination and from matter to Λ-term domination, potential wells shallow out. This shallowing of the wells provides a driving effect for the oscillations, because the wells are shallower when the photons climb out, as to when they fell in, this is the $\dot{\Phi}$ term in equation 1.5. During the recombination epoch, that is near to radiation-matter transition, this effect shuts off faster the larger the amount of dark matter there exists. Incorporating all the previous effects with this, a high third peak in the spectrum is a good indication of dark matter dominance [Hu & Dodelson 2002].

The photon-baryon fluid is not prefect, as it has viscosity and heat conduction [Hu & Dodelson 2002]. These imperfections contribute to an overall dampening effect on our spectrum. The exponential dampening is on the order of $e^{-\frac{k^2\eta}{\dot{\tau}}}$, where $\dot{\tau} \equiv n_e \sigma_T a$ is the differential Thomson optical depth.

All the effects discussed previously are in the pre-recombination photon-baryon plasma epoch. There are effects that occur after recombination that affects the temperature fluctuation spectrum. Just after the time of recombination we have what is called the early Integrated-Sachs-Wolfe (ISW) effect. This is from the shallowing of the potential wells as the Universe completes the change from radiation to matter domination after the time of last scattering.

The late ISW effect is similar the early ISW effect and is also caused by the time varying potential perturbations. The difference is that these occur when the Universe becomes dark energy dominated, which leads to decay of potential perturbations. This only effects large scales (small l) because as the photons travel through the visible Universe they travel through many peaks and valleys of the smaller scale potential modes, over the time scale of these potential perturbations. Generally the temperature fluctuations at higher l will not be greatly affected by the late ISW effect and the effect at low l is at the level of only a few percent.

We know from our observations of the Universe today that the intergalactic gas is ionized, this reionization had to occur no later than $z \approx 6.5$ or before Universe was $t \approx 1$ billion years old. Therefore our spectrum will be dampened at the

higher mode frequencies, but since the gas is so rarefied there is no additional acoustic oscillation effects on the temperature fluctuations [Hu & Dodelson 2002].

The last effects are from foreground sources and their gravitational lensing. These are non-Gaussian due to their origin and can cause great problems for data analysis. Some sources can be dealt with by comparing to x-ray maps and simply masking out the affected areas. In fact this method was used to first determine if the observed anisotropies seen by COBE were caused by foreground emission of hot gasses [Boughn & Jahoda 1993]. This is the primary reason why most data analysis of the CMB is done with a mask of these foreground objects and regions.

Let us look at the expected power spectrum in more detail. Our first peak is the first compression mode, second peak is the first rarefaction mode, the third peak is the second compression mode, and so on and, and so forth. Figure 1.2 shows the effect of varying an individual parameter on the power spectrum and figure 1.3 is a schematic of how the cosmological parameters individually affect the power spectrum and the combined final outcome.

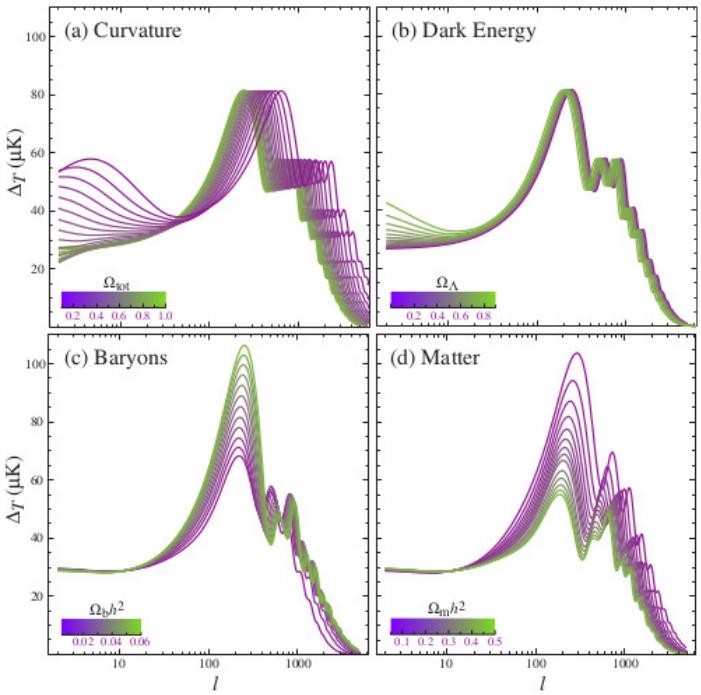

Figure 1.2: Visual representation of how the power spectrum changes as an individual cosmological parameter is varied. Image from [Hu & Dodelson 2002], Plate:4

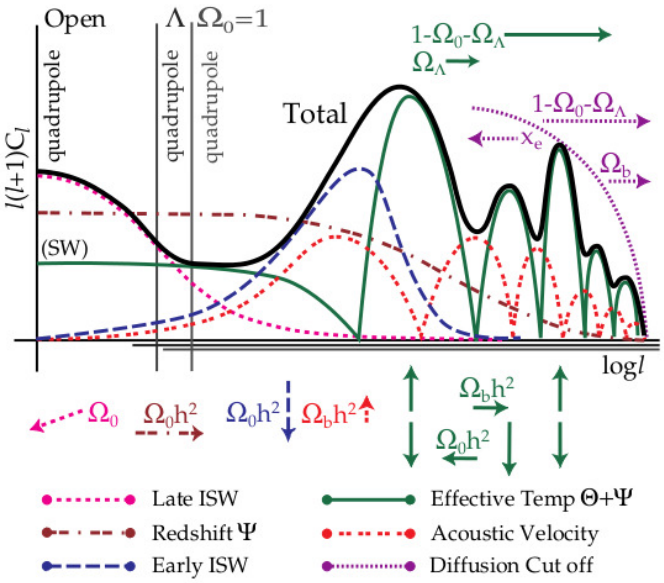

Figure 1.3: A schematic of how varying different cosmological parameters affects the CMB power spectrum. Image from [Hu 1996], Fig:8

1.1.1 Equation for the Temperature Fluctuations

We will be dealing with the signal smoothed over large angular scales, which limit us to the Sachs-Wolfe $k \to 0$ regime for temperature fluctuations. In the Sachs-Wolfe regime we can separate the time and space component of the potential $\Phi(\eta, \mathbf{x}) = D(\eta)\Phi(\eta_H, \mathbf{x})$, where the time dependence of the growing mode of perturbations is in $D(\eta)$ normalized to $D(\eta_H) = 1$. It is worth noting that for hydrodynamic matter $\Phi = -\Psi$, which is the assumption made about the photon-baryon plasma. The other assumption that we have in our calculation of the anisotropies, is that we ignore higher local moments of photon distribution, as these affect only modes of higher spatial frequencies. We also assume that the time of recombination was instantaneous, a valid approximation for the lower frequency modes. The complete equation that is used to calculate the temperature fluctuations is equation 1.7 [Bond et al. 2000b].

$$\boxed{\frac{\Delta T}{\bar{T}}(\hat{\mathbf{q}}) = \frac{1}{3}\Phi(\chi\hat{\mathbf{q}})|_{\chi=\chi_H} + 2\int_0^{\chi_H} \dot{D}(\chi)\Phi(\chi\hat{\mathbf{q}})e^{-\tau_{reion}(\chi)}\, d\chi} \tag{1.7}$$

$\hat{\mathbf{q}}$ is the unit vector that points to a position on the sky, χ is the comoving distance along the line of sight such that χ_H is the comoving distance to the last scattering surface. Time-dependent functions $\dot{D}(\chi)$ and $\tau_{reion}(\chi)$ are evaluated at the time moment $\eta = \eta_0 - \chi$ when the photon is at the radial distance χ, η_0 being the present time. We remark that the moment of last scattering is $\eta_H = \eta_0 - \chi_H$. $\bar{T}$ is the mean temperature of the CMB map. It is worth

noting that these temperature fluctuations are at large scale and as such are not acoustical oscillations as they are larger that the sound horizon at the time of recombination. These temperature fluctuations originated from the perturbations in the potential field caused by the vacuum fluctuations of the scalar field at the inflationary epoch.

1.2 The Power Spectrum

In the previous section we saw how to compute the temperature fluctuation for a point on the sky in the direction $\hat{\mathbf{q}}$, at large scales. However it is multiplied by a random amplitude, set at inflation, and its comparison with observed sky can be done only statistically. The correlation function is defined as the average product of the temperature fluctuations in two directions.

$$C(\hat{\mathbf{q}}, \hat{\mathbf{q}}') = \langle \Delta T(\hat{\mathbf{q}}) \Delta T(\hat{\mathbf{q}}') \rangle \tag{1.8}$$

On the other hand we can decompose these temperature fluctuations into spherical harmonics.

$$\Delta T_{lm} = \int \Delta T(\hat{\mathbf{q}}) Y_{lm}(\hat{\mathbf{q}}) \, d\hat{\mathbf{q}} \tag{1.9}$$

and define the covariance matrix $\mathbf{C_{lml'm'}}$, calculated the following way,

$$C_{lml'm'} = \langle \Delta T_{lm} \Delta T^*_{l'm'} \rangle \quad . \tag{1.10}$$

$C_{lml'm'}$ and $C(\hat{\mathbf{q}}, \hat{\mathbf{q}}')$ are related through spherical harmonic decomposition.

$$C_{lml'm'} = \int C(\hat{\mathbf{q}}, \hat{\mathbf{q}}') Y_{lm}(\hat{\mathbf{q}}) Y^*_{l'm'}(\hat{\mathbf{q}}') \, d\hat{\mathbf{q}} \, d\hat{\mathbf{q}}' \tag{1.11}$$

Our fluctuations are homogeneous as such there is no cross correlation between lm modes, $C_{lml'm'} = C_{lm}\delta_{ll'}\delta_{mm'}$. C_{lm} is called the power spectrum. If in addition we have statistical isotropy, the correlation function will depend only on the angle between two directions $\cos\theta = \hat{\mathbf{q}} \cdot \hat{\mathbf{q}}'$ and the power spectrum in turn will depend only on l and not on m.

$$C_l = \frac{2l+1}{4\pi} \int C(\cos\theta) P_l(\cos\theta) \, d(\cos\theta) \tag{1.12}$$

The angular brackets $\langle \ \rangle$ represent a statistical average over an ensemble of all possible realizations of the CMB, but we only have one sky and thus only one realization. Therefore how do we obtain the ensemble average? There are essentially two procedures. Compute the correlation function then convert to the power spectrum or to first decompose the temperature fluctuations into spherical harmonics then calculate the power spectrum.

We start with our data map of temperature values on the sky $T(\hat{\mathbf{q}})$. The CMB is very uniform and is a perfect blackbody with an average temperature according to its blackbody spectrum of $\bar{T} = (2.72548 \pm 0.57)K$ [Fixsen 2009]. The temperature fluctuations are $\Delta T(\hat{\mathbf{q}}) = T(\hat{\mathbf{q}}) - \bar{T}$. The dipole of the temperature fluctuations is removed as it is dominated by our motion relative to the CMB. The temperature fluctuations that remain in the map after the dipole removal are small and in the $0.1mK$ range, these temperature fluctuations can be seen in figure 1.6.

If the temperature fluctuations are homogeneous, then $C(\hat{\mathbf{q}}, \hat{\mathbf{q}}') = C(\Delta_{\theta\phi})$, where $\Delta_{\theta\phi}$ is the directional difference of the two points on sky, such that $\hat{\mathbf{q}}' = \hat{\mathbf{q}} + \Delta_{\theta\phi}$. Therefore $\mathbf{C}$ is only a function of directional difference between the two directions, and we can estimate our correlation function by marginalizing over all points that have this same directional difference $\Delta_{\theta\phi}$.

$$C(\Delta_{\theta\phi}) = \frac{1}{4\pi} \int \Delta T(\hat{\mathbf{q}}) \Delta T(\hat{\mathbf{q}} + \Delta_{\theta\phi}) \, d\hat{\mathbf{q}} \tag{1.13}$$

If the temperature fluctuations are in addition isotropic, we have no dependence on the direction provided by $\Delta_{\theta\phi}$, as such $C(\hat{\mathbf{q}}, \hat{\mathbf{q}}') = C(\cos\theta)$, $\cos\theta = \hat{\mathbf{q}} \cdot \hat{\mathbf{q}}'$. Therefore to improve the estimate we further marginalize so that there is only the dependence on the angle between $\hat{\mathbf{q}}$ and $\hat{\mathbf{q}}'$.

$$C(\cos\theta) = \frac{1}{16\pi^2} \int \int \Delta T(\hat{\mathbf{q}}) \Delta T(\hat{\mathbf{q}}') \delta(\cos\theta - \hat{\mathbf{q}} \cdot \hat{\mathbf{q}}') \, d\hat{\mathbf{q}} \, d\hat{\mathbf{q}}' \tag{1.14}$$

Now we estimate the power spectrum in lm space. We start with the power spectrum $C_{lm} = |\Delta T_{lm}|^2$ for the homogeneous field. If the field is isotropic the estimation of the power spectrum is accomplished by averaging over the respective m values.

$$C_l = \frac{1}{2l+1} \sum_{m=-l}^{l} C_{lm} \tag{1.15}$$

This estimation is how the correlation function from the data of observed sky is often obtained [Szapudi et al. 2001]. From the CMB data's power spectrum we can reconstruct the cosmological parameters of the Universe. The power spectrum modes are independent allowing the comparison of a model to the data be a simple modification of the χ-squared test. This is one of the greatest strengths of power spectrum analysis.

Masks are difficult to deal with in power spectrum analysis. For they can cause cross correlation of modes which are more significant for masks that are more extended and irregular. To solve this Monte-Carlo simulations can be run on many theoretical CMB sky realizations based on a known power spectrum to determine a correction. In real space for the correlation function, the advantage is there is no issue in dealing with a mask. In fact masks are quite simple as the points that are masked are simply ignored when computing the marginalisation.

The downside is that there can be strong correlation between different length scales $\Delta_{\theta\phi}$, thus comparing results to theory can be complicated.

For the most part CMB analysis is done using the power spectrum, but for our purposes this is not appropriate. We cannot assume isotropy of our Universe, as such the power spectrum would be at the homogeneous estimation stage only. We are interested in the lower l modes as such with out the marginalisation of m we would have significantly larger error due to the lack of points to sample over at these large scales. There remains the possibility that the multiconnected space may also break homogeneity which would further complicate the use of the power spectrum.

Figure 1.4 shows the power spectrum for the 7-year WMAP dataset that is compared with the theoretical predictions in figure 1.2. The gray band shows the cosmic variance ΔC_l, which is an intrinsic uncertainty in our measurements, this is from the fact that we have only one realization of our CMB to observe.

$$\Delta C_l = \sqrt{\frac{2}{2l+1}} C_l \tag{1.16}$$

As we approach smaller l this corresponds to larger modes on the sky, the number of points therefore to sample for each mode is reduced significantly and the cosmic variance grows. For the quadrupole $l = 2$ we have an error of $\pm C_l \sqrt{\frac{2}{5}}$, i.e over 60%. The monopole and dipole terms of our spectrum are not considered in the analysis on the CMB. Though the anisotropies will have monopole and dipole terms, it is impossible to distinguish them from the the mean temperature offset and our motion through space relative to the CMB respectively.

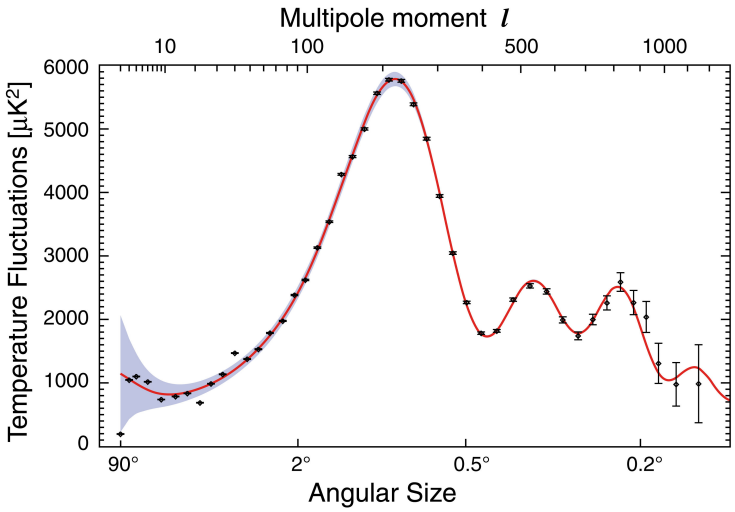

Figure 1.4: 7-year WMAP measured power spectrum. The gray shadow represents the cosmic variance, note that it is inversely proportional to l. Image from `http://wmap.gsfc.nasa.gov/media/111133/111133_7yr_PowerSpectrumL.jpg`, courtesy of the NASA/WMAP science team

1.3 Discovery and Observation of the CMB

In 1964-1965, A.A. Penzias and R.W. Wilson set out to analyze noise in radio antennae. Much to their surprise they actually discovered something far more profound. After taking into account Ohmic loss, atmospheric absorption and back-lobe response[3] an unaccounted for temperature of $(3.5 \pm 1.0)K$ at $4080MHz$ was detected [Penzias & Wilson 1965]. Using the temperature for known common radio sources determined by other researchers and their own data, they determined that this signal did not originate from some unaccounted for known radio source, but from something new. They determined that this signal is isotropic, unpolarized and is not affected by the seasonal variations. What they did not know at that time was that this signal is the CMB.

It was theorized that the Universe either began from a singularity, or that the Universe oscillates in size from a very small to large sizes for all eternity, this means that the early Universe is expected to be hot [Gamow 1948; Alpher & Herman 1948]. Either way the Universe, at some point the Universe had to reach a temperature in excess of $10^{10}K$,[4] [Dicke et al. 1965]. It was accepted that the early Universe was hot as it did also explain the $\approx 25\%$ He produced

[3]In directional antennae there are two main regions of signal strength front-lobe: the signal strength in the direction you want the signal to propagate and back-lobe the signal strength propagating in the opposite direction

[4]If the universe was a cycle then a temperature of $10^{10}K$ is required so that the mater from the previous cycle is decomposed into basic baryons. As a singularity the Universe will be dense at the beginning with $T \gg 10^{10}K$

through early nucleosynthesis [Carroll 2004]. P.G. Roll and D.T. Wilkinson set out to detect this radiation from the early Universe and were in the process of constructing a radiometer and horn, set to measure at $\lambda = 3cm$, when A.A. Penzias and R.W. Wilson discovered the CMB [Dicke et al. 1965]. In theory this radiation had to have a $T \leq 40K$ [Dicke et al. 1965] based on the value of the Hubble constant and that is what A.A. Penzias and R.W. Wilson measured. Unfortunately the data from the CMB at that time was not able to determine the curvature of the Universe.

Further experiments were done to measure any anisotropies in the CMB [Partridge 1988][5], but other than just the dipole [Smoot et al. 1977], no other anisotropies were observed [Smoot et al. 1990]. In 1989 a satellite called the Cosmic Background Explorer (COBE for short) was launched into orbit to gather a full sky map of the CMB for both temperature variations (DMR) and the frequency spectrum (FIRAS) [Boggess et al. 1992]. COBE's data provided the first definitive detection of anisotropies in the CMB, other than that from just the dipole [Smoot et al. 1992]. Unfortunately it did not have a high resolution as it had an experimental beam of around FWHM $\approx 7^\circ$ (to a resolution of around $l \approx 25$,[6]) and a sensitivity of around $\Delta T \approx 0.15mK(rms)$ [Boggess et al. 1992]. Many experiments were done that later confirmed these results [White et al. 1994]. Out of these experiments two of the more famous of them were MAXIMA and BOOMERanG[7].

MAXIMA and BOOMERanG were both high altitude balloon based experiments that observed a high resolution section of the sky [Rabii et al. 2006; de Bernardis et al. 1999]. BOOMERanG[8] consisted of two flights one in 1998 and the other in 2003, they both measured a high resolution map having a beam of around (12 to 20 $arcmin$) [de Bernardis et al. 1999]. This confirmed and was able to determine with more precision, the cosmological parameters due to this higher resolution of the smaller temperature fluctuation modes [MacTavish et al. 2006]. MAXIMA[9] mapped a high resolution section of the sky as well [Rabii et al. 2006]. Though the experimental runtime was shorter than BOOMERanG, some interesting properties such as gaussianity were examined along with a check for the results obtained by other experiments[10]. In 2001 the Wilkinson Microwave Anisotropy Probe (WMAP) was launched, this provided the next highest resolution full sky map available. WMAP has a beam width of FWHM = (0.88, 0.66, 0.51, 0.35 and 0.22)$^\circ$, and a sensitivity of $\Delta T \approx 35\ \mu K$ at a pixel size of

[5]Read this paper to get information on the state of the CMB experiments at 1988

[6]Resolution in $l \approx \frac{180^\circ}{res(FWHM)}$, this is a crude estimate of the potential beam resolution in lm space to which they can observe

[7]For a list of all CMB observation experiments and their information can be obtained from the LAMBDA website: `http://lambda.gsfc.nasa.gov/product/expt/`

[8]`http://cmb.phys.cwru.edu/boomerang/`

[9]`http://cfpa.berkeley.edu/group/cmb/`

[10]MAXIMA publication page `http://cosmology.berkeley.edu/group/cmb/comp_publications.html`

$0.3^\circ \times 0.3^\circ$ [NASA/WMAP Science Team 2010]. This allowed WMAP to reach a resolution of around $l \approx 820$.

The next highest resolution full sky map is from the *Planck* satellite launched in 2009. This satellite is producing the highest resolution full sky temperature maps of the CMB anisotropies. *Planck* has a beam size of FWHM= (33.16, 28.09 and 13.08) *arcmin* for LFI,and FWHM= (9.59, 7.18, 4.87, 4.7, 4.73 and 4.51) *arcmin* for HFI. The sensitivity of LFI is $\frac{\Delta T}{T}$ = (2.0, 2.7, and 4.7) 10^{-12} at a resolution of (33, 24, 14) *arcmin* respectively, and for HFI $\frac{\Delta T}{T}$ = (5.0, 3.1, 14.7, 147 and 6700) 10^{-12} at a resolution of 5.0 *arcmin* [The Planck Collaboration 2005; Planck Collaboration et al. 2013a]. This will most definitely be the last high sensitivity and resolution ($l \approx 2400$), full sky temperature intensity map, as the new exciting area of research on the CMB is in its polarization. The polarization is not of much interest to us, due to the computational requirements and there is no real advantage in using it. The polarization is expected to contain interesting information, one of the most interesting being the proof of primordial gravitational waves though no definitive discovery of them has yet been made. Figure 1.5, 1.6 and 1.7 are foreground reduced maps of the CMB from the three different full sky satellites experiments to date. Note that 1.5, is not from the COBE satellite, due to its low resolution it is not possible to obtain a full sky foreground reduced map, hence we used the WMAP map but degraded to the resolution as seen by COBE.

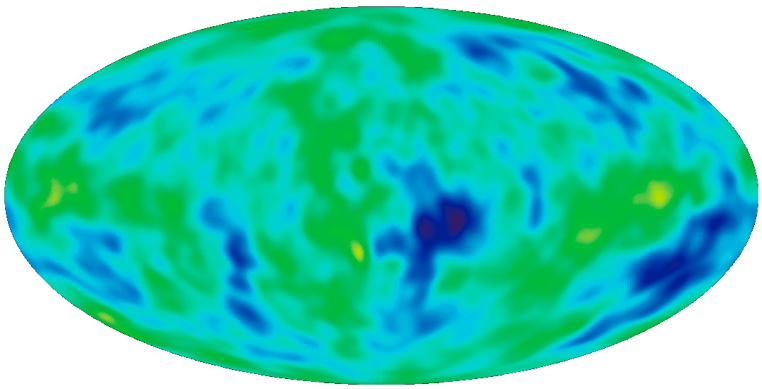

Figure 1.5: Full sky map of the temperature anisotropies at the resolution of COBE taken from the WMAP data, this is done because there is no foreground reduced noise map for the COBE satellite. The map uses the same temperature scale as WMAP (fig:1.6). Image is from `http://map.gsfc.nasa.gov/media/030653/030653_1_1280.png`, courtesy of NASA/WMAP science team.

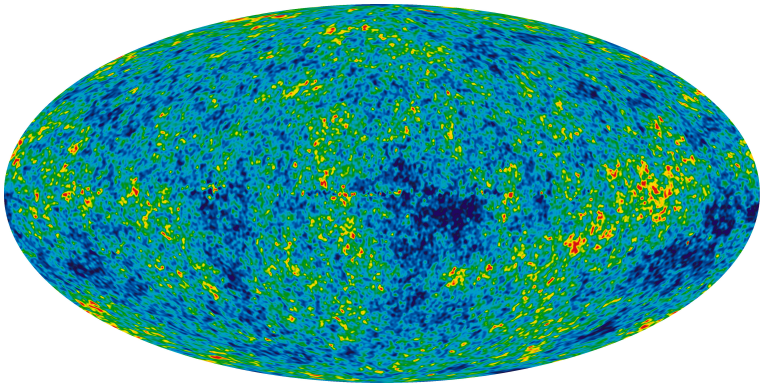

Figure 1.6: Full sky map of the temperature anisotropies from the nine year WMAP data, this is a foreground noise reduced map with a temperature scale of $\pm 200mK$. Image is from `http://lambda.gsfc.nasa.gov/product/map/current/map_images/9yr_4096/ilc_9yr_temp_4096.png`, courtesy of NASA/WMAP science team.

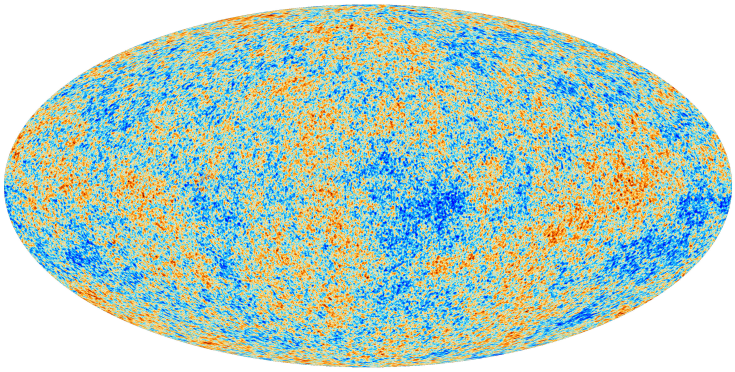

Figure 1.7: Full sky map of the temperature anisotropies from the *Planck* satellite, this is a foreground noise reduced map. Image is from `http://spaceinimages.esa.int/var/esa/storage/images/esa_multimedia/images/2013/03/planck_cmb/12583930-4-eng-GB/Planck_CMB.jpg`, courtesy of the ESA and the *Planck* Collaboration

1.4 Shape of the Universe

The main purpose in this investigation is to analyze possible shapes of the Universe, but what do we mean by shape, which is a rather general term? The shape of the Universe can be separated into two components, the geometry of the Universe's 3-space and its topology.

1.4.1 Geometry

Since Euclid formally defined flat space, around 300 BC, mathematicians have been searching for a contradiction of his famous fifth postulate[11]. It was not until in the early 1800's that mathematicians discovered the hyperbolic space that contradicts this postulate, however they could not determine if we lived in this space or not.

In 1909 Einstein postulated general relativity, where the field equations of general relativity are used to described the geometry of space from its energy densities. General relativity only describes the local geometry and does not describe the shape of the Universe as a whole. In 1922, A. A. Friedmann applied Einstein's field equations to the homogeneous model of the Universe, this gave a first real glimpse into the possibilities and conditions under which the Universe would have a non-Euclidean geometry. Friedmann's equations relate the curvature of the space to the density of matter and expansion rate of the Universe,

$$H(t)^2 \equiv \left(\frac{\dot{a}}{a}\right)^2 = \frac{8\pi G}{3c^2}\epsilon(t) - \frac{\kappa c^2}{a^2\mathcal{R}_0^2} \tag{1.17}$$

G is the gravitational constant, H is the Hubble constant, $\mathcal{R}_0$ is the current curvature radius of the 3-space, and $\epsilon(t)$ is the energy density of the Universe. Assuming curvature is the same everywhere due to homogeneity, there are essentially only three global geometries, open, flat, and closed described by the value of $\kappa = -1$, $\kappa = 0$ and $\kappa = +1$ respectively. Out of these three possibilities only one is intrinsically finite in size and that is the closed space. The two curved 3-spaces are also called hyperbolic (open) and spherical (closed). In hyperbolic spaces parallel geodesics tend to diverge, where as in spherical spaces they tend to converge, or it can be thought of in terms of triangles, where the sum of its angles in a closed space is $\geq 180°$ and in an open space is $\leq 180°$, see the figure 1.8. This is one of the earliest relations used in trying to determine if the Universe has a curvature.

The observed Universe is surprisingly isotropic and homogeneous, thus it is assumed in the first approximation to be described by the Friedmann-Lemaître-

[11]Have two geodesics l m and a geodesic t crossing both l and m forming the angles ϕ and θ both on the same side with reference to t, if $\phi + \theta < 180°$, then l and m will intersect on the same side as the angles of t.

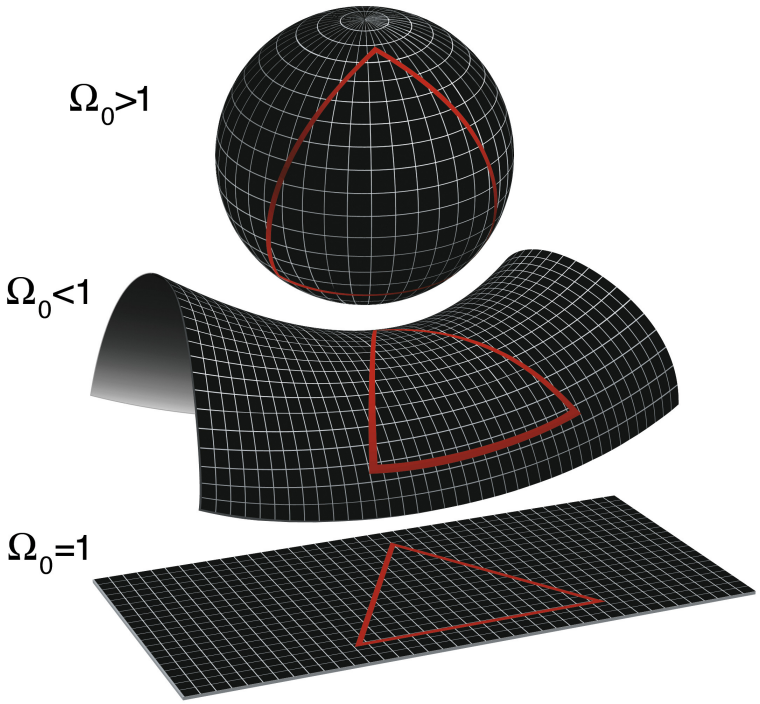

Figure 1.8: The three spacial geometries as predicted by the Friedmann-Lemaître metric. Notice the triangles and how the angles are "bowed" in the curved spaces. The top geometry is the closed, the middle is the hyperbolic and the last is the flat. Image from `http://map.gsfc.nasa.gov/media/990006/9900062048.jpg`, courtesy of the NASA/WMAP science team

Robertson-Walker metric given by the unperturbed part of equation (1.1). This constitutes the standard model of the Universe. In this model we can describe the curvature in terms of the parameter known as the curvature density Ω_k.

$$\Omega_k = 1 - \Omega(t) = -\frac{\kappa c^2}{\mathcal{R}_0^2 a(t)^2 H(t)^2} \tag{1.18}$$

$\Omega(t)$ is the ratio of the density in the Universe to the critical density which is the density for the space to be flat.

$$\Omega(t) = \frac{\epsilon(t)}{\epsilon_c(t)} \ , \quad \epsilon_c(t) \equiv \frac{3c^2}{8\pi G} H(t)^2 \tag{1.19}$$

Similarly, the Ω_i parameters are defined for individual energy components that fill the Universe.

Modern measurement of CMB temperature anisotropies provide the best to date estimates for the main cosmological parameters, especially when combined with other measurements such as the distribution of galaxies at large scales (BAO). Cosmological parameters obtained by fitting the WMAP 9-year data are summarized in Table 1.1.

Table 1.1: The Cosmological Parameters from the WMAP 9-year Data Set [Hinshaw et al. 2012].

Parameters	9-Year WMAP Only	WMAP+eCMB+BAO
Ω_k	$-0.037^{+0.044}_{-0.042}$	$-0.0049^{+0.0041}_{-0.0040}$
Ω_{tot}	$1.037^{+0.044}_{-0.042}$	$1.0049^{+0.0041}_{-0.0040}$
Ω_m	$0.19 < \Omega_m < 0.95$ (95%CL)	0.292 ± 0.010
Ω_Λ	$0.22 < \Omega_\Lambda < 0.79$ (95%CL)	0.713 ± 0.011
t_0 (Gyr)	14.8 ± 1.5	13.99 ± 0.17
H_0 $(km/s/Mpc)$	$38 < H_0 < 84$ (95%CL)	68.0 ± 1.0

eCMB uses information obtained by other CMB sky experiments, BAO is from the baryon acoustic oscillations.

This shows that CMB data alone allows the spatial geometry of our Universe to be either flat or curved. Combining CMB data with Large-Scale-Structure datasets highly prefers nearly flat spaces, but with a slight positive curvature.

With our focus on a multiconnected positively curved Universe, let us quote here geometrical characteristics of the Universe with 9-year WMAP only parameters and $\Omega_k = -0.037$. The distance to the last scattering surface is $\chi_{\rm LSS} = 2.8239 \frac{c}{H_0}$, and the curvature radius of the 3-sphere is $R_0 = 5.1988 \frac{c}{H_0}$, therefore,
$\chi_{\rm LSS} = 0.5432 \ R_0$.

$$V_{\mathbb{S}^3} = 2\pi^2 R_0^3 = 2773.569 (\frac{c}{H_0})^3, \quad V_{\rm LSS} = \frac{4}{3}\pi \chi_{\rm LSS}^3 = 94.327 (\frac{c}{H_0})^3$$

$$\Rightarrow \frac{V_{\text{LSS}}}{V_{\mathbb{S}^3}} = 0.034$$

$$C_{\mathbb{S}^3} = 2\pi R_0 = 32.665\frac{c}{H_0}$$

$$\Rightarrow \frac{2\chi_{\text{LSS}}}{C_{\mathbb{S}^3}} = 0.173$$

From these values we are seeing only about 3.4% of the volume of the Universe if it is just $\mathbb{S}^3$, but 17.3% of the circumference of the Universe, which is quite impressive for a seemingly small value of Ω_k. By introducing a compactification we can potentially introduce a case where we are close to viewing 100% of the Universe.

1.4.2 Multiconnected topology

Though the Friedmann-Lemaître metric does describe the geometry of the 3-space, it contain no information about, nor is it affected by the introduction of some sort boundary condition on the 3-space. Similarly Einstein's field equations are local and are not affected by imposing a compactification of the space, though this does not mean that this compactification will not affect the boundary conditions on the physical fields that evolve in such space. The introduction of a compactification is given in the simplest terms as a periodic boundary condition creating what is called the fundamental domain, which is a set of points of the space that are unique.

A multiconnected space, is a space where for any point x in the fundamental domain, there exists at least one loop l that can not be continuously shrunk down to the single point x. Any function along such loop will be periodic. For example take a square of length a with a periodic boundary condition, for simplicity let us take the point at coordinates (x, y), the origin being at the center of the square. Take a line and run it to the edge of the square at $(x, a/2)$, and $(x, -a/2)$ this created a loop that runs through point x, but can not be continuously shrunk to a single point at x. This is because it passes through our boundary condition[12].

It is easier to deal with a tiling of images of the fundamental domain ($\mathcal{M}$) over the 3-space, this set of all tiles is called our universal covering space ($\mathcal{M}^u$). Our universal covering space is simply connected, meaning that we can take any loop l that passes through point x contained in the 3-space and continuously shrink it to the point x. It is simpler to deal with a tiling on the universal covering space because it is an isotropic and homogeneous space, as described by our Friedmann-Lemaître metric. Figure 1.9 shows how this tiling functions, a particle traveling along the curved line is seen entering and leaving the individual image domains, when dealing with only the fundamental domain and not using the universal covering space it can be quite inconvenient.

[12]This is the popular example of a loop that goes around a 2-torus

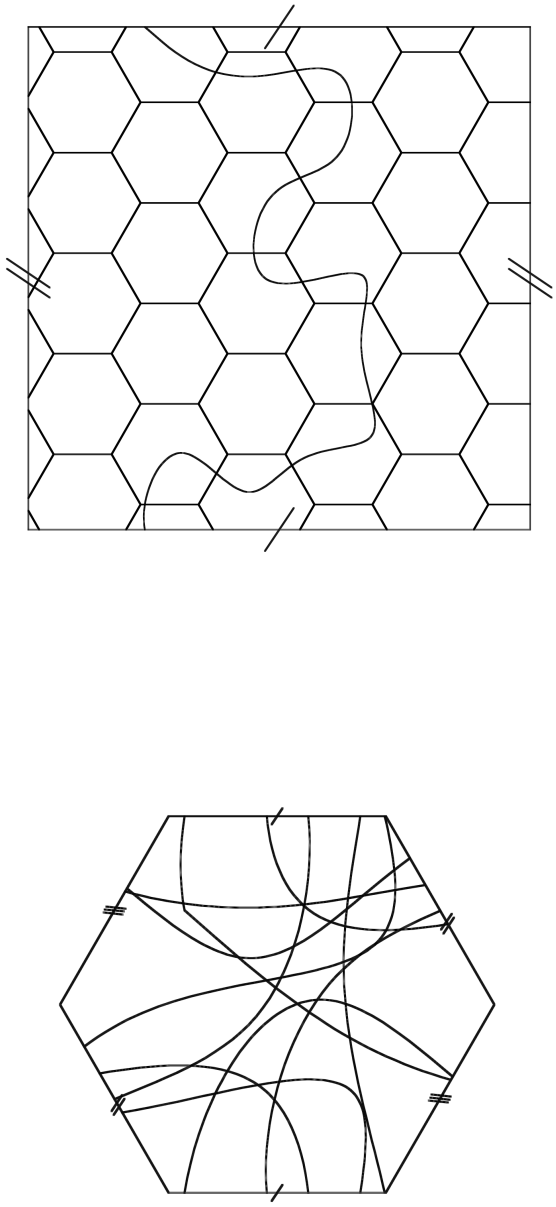

Figure 1.9: The top panel is the universal cover $\mathbb{R}^3$ tiled by hexagons. The line is a particle trail in the flat space. The bottom image is the trail as seen using the periodic boundary conditions of the fundamental domain.

How do we construct our fundamental domain? The main idea is that our compactification can not induce any additional curvature, therefore there can be no stretching or bending of the space. Not all shapes are capable of being a fundamental domain given this restriction, this is analogous to why a soccer ball can not be tiled by hexagons alone unless our ball is no longer $\mathbb{S}^2$. As such we must construct our fundamental domain using only isometric transitions[13] Γ, this prevents any addition of curvature, which would affect our distance relations. Therefore we must find a fundamental domain were we can map all points in a domain to all their images using transitions in Γ. A fundamental domain shape is not usable when there does not exist a mapping to map all points from one image domain I_a to another image domain I_{a+n}, that is isometric, for all a and n, where a and n are such that I_a and I_{a+n} is also contained in the set of all image domains.

We focus on the spherical case, as the latest data shows that the Universe is closer to a closed space than to an open one. For the $\mathbb{S}^3$ space, the group of isometries is $SO(4) = \Gamma$, which are all rotations in a four dimensional space, but unlike in three dimensions there is no point that is held fixed during the rotations. Due to the rotational nature of these transitions, we use unit quaternions[14] to describe theses rotations [Gausmann et al. 2001]. We describe the position of each image by a unit quaternion, this allows treatment of transitions from one image to another by the use of a rotation matrix for the unit vector quaternions. A more detailed view on the construction of the finite subgroups for $\mathbb{S}^3$ can be found in, e.g. [Gausmann et al. 2001].

Table 1.2: Table of the finite subgroups of $\mathbb{S}^3$ Universal Cover from [Gausmann et al. 2001].

Group transitions	Space Symbol	Order	Shape of Fundamental Domain
Cyclic group	Z_n	n	lens
Binary dihedral group	D_m	$4m$, $m \geq 2$	m sided prism
Binary tetrahedral group	T	24	regular octahedron
Binary octahedral group	O	48	regular truncated cube
Binary icosahedral group	I	120	regular dodecahedron

Let $\mathcal{D}$ be the discrete subgroup of isometries that translate all points in a domain to an image domain. The isometries that remain are $\gamma = \Gamma/\mathcal{D}$, out of these remaining transitions the isotropy group is broken and possibly the homogeneity group as well depending on the domain. For a 3-space to be globally isotropic, it is required that the set of all rotations of the 3-space are isometric. Let's look at an example in 2-space where we choose a point near the edge of the fundamental

[13] isometric transitions retain the distance relation between points

[14] These are the four dimensional analog to complex numbers

domain. If we rotate all points around this point, when they cross the boundary some renter with a different distance relation to one another, this is best seen in figure 1.10. Take the two points **a** and **b** they are a distance **d** from each other (this being the shortest distance between them), now rotate the 2-space to the prime 2-space. The distance between $\mathbf{a}'$ and $\mathbf{b}'$, $\mathbf{d}' \neq \mathbf{d}$, therefore rotation is not an isometric transition for all points in this multiconnected space. If we expand to all multiconnected spaces it is obvious that this will always be the case, all multiconnected spaces are globally anisotropic.

Homogeneity requires that translations in the 3-space are isometric. Not all multiconnected spaces are globally homogeneous, For example a Klein bottle though not a flat 2-space it will serve to illustrate a non globally homogeneous multiconnected space. See figure 1.11, where under a translation, the shortest distance between $\mathbf{a}'$ and $\mathbf{b}'$ is not the same as the shortest distance between **a** and **b**, $\mathbf{d}' \neq \mathbf{d}$. Essentially the property that destroyed homogeneity is that the boundaries are anti-parallel in figure 1.11. Multiconnected spaces with a hyperbolic universal cover are all inhomogeneous [Bond et al. 1998]. This leads to the observer dependence which is an issue, as computationally it will lengthen run times of the analysis because we have to simulate for many observer positions. Even if a multiconnected space that is inhomogeneous is found to fit the Universe, there is the nagging question as to why are we located where we are, especially if we are near the center of the Universe. Having a homogeneous space is therefore much simpler conceptually.

It is worth noting that even though the local geometry of the 3-space is not affected by the introduction of the multiconnectivity, presence of a particular curvature does restrict the allowable types of fundamental domains. This is due to the requirement to preserve the constant curvature everywhere.

1.4.3 Why a Compact Space

Why are we interested in a multiconnected Universe? First of all for the compactness of our Universe, multiconnected spaces are the only compact possibility if the curvature is negative or zero. While spherical models are compact by themselves, the observed value of curvature is such that $\mathbb{S}^3$ spaces that fit the data are very large and my benefit from extra topological compactification. Philosophical reasoning for compactness may be that nothing in the Universe is truly infinite so why should the Universe itself be infinite in size. There are also many theories that are formulated with extra compact dimensions, so why would the three space-like dimensions be infinite? It has also been mentioned that the production of a finite (smaller) universe is more probable than that of an infinite (larger) one [Cornish et al. 1998]. Then there exists observational evidence that a compact universe can account for some peculiar observations. The CMB power spectrum as a significant lower mode suppression [Spergel et al. 2003; Smoot

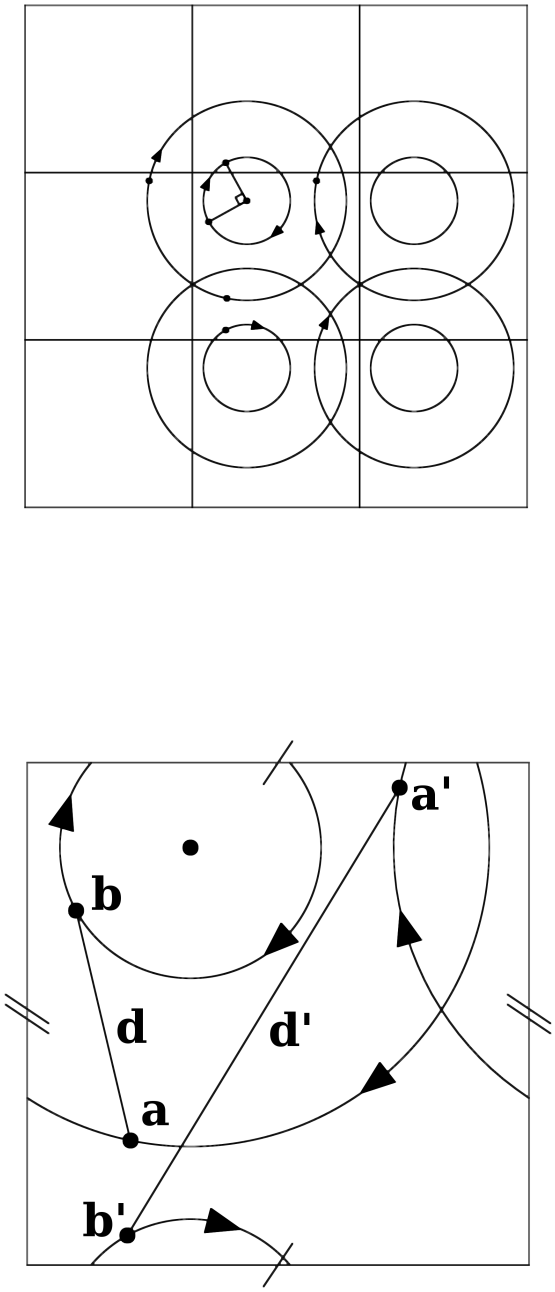

Figure 1.10: The top panel is the universal cover $\mathbb{R}^2$ tiled by squares which corresponds to a torus. The bottom panel is the fundamental domain. The two points **a** and **b** are rotated 90° to $\mathbf{a}'$ and $\mathbf{b}'$. As can be seen rotation not isometric as $\mathbf{d}' \neq \mathbf{d}$. Therefore violating global isotropy.

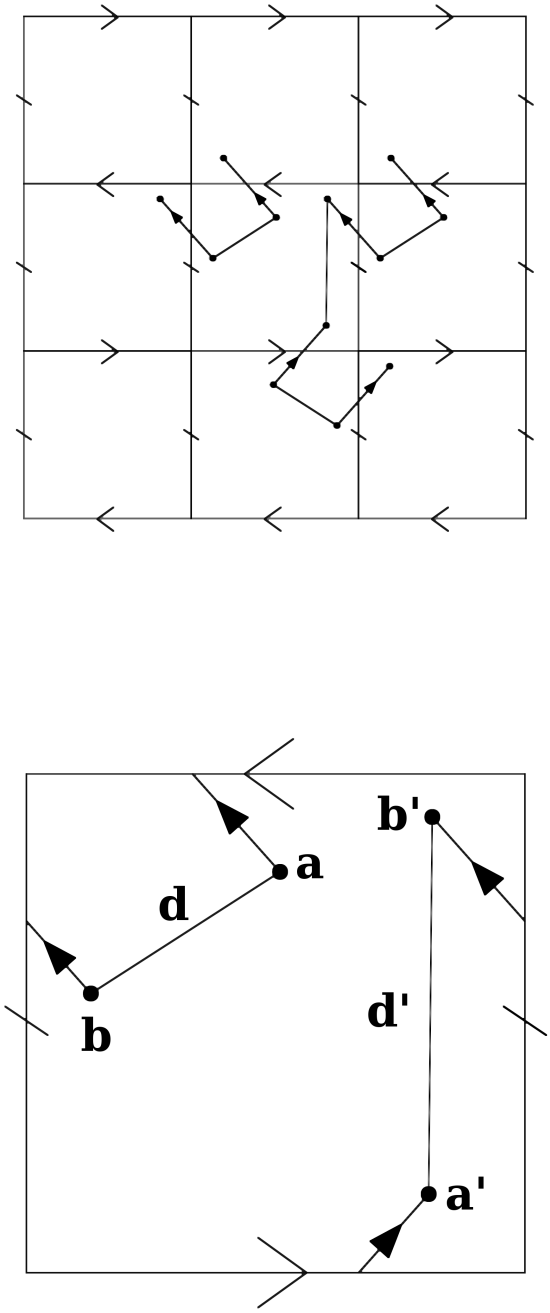

Figure 1.11: The top panel is the universal cover $\mathbb{R}^2$ tiled by squares which correspond to the multiconnected space of a Klein bottle. The bottom panel is the fundamental domain. The two points $\mathbf{a}$ and $\mathbf{b}$ are moved using the same translation to $\mathbf{a}'$ and $\mathbf{b}'$. As we can see in this case the translation is not isometric as $\mathbf{d}' \neq \mathbf{d}$. Therefore violating global homogeneity.

et al. 1992] which can be explained by the presence of a compact universe providing a characteristic length scale causing this lower mode suppression. A strange quadruple-octupole alignment in the the CMB spectrum also exists, which may point to some specific topology as the cause [Aurich et al. 2007], but investigations have not yet revealed any positive results. Though these observations are odd it is worth noting that there is the possibility that our observations could simply be due to random chance, like the role of a dice this could just be the realization that we have for our sky. Since the CMB is a random Gaussian field for which we only have one realization, our one realization can have some particularities, that when averaged over the ensemble of all realizations disappears.

1.4.4 Methods of Detection

There are a number of methods to determine the shape of the fundamental domain. They fall into two basic categories, direct methods and indirect methods. The direct methods have the potential to blindly determine the shape of the fundamental domain from the observed data, a seemingly stronger approach. Whereas indirect methods, need a topological model to compare the observed data with, to see if it is a good fit. This is long and can be an ultimately futile task as the number of possible multiconnected spaces is well into the infinities.

1.4.4.1 Direct Methods

These methods are the seemingly logical choice to use when determining the topology of the Universe. There are two ways to get direct measurements of the fundamental domain, the first is to search for multiple images [Sokolov & Shvartsman 1974], called the crystallographic method [Lehoucq et al. 1996; Uzan et al. 1999], and then there is the circles in the sky method [Weeks 1998; Cornish et al. 1998].

The crystallographic method is very simple in conception, but rather difficult in execution. The essence of the idea is that, if we live in a multiconnected space we have the possibility to observe multiple images, from multiple directions of the same object. This only works assuming that the Universe is smaller than our visual horizon. Take for example a fundamental domain that is a two dimensional square, with sides of length a, and a universal covering space that is R^2. In this domain there is a galaxy (**O**) at distance l from the observer, now let the horizon be of radius a. Figure 1.12 depicts what we see, and that is, that there will be three images (**I**) of the galaxy (**O**). There are some issues with this. The first being, that the farther the distance to an image, the farther back in time the object is being observed, this means that not only will the observer have to deal with the obscuring effects from the red-shift and intermediate objects, but will also need to consider the evolution of the astronomical object that is being

observed. Quasars are some of the brightest objects in the sky, obviously these would make great sources to test for the topology, but unfortunately Quasars are short lived objects on the astronomical scale. Meaning that the difference in the distance to an image and from the source will have to be correspondingly short [Lehoucq et al. 1996]. There are many types of objects to choose from such as galaxies and galaxy clusters, recorded in many different sources catalogs. Consequently it could take a very long time to measure a positive detection, if one exists, unless one test for a specific topology. The second being, that the size difference between the horizon and the fundamental domain does has to be such that there exists an image to view. So we have to consider that there might not be an object suitable for this kind of observation.

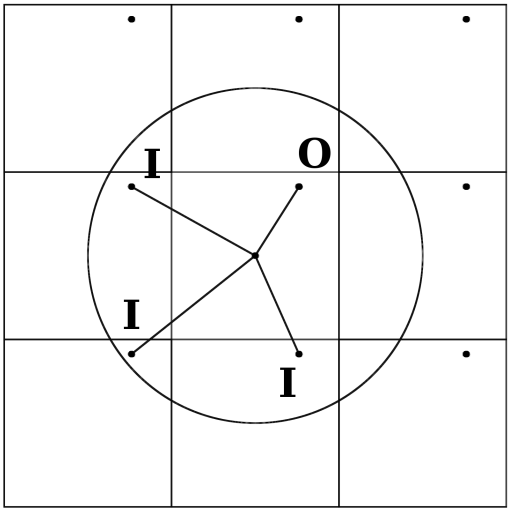

Figure 1.12: This is a universal cover corresponding to $\mathbb{R}^2$, tiled by squares. The original object **O** has three images **I**, where as the rest are not visible since they are beyond the horizon.

The circles in the sky method is more elegant. In this method the idea is to look for correlated pairs of circles of temperature values on different parts of the sky [Cornish et al. 1998]. These circles originate from the overlap of the last scattering horizon with itself, as seen by an observer from multiple directions, see figure 1.13. What is seen are two circles that have the same temperatures along these circles on the sky.

This again requires that the fundamental domain be smaller than the horizon of last scattering, but unlike the crystallographic method, the size difference between

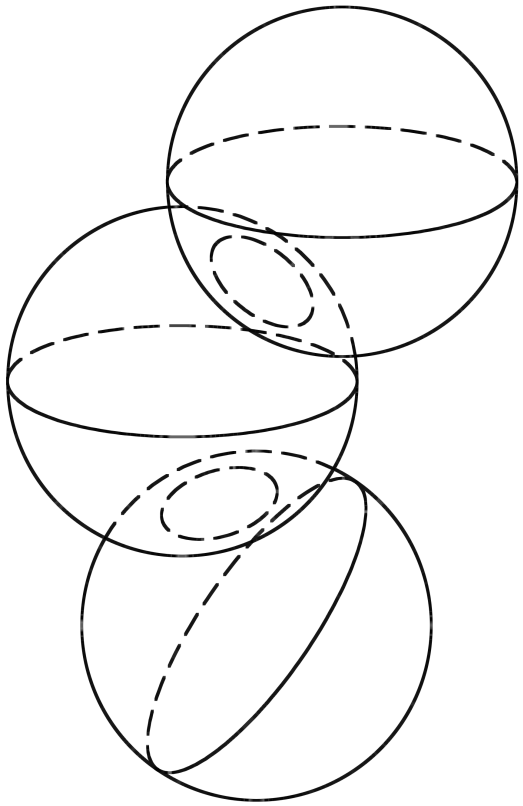

Figure 1.13: The intersection of the horizon with two image horizons from adjacent image domains, where they intersect is a circle that can be seen from two directions. These two circles will be correlated as they are images of the same temperatures on the sky.

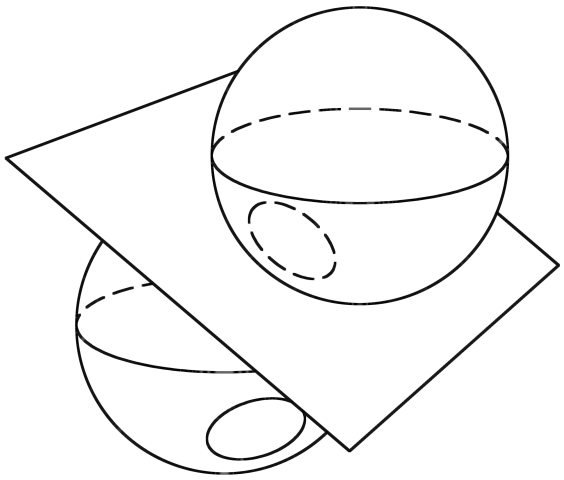

Figure 1.14: Running a plane through one of the circle pairs found on the sky provides an edge to the fundamental domain.

them does not have to be as severe. Even if the domain is only marginally smaller, there will still be some overlap of the last scattering surface, only the size of the circles will change with the size of the domain, becoming smaller, the larger the domain is relative to the horizon of last scattering. If pairs of circles are found, it is rather simple to form a domain [Weeks 1998]. To do so one simply places an infinite plane that intersects the horizon of last scattering and one of the correlated circles, this forms the edge of the domain as in figure 1.14. The more circles that are found the more edges of the domain are determined. A check of the domain is that it should tile the universal covering space, this is a great check for errors such as false circles [Cornish et al. 1998]. Another procedure is that one is not required to find all the pairs of correlated circles, as each pair provides a holonomy of the multiconnected space which can be used to limit the number of possible multiconnected spaces for our Universe. Unfortunately this method is highly susceptible to the effects caused by secondary anisotropies.

To date no direct detection of any kind has been made. This is not an indication that no topological signal exists, but these method are computationally intensive and making blind tests for the topology are almost impossible. As such constraints are usually used, such as a specific topological model.

1.4.4.2 Indirect methods

Indirect methods potentially do not require that the Universe be of a certain size. These methods analyze patterns that emerge given a certain topological constraint. As seen before, the power spectrum is a powerful tool, and it can be used to investigate the possible finite nature of the Universe. The issue is that a multiconnected spaces are not isotropic as seen in figure 1.10, which makes the whole point of using the power spectrum inappropriate. But we can estimate a possible characteristic length scale of the Universe by assuming that it is isotropic and then analyzing the suppression of the lower multipoles, to obtain the length scale. This does not provide a specific shape of the fundamental domain, but it is no less interesting.

Another method, which is the one that we use, is to compare a theoretical correlation for a certain model/shape of the CMB in real space to the observed CMB data map. What we obtain is the probability of observing our CMB data map (a single possible realization), given our theoretical basis. This method is known as the Likelihood method.

Chapter 2

Likelihood Function and Correlation Matrix

2.1 The Correlation Matrix

The observed CMB temperatures $T(\hat{\mathbf{q}})$, in the direction on the sky is specified by the unit vector $\hat{\mathbf{q}}$ from the observer. This temperature reflects the random perturbations in photon-baryon plasma at the epoch of last scattering, and modifications to the temperature induced during photon propagation from the surface of last-scattering to the observer. These temperatures constitute a two-dimensional random field on a 2-sphere, and this field is practically Gaussian due to the quantum origin of perturbations and linearity of their evolution.

Experimentally determined temperature maps are pixelated, thus one deals with a finite set of random variables that can be viewed as a finite-dimensional vector $\mathbf{x} = (T_1, T_2, \cdots T_{np})$, where np is the number of pixels that make up our map. If one focuses on temperature fluctuations, each ΔT_p is a random variable with zero mean, but correlated between different pixels as described by the covariance matrix,

$$\mathbf{C} = C_{pp'} = \langle \Delta T(p) \Delta T(p') \rangle \tag{2.1}$$

which plays the role that the correlation function plays in the continuous case.

We are interested in the probability of having a specific set of temperatures values that constitute our map, like the data map that we see as our observed CMB sky. As stated our random field is Gaussian, as such all of its statistical properties can be described by $\mathbf{C}$, namely the probability distribution of $\mathbf{x}$ is given by,

$$P(\mathbf{x}) = \frac{1}{(2\pi)^{\frac{np}{2}} \det(\mathbf{C})^{\frac{1}{2}}} e^{-\frac{\mathbf{x}^T \mathbf{C}^{-1} \mathbf{x}}{2}} \tag{2.2}$$

The statistical properties that are contained in $\mathbf{C}$ originate from the physical processes that form the CMB anisotropies. To compare the data with a model,

we need first of all to generate a theoretical prediction for correlation matrix **CT**, called our theoretical correlation matrix. To reiterate **CT** is the np by np correlation matrix for the model and is in pixel space which contains np pixels, $CT_{pp'}$ is the value of the correlation between pixel p and pixel p' that the theory predicts.

2.1.1 Correlation Matrix Generation for a Given Multiconnected space

The theoretical correlation matrix must be generated for our multiconnected space.

$$CT_{pp'} = \bar{T}^2 \left\langle \frac{\Delta T}{\bar{T}}(p) \frac{\Delta T}{\bar{T}}(p') \right\rangle \tag{2.3}$$

To determine the correlation between two points on the sky, p and p', we first we must compute their ΔT according to equation 1.7. $\hat{\mathbf{q}}$ and $\hat{\mathbf{q}}'$ are the unit directional vectors for p and p' respectively from the observer. The correlation matrix then becomes equation 2.4 which when expanded becomes equation 2.5.

$$\begin{aligned} CT_{pp'} = \bar{T}^2 \Bigg\langle & \left(\frac{1}{3}\Phi(\chi\hat{\mathbf{q}})|_{\chi=\chi_H} + 2\int_0^{\chi_H} \dot{D}(\chi)\Phi\left(\chi\hat{\mathbf{q}}\right) e^{-\tau_{reion}}\, d\chi \right) \\ & \left(\frac{1}{3}\Phi(\chi\hat{\mathbf{q}}')|_{\chi=\chi_H} + 2\int_0^{\chi_H} \dot{D}(\chi)\Phi(\chi\hat{\mathbf{q}}') e^{-\tau_{reion}}\, d\chi \right) \Bigg\rangle \end{aligned} \tag{2.4}$$

$$\begin{aligned} CT_{pp'} = & \frac{1}{9}\bar{T}^2 \left\langle \Phi(\chi_H\hat{\mathbf{q}})\Phi(\chi_H\hat{\mathbf{q}}') \right\rangle \\ & + \frac{2}{3}\bar{T}^2 \int_0^{\chi_H} \dot{D}(\chi) e^{-\tau_{reion}} \left(\langle \Phi(\chi\hat{\mathbf{q}}')\Phi(\chi_H\hat{\mathbf{q}}) \rangle + \langle \Phi(\chi_H\hat{\mathbf{q}}')\Phi(\chi\hat{\mathbf{q}}) \rangle \right) d\chi \\ & + 4\bar{T}^2 \int_0^{\chi_H}\int_0^{\chi_H} \dot{D}(\chi_1)\dot{D}(\chi_2) e^{-2\tau_{reion}} \langle \Phi(\chi_1\hat{\mathbf{q}}')\Phi(\chi_2\hat{\mathbf{q}}) \rangle \, d\chi_1 \, d\chi_2 \end{aligned} \tag{2.5}$$

Therefore the correlation between two points on the sky is related to the correlation of the potential field in space. To obtain the potentials correlation between the two points in space we use equation 2.6 [Bond et al. 2000a]

$$\xi_\Phi(\mathbf{x}, \mathbf{x}') = \langle \Phi(\mathbf{x})\Phi(\mathbf{x}') \rangle = \sum_i P(k_i) \sum_j^{m_i} \Psi_{ij}(\mathbf{x})\Psi^*_{ij}(\mathbf{x}') \tag{2.6}$$

$P(k_i)$ is the power spectrum for the potential perturbations, and Ψ_{ij} are the eigenfunctions of the Laplace operator in the fundamental domain $(\Delta^2 + k_i^2)\Psi_{ij} = 0$. Calculating these eigenfunctions can be lengthy and difficult for a given fundamental domain. The calculation of the eigenfunctions can be done, as outlined for spherical multiconnected spaces in e.g. [Lehoucq et al. 2002], but there is an alternative, called the method of images [Bond et al. 1998].

2.1.2 Method of Images

Computing the correlation between two points $\mathbf{x}$ and $\mathbf{x}'$ in a multiconnected space can be done by summing the correlation function of the universal covering space for point $\mathbf{x}$ and all the images of $\mathbf{x}'$. This method is called the method of images. To derive this method start with the following two relations.

$$\int_{\mathcal{M}} \xi_{\Phi}^{f}(\mathbf{x},\mathbf{x}')\Psi_i(\mathbf{x}')\, d\mathbf{x}' = P_{\Phi}(k_i)\Psi_i(\mathbf{x}) \tag{2.7}$$

$$\int_{\mathcal{M}^u} \xi_{\Phi}^{u}(\mathbf{x},\mathbf{x}')\Psi_i(\mathbf{x}')\, d\mathbf{x}' = P_{\Phi}(k_i)\Psi_i(\mathbf{x}) \tag{2.8}$$

The ^{f} represents the fundamental domain $\mathcal{M}$, and ^{u} is for the universal covering space $\mathcal{M}^u$. The eigenfunctions of the fundamental domain $\mathcal{M}$ are also the eigenfunctions of the universal cover $\mathcal{M}^u$, therefore we can equate the previous two relations [Bond et al. 1998].

$$\int_{\mathcal{M}^u} \xi_{\Phi}^{u}(\mathbf{x},\mathbf{x}')\Psi_i(\mathbf{x}')\, d\mathbf{x}' = \int_{\mathcal{M}} \xi_{\Phi}^{f}(\mathbf{x},\mathbf{x}')\Psi_i(\mathbf{x}')\, d\mathbf{x}' \tag{2.9}$$

The universal covering space $\mathcal{M}^u$ is tiled by images of the fundamental domain $\mathcal{M}$, the integral over all of $\mathcal{M}^u$ is then simply the sum of the integrals over the individual images of $\mathcal{M}$ that tile the universal cover. Therefore we manipulate the integral in equation 2.8 the following way.

$$\int_{\mathcal{M}^u} \xi_{\Phi}^{u}(\mathbf{x},\mathbf{x}')\Psi_i(\mathbf{x}')\, d\mathbf{x}' = \sum_{\pi\in\Pi} \int_{\mathcal{M}} \xi_{\Phi}^{u}(\mathbf{x},\pi\mathbf{x}')\Psi_i(\mathbf{x}')\, d\mathbf{x}' \tag{2.10}$$

$$= \int_{\mathcal{M}} [{\sum_{\pi\in\Pi}}' \xi_{\Phi}^{u}(\mathbf{x},\pi\mathbf{x}')]\Psi_i(\mathbf{x}')\, d\mathbf{x}' \tag{2.11}$$

$\pi \in \Pi$ represents an image of the fundamental domain $\mathcal{M}$ which is $\mathcal{M}^\pi$ in the set of all possible image domains denoted by Π, note that since it is an image $\mathcal{M}^\pi = \mathcal{M}$. Equating with equation 2.7 obtains the following relation.

$$\int_{\mathcal{M}} \xi_{\Phi}^{f}(\mathbf{x},\mathbf{x}')\Psi_i(\mathbf{x}')\, d\mathbf{x}' = \int_{\mathcal{M}} [{\sum_{\pi\in\Pi}}' \xi_{\Phi}^{u}(\mathbf{x},\pi\mathbf{x}')]\Psi_i(\mathbf{x}')\, d\mathbf{x}' \tag{2.12}$$

The $'$ on the $\sum'_{\pi\in\Pi}$ indicates that the sum may need to be regularized, though this is only for a non-closed universal covers, where there is an infinite set of image domain such, as the flat and the hyperbolic universal covering spaces [Bond et al. 1998]. We do not have to deal with this issue as our universal cover is $\mathbb{S}^3$ and thus finite. Equation 2.12 holds for all the eigenfunctions of the multiconnected space Ψ_i, thus we obtain our main equation for the method of images, equation 2.13.

$$\Rightarrow \boxed{\xi_{\Phi}^{f}(\mathbf{x},\mathbf{x}') = \sum_{\pi\in\Pi} \xi_{\Phi}^{u}(\mathbf{x},\pi\mathbf{x}')} \tag{2.13}$$

This equation provides the relation as stated in the beginning of this section, and saves us from having to compute the eigenfunctions for the multiconnected space.

To use this method in determination of the correlation between two points, we start with the two points in space which are $\mathbf{x}$ and $\mathbf{x}'$. First we place the images of $\mathbf{x}'$, $\pi\mathbf{x}'$, in all the image domains. Now we use equation 2.13 which means that we need the correlation between $\mathbf{x}$ and $\pi\mathbf{x}'$ for the universal cover's correlation function ξ^u. The correlation function $\xi^u(\mathbf{x}, \pi\mathbf{x}')$ is simply calculated as stated previously using equation 2.6. We then sum over all the images to obtain the correlation value for the two points $\mathbf{x}, \mathbf{x}'$.

It is this method that we use in the computation of our theoretical correlation matrices. Using equation 2.5, we use the method of images to compute the potential spacial correlation functions and obtain our **CT**. Figure 2.1 and 2.2 are visualization of the correlation about pixel number 500 for an isotropic and anisotropic Universe respectively

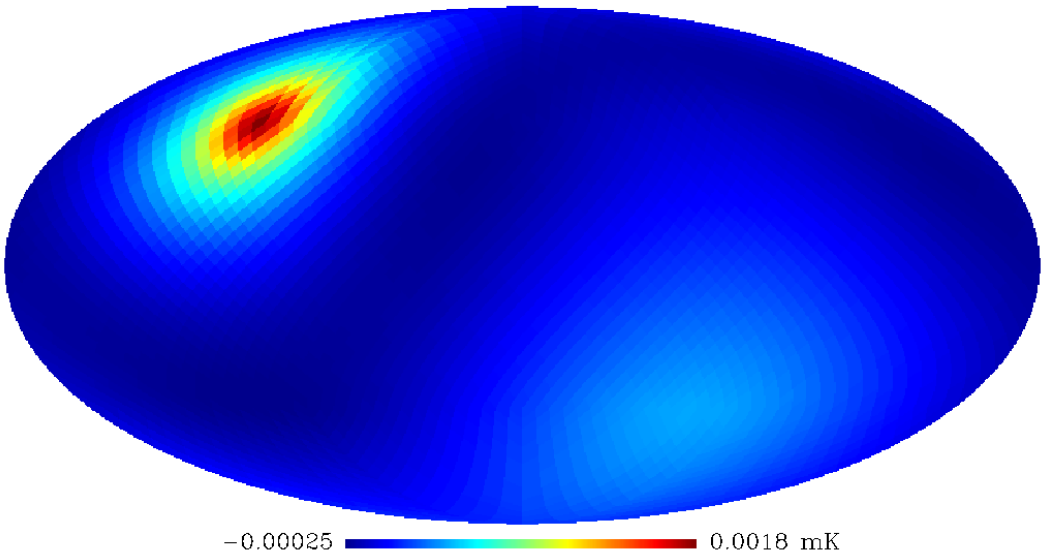

Figure 2.1: Correlation matrix visualization for the 500th pixel, for an isotropic model. This is for a space that has a large domain size when compared to the distance of the last scattering horizon. Notice the lack of correlation patterns.

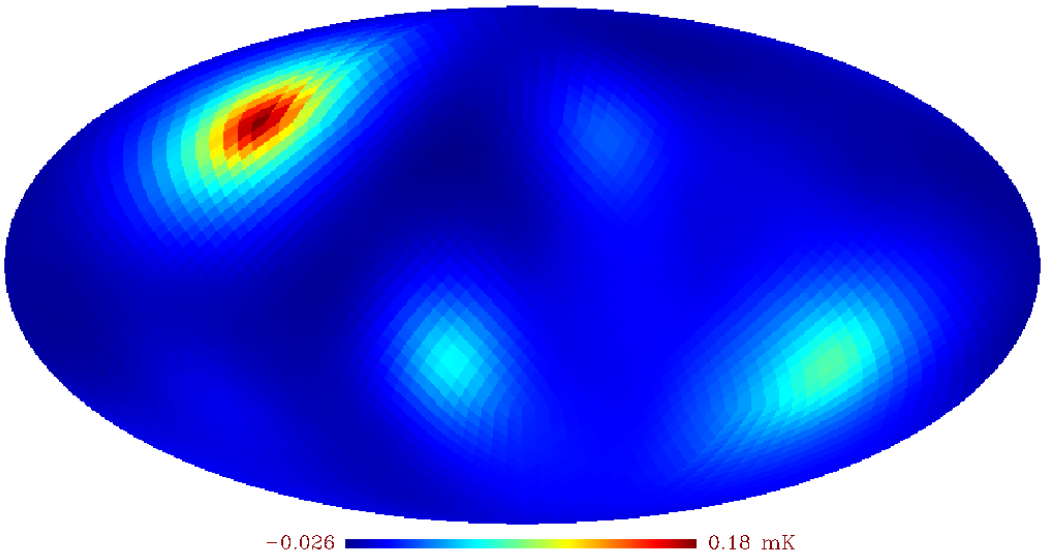

Figure 2.2: Correlation matrix visualization for the 500th pixel for an anisotropic space. This is for a space that has a small domain size when compared to the distance of the last scattering horizon. Notice the increased correlation with other pixels.

2.1.3 Visualization of the effects of the Topology

A visualization of multiple images of a point as seen by an observer in a multiconnected spaces can be simulated. Three visualizations were computed for the three multiconnected spaces that we will examine. The three figures in figure 2.3 show images of an object located at the observer as seen when the horizon is such that it encompasses the universal covering space. As such we should be able to count the number of domains that tile the universal covering space minus two, since the observer does not see oneself in the domain that the observer occupies, and that the last domain's image simply fills the whole sky as it is located in the point on our 3-sphere universal covering space that is antipodal to the observer. From the three figures we can actually make out the shape that is the multiconnected space, the most obvious being the dodecahedral space-I.

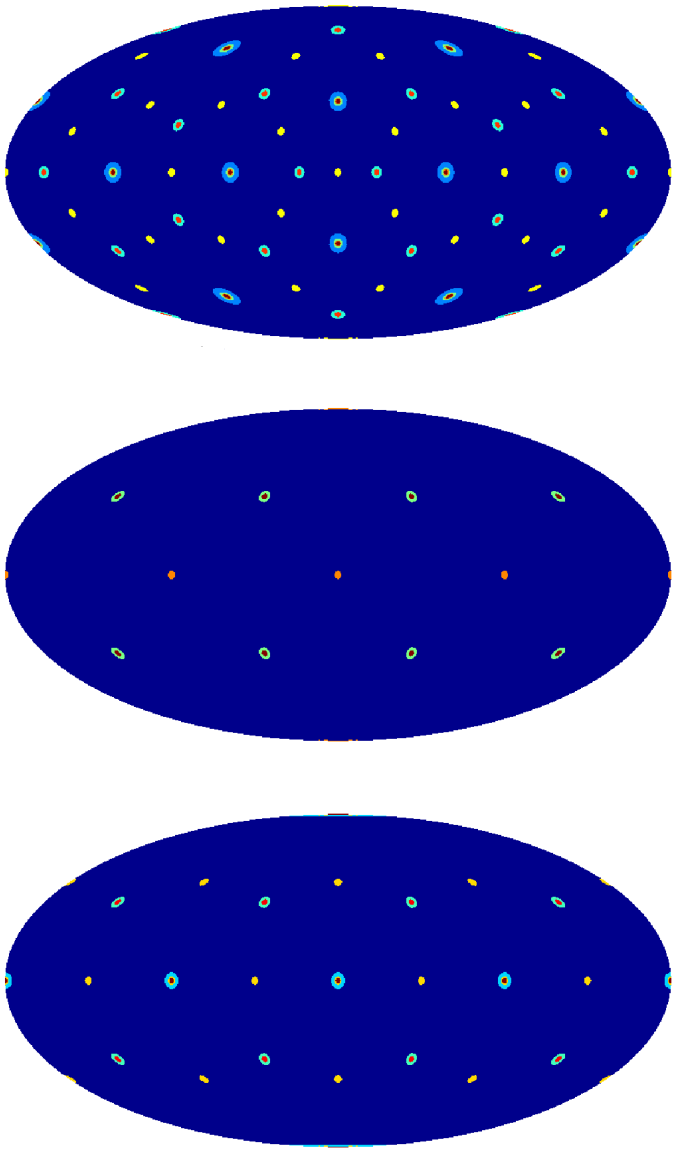

Figure 2.3: Visualization on the sky of images for the observer. The top panel is space-I, the middle panel space-T, and the last panel space-O see section 1.4.2. The size of the dot is inversely proportional to the distance from the observer. This distance is also color coded so that we may observe the images on overlapping lines of sight.

2.2 Likelihood function

The Likelihood function computes a value for which the effectiveness of the topological model can be determined. Essentially it is the probability of observing the observed CMB data map given a certain topological model. This is a non-normalized probability, as we do not have access to all possible skies to which it can be normalize against as we only have one sky to observe. But this value is useful for the comparison between models.

2.2.1 Meaning of the Likelihood

The likelihood is the probability that our data $\mathbf{x}$ will be realized given the correlation matrix $\mathbf{C}$. Simply $\mathcal{L}_{\mathbf{x}}(\mathbf{C}) = P(\mathbf{x}|\mathbf{C})$[1] where $\mathbf{x}$ is our observed CMB data map. We can easily calculate the likelihood value using equation 2.2, the n-point probability function of a random Gaussian field with correlation matrix $\mathbf{C}$.

$$P(\mathbf{x}|\mathbf{C}) = \frac{1}{(2\pi)^{\frac{np}{2}} \det(\mathbf{C})^{\frac{1}{2}}} \, e^{(-\frac{1}{2}\mathbf{x}^T\mathbf{C}^{-1}\mathbf{x})} \tag{2.14}$$

$\mathbf{C}$ is our correlation matrix in pixel space, which contains the statistics of our model. However, to objectively judge the model, it would be more appropriate to find the *posterior probability* $P(\mathbf{C}|\mathbf{x})$. Bayes theorem states that $P(a|b) = \frac{P(b|a)P(a)}{P(b)}$ therefore we can calculate $P(\mathbf{C}|\mathbf{x})$ from $P(\mathbf{x}|\mathbf{C})$ the following way.

$$P(\mathbf{C}|\mathbf{x}) = \frac{P(\mathbf{x}|\mathbf{C})P(\mathbf{C})}{P(\mathbf{x})} \tag{2.15}$$

$P(\mathbf{x})$ is called the *evidence* and is the probability of obtaining this data realization from all possible others. We only have one sky as such we do not know $P(\mathbf{x})$ but this simply a normalization term. $P(\mathbf{C})$ is called the *prior* which represents our prior knowledge about the probability of the model being chosen out of all possible models. It is here that we may add additional constraints obtained from other experiments or observations on the likelihood that this model is a good fit. For us, in this experiment we have an equally weighted prior. By not knowing the exact values for $P(\mathbf{C})$ and $P(\mathbf{x})$, we can only compare ratios.

$$\frac{P(\mathbf{C}_1|\mathbf{x})}{P(\mathbf{C}_2|\mathbf{x})} = \frac{P(\mathbf{x}|\mathbf{C}_1)}{P(\mathbf{x}|\mathbf{C}_2)} = \frac{\mathcal{L}_{\mathbf{x}}(\mathbf{C}_1)}{\mathcal{L}_{\mathbf{x}}(\mathbf{C}_2)} \tag{2.16}$$

This is why we only use the likelihood value. Our data $\mathbf{x}$ contains both the signal, for which we have the theoretical correlation matrix $\mathbf{CT}$ and the noise to which we have the correlation matrix $\mathbf{CN}$. Due to the fact that the noise is

[1]The notation $P(a|b)$ represents the probability of obtaining/observing the value(s) a while having the value(s) b fixed

generated at the detector, (electronics noise, stray high energy particles, ...), and that the cosmological anisotropies are generated far away from the detector, they are assumed within good approximation to be uncorrelated. Being uncorrelated the correlation matrix $\mathbf{C}$ is simply the sum of the two, $\mathbf{CT} + \mathbf{CN}$. This means that our likelihood equation can be written as equation 2.17.

$$\mathcal{L}_{\mathbf{x}}(\mathbf{CT}) = \frac{1}{(2\pi)^{\frac{np}{2}} \det(\mathbf{CT} + \mathbf{CN})^{\frac{1}{2}}} \, e^{(-\frac{1}{2}\mathbf{x}^{\mathrm{T}}(\mathbf{CT}+\mathbf{CN})^{-1}\mathbf{x})} \tag{2.17}$$

We showed how to calculate $\mathbf{CT}$ in section 2.1.1 and $\mathbf{CN}$ is obtained from our experiment as we will see later in section 3.2.

For computations the natural logarithm of the likelihood, called the log-likelihood is must nicer to deal with. The final equation that we use in our investigation is equation 2.18.

$$\boxed{\ln(\mathcal{L}) = -\frac{1}{2}\left[np\ln(2\pi) + \ln(\det(\mathbf{CT} + \mathbf{CN})) + \mathbf{x}^{\mathrm{T}}(\mathbf{CT} + \mathbf{CN})^{-1}\mathbf{x}\right]} \tag{2.18}$$

For simplicity from now on we will use the notation $\mathcal{L}$ which represents $\mathcal{L}_{\mathbf{x}}(\mathbf{CT})$.

2.2.2 Modes

We are looking for a topological signal as such we are only interested in the lower frequency modes, i.e. the large structures in the CMB anisotropies. This is because the effect of a characteristic length imposed on the Universe by a compact multiconnected space will have the greatest effect on these lower frequency modes. Therefore we smooth out all the higher frequencies, as such our $\mathbf{CT}$ tends to become degenerate, with a number of the eigenmodes being quite small. When noise is large, this is not a problem since we invert $\mathbf{CT} + \mathbf{CN}$, and the noise is expected to be uncorrelated, and therefore diagonal. WMAP and *Planck* for example have very large signal to noise ratio when re-binned to $N_{\mathrm{side}} = 16$, as such the addition of the noise can be ineffective in masking these very small amplitude modes. WMAP for example has around 1% error compared to signal at $N_{\mathrm{side}} = 16$ (see section 3.2 for details). As such the noise does not contribute significantly to the signal, which can make dealing with the likelihood function quite tricky.

The issue is that the likelihood value is greatly affected by these small modes, partially due to the inverse determinant term in equation 2.18. We can induce invertibility by simply dropping these troublesome small or zero modes by using something like a condition number for the matrix. Because the likelihood value by itself is more or less meaningless this appears to be okay, but upon comparison to another likelihood value for another model we then have a problem.

Unfortunately a dynamic choice from model to model that changes the number of modes to be used by the theory is not very informative, since each model can

have a different mode structure, by dropping different modes for computations, it is unclear if the likelihood difference between the models is due to the loss of modes or if it is due to a topological signal. Even the addition of an artificial noise parameter to bump up these lower modes can greatly affect the likelihood value.

A solution is to decompose the correlation matrix and project it onto a set of basis modes that is consistent for every model. By standardizing every model use the same set of eigenmodes we can manipulate the rank of the correlation matrix, while maintaining consistency between the models, the specifics of this is in section 3.3.

To understand the effect that the modes have on the likelihood value let us start with the $\ln(\mathcal{L})$ function that is equation 2.18. $\mathbf{CT}$ is symmetric therefore we can decompose it as

$$\mathbf{CT} = \mathbf{\Psi \Lambda \Psi}^{-1} \tag{2.19}$$

$\mathbf{\Lambda}$ is a diagonal $np \times np$ matrix, where $\Lambda_{ii} = \lambda_i$ and $\Lambda_{ij} = 0, i \neq j$. $\mathbf{\Psi}$ is the $np \times np$ matrix of the eigenvectors where the i'th column is the i'th eigenvector φ_i of $\mathbf{CT}$. By construction these eigenvectors are orthonormal $\Rightarrow \varphi_i \varphi_j^T = 0, i \neq j$. Let our map consist of a single eigenvector of $\mathbf{CT}$, therefore $\mathbf{x} = a\varphi_1$, where a is the amplitude of the map. Now we will examine two cases where we will limit the number of non-zero eigenmodes. We will also ignore the noise component for simplicity. Before this can be done we must analytically calculate the best amplitude for our model. This can be done analytically as we are ignoring the noise contribution to the likelihood function. This has to be computed because though we know what the amplitude should be when we compute $\mathbf{CT}$, the best amplitude may vary sightly from model to model.

$$\det(A\mathbf{CT}) = A^n \det(\mathbf{CT}) \tag{2.20}$$

$$\Rightarrow \ln(\mathcal{L}) = -\frac{1}{2}\left[n\ln(2\pi) + n\ln(A) + \ln(\det(\mathbf{CT})) + \frac{\mathbf{x}^T\mathbf{CT}^{-1}\mathbf{x}}{A} \right] \tag{2.21}$$

We want A at a maximum, $\Rightarrow 0 = \frac{d}{dA}\ln(\mathcal{L}) = \frac{1}{\mathcal{L}}\frac{d}{dA}\mathcal{L}$ and solve for A. $\frac{1}{\mathcal{L}} \neq 0$.

$$\Rightarrow 0 = \frac{d}{dA}\mathcal{L} = \frac{n}{A} - \frac{\mathbf{x}^T\mathbf{CT}^{-1}\mathbf{x}}{A^2}$$

$$\Rightarrow nA = \mathbf{x}^T\mathbf{CT}^{-1}\mathbf{x}$$

$$\Rightarrow \boxed{A = \frac{\mathbf{x}^T\mathbf{CT}^{-1}\mathbf{x}}{n}}$$

Substituting into equation 2.21 gives us,

$$\ln(\mathcal{L}) = -\frac{n}{2}\left[\ln(\frac{2\pi}{n}) + 1 + \ln(\mathbf{x}^T\mathbf{CT}^{-1}\mathbf{x}) + \frac{\ln(\det(\mathbf{CT}))}{n} \right] \tag{2.22}$$

From equation 2.22 there are only two components that depend on the eigenmodes: $\mathbf{x}^T\mathbf{C}\mathbf{T}^{-1}\mathbf{x}$ and $\det(\mathbf{C}\mathbf{T})$. Now we will examine two cases for the effect that the number of non-zero eigenmodes has on the difference in likelihood values.

Case 1:
Let $\mathbf{CT}$ only have only one eigenmode $\Rightarrow \Lambda_{ij} = \lambda_1, i = j = 1$ and $\Lambda_{ij} = 0$ everywhere else. Essentially what we are doing is ignoring the zero eigenmodes for this matrix, as such that they do not appear in the determinate and for inversion the 0 eigenmodes are set to ∞. This is in pixel space and not what we do in reality as we project onto a set of basis eigenvectors thus reducing the rank of the matrix which is explained in more detail in section 3.3.

$$\mathbf{x}^T\mathbf{C}\mathbf{T}^{-1}\mathbf{x} = a^2\mathbf{\Psi}_1^T\mathbf{\Psi}\mathbf{\Lambda}^{-1}\mathbf{\Psi}^T\mathbf{\Psi}_1$$

$$\mathbf{\Psi}_1^T\mathbf{\Psi} = \begin{bmatrix}1 & 0 & \cdots & 0\end{bmatrix}$$

$$\mathbf{x}\mathbf{C}\mathbf{T}^{-1}\mathbf{x}^T = a^2\begin{bmatrix}1 & 0 & \cdots & 0\end{bmatrix}\begin{bmatrix}\frac{1}{\lambda_1} & 0 & \cdots & 0\\ 0 & 0 & \cdots & 0\\ \vdots & \vdots & \ddots & \vdots\\ 0 & 0 & \cdots & 0\end{bmatrix}\begin{bmatrix}1\\0\\\vdots\\0\end{bmatrix}$$

$$\mathbf{x}^T\mathbf{C}\mathbf{T}^{-1}\mathbf{x} = \frac{a^2}{\lambda_1} \tag{2.23}$$

$$\ln(\det(\mathbf{C}\mathbf{T})) = \sum_{i=1}^{n+1}\ln(\lambda_i) = \ln(\lambda_1) \tag{2.24}$$

Substituting in 2.23 and 2.24 into equation 2.22 we obtain.

$$\ln(\mathcal{L}) = -\frac{n}{2}\left[\ln(\frac{2\pi}{n}) + 1 + (\frac{1}{n} - 1)\ln(\lambda_1)\right] \tag{2.25}$$

Case 2:
Let $\mathbf{CT}$ have two non-zero eigenmodes.

$$\Rightarrow \mathbf{\Lambda} = \begin{bmatrix}\frac{1}{\lambda_1} & 0 & \cdots & 0\\ 0 & \frac{1}{\lambda_2} & \cdots & 0\\ 0 & 0 & \cdots & 0\\ \vdots & \vdots & \ddots & \vdots\\ 0 & 0 & \cdots & 0\end{bmatrix}$$

Just as we did for Case 1 we we obtain:

$$\mathbf{x}^T\mathbf{C}\mathbf{T}^{-1}\mathbf{x} = \frac{a^2}{\lambda_1} \tag{2.26}$$

$$\ln(\det(\mathbf{C}\mathbf{T})) = \ln(\lambda_1) + \ln(\lambda_2) \tag{2.27}$$

Therefore the only difference from Case 1 is equation 2.27.

$$\ln(\mathcal{L}) = -\frac{n}{2}\left[\ln(\frac{2\pi}{n}) + 1 + (\frac{1}{n} - 1)\ln(\lambda_1) + \frac{1}{n}\ln(\lambda_2)\right] \tag{2.28}$$

The difference between these two cases is $\Delta \ln(\mathcal{L}) = \ln(\mathcal{L}_{case1}) - \ln(\mathcal{L}_{case2}) = -\frac{1}{2}\ln(\lambda_2)$. Therefore as we decrease the number of non-zero modes the value of $\ln(\mathcal{L})$ increases and becomes more favorable when compared to a model with more eigenmodes, this is assuming that λ_2 is greater than 1. In reality λ_2 is very small as we are manipulating the conditionality of the matrix and dropping these small modes, therefore it will dominate $\ln(\mathcal{L})$ thus the difference will be quite significant between the two models. As such one must make a consistent choice when comparing different models to eliminate any increases to the likelihood value due to one model having extra eigenmodes, and is why we use the procedure in section 3.3.

Chapter 3

The Code

The computation of the likelihood is accomplished by a program called Topmarg, originally created by Dr. C. Contaldi then developed into its current state, as of the date of this thesis, by Dr. Pogosyan and Mr. Knutson. Topmarg is a likelihood code that computes the maximum log-likelihood value for a given **CT**. We provide the likelihood code with four pieces of crucial information, the pixelated to $N_{\rm side} = 16$ data map, the $N_{\rm side} = 16$ theoretical correlation matrix for our model, the inverse noise map that is obtained from the data, and the analysis mask that has been chosen.

First the map is smoothed with a Gaussian beam, then it is masked by our analysis mask. The noise and theoretical correlation matrices are also smoothed with a Gaussian beam and **CT** is additionally smoothed with the pixel window to simulate effect of pixelization. It is also possible to introduce an experimental beam for the apparatus to be used when smoothing, but a beam file must be provided. The correlation matrices are then masked by the same analysis mask as the data.

Next, the data vector **x** and the correlation matrices **CT** and **CN** are decomposed into the chosen set of basis eigenvectors, and then reduced to only contain the decided number of modes. All is then passed to the core of the program, which calculates the maximum likelihood value. There are two sets of parameters that can be varied for the theory in the determination of the maximum likelihood value. These are the amplitude and orientation of our anisotropic space relative to the data map. We do know what the expected amplitude is to be from the data, but there may be differences in the best amplitude between models. The use of a numerical multidimensional minimization routine is used for the determination of the best orientation and for each orientation tested the best amplitude must also be found, this accomplished by the use of another numerical minimization routine.

When the largest log-likelihood value is found, this the maximum log-likelihood

value for this model at the best orientation and with the best amplitude.

3.1 Smoothing and Masking Of $CT_{pp'}$ and x

The patterns that are of interest to us are those at large scales, therefore we smooth out the higher frequency modes of the map, and correlation matrices. Smoothing reduces the features in the map to those of around the same size as seen by the COBE satellite (figure 1.5).

The Data map used is a reduced resolution map with $N_{\text{side}} = 16$ of ΔT values from the much higher highest resolution map of ΔT with an $N_{\text{side}} = 512$ like that in figure 1.6[1], this is accomplished by re-binning the $N_{\text{side}} = 512$ subpixles into the larger $N_{\text{side}} = 16$ pixels. Before the re-binning of the map we mask the point sources and the galactic plane by setting their temperatures to 0. The mask used is the WMAP mask *wmap_temperature_kq75_analysis_mask_r9_9yr_v5.fits* (figure 3.1) from the 9-yr WMAP data release[2]. Since the map is re-binned, there will be some pixels that will only have a handful of sub-pixels that contribute to the temperature value of the pixel. The re-binned point source mask is that in figure 3.2, where the value in each pixel represents the fraction of unmasked sub-pixels. We have chosen that for a pixel to have a valid temperature value it must have no more than 50% of its sub-pixels masked. This is essentially like masking the re-binned data map with the mask in figure 3.3. It is this final data map in figure 3.4, which is then smoothed.

The reason why we do not smooth a full sky map is due to the hot sources that exist in the galactic plane. These hot sources contaminate the whole map when smoothed, this effect is far more detrimental than if these hot spots are masked to $\Delta T = 0$ and then these 0 temperature values spread out by the smoothing.

All smoothing is done in lm space as to reduce any artificial effects due to the pixelated nature of the map. To smooth the maps we first collect the beams. The full width half max value for the Gaussian beam that we use in our investigation is FWHM= 492.0 *arcmin*, which is very close to the COBE satellite's experimental beam. The `HEALPix` routine, *generate_beam* [Górski et al. 2005] generates the l weights that are the Gaussian beam (G_l). Now that we have the Gaussian beam weights, we can smooth the data map. First the data is decomposed into spherical harmonics to obtain its a_{lm} values. Once this is completed, the map is now in a form such that it can be smoothed using another `HEALPix` routine *alter_alm* [Górski et al. 2005], with the generated G_l. The G_l weights that are generated for FWHM=492.0 *arcmin* are in figure 3.6. Figure 3.5 is our re-binned CMB data map after smoothing.

[1]Number of pixels in a `HEALPix` map is $npix = 12 \times N_{\text{side}}^2$

[2]Data release for 9-yr WMAP is obtained from the LAMBDA web site `http://lambda.gsfc.nasa.gov/`

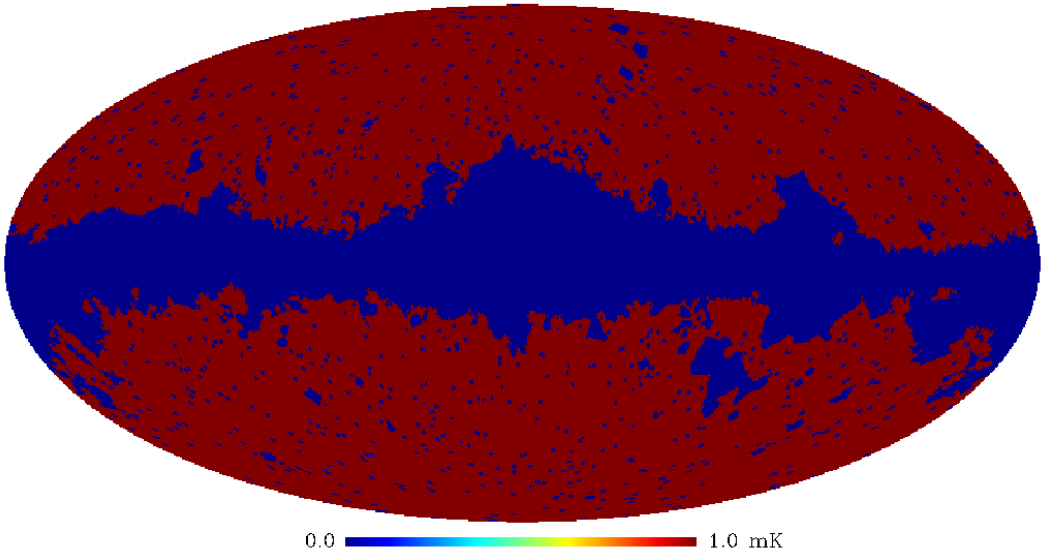

Figure 3.1: The $N_{\text{side}} = 512$ point source mask used when re-binning from $N_{\text{side}} = 512$ to a lower resolution data map.

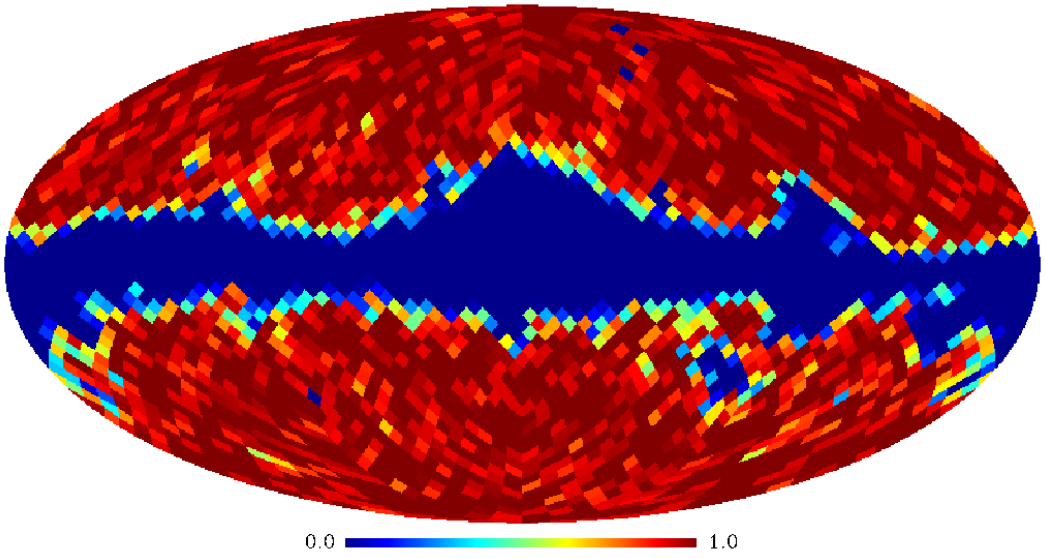

Figure 3.2: The point source mask re-binned to the $N_{\text{side}} = 16$ point source mask, the scale from 0-1 represents the fraction of sub-pixels that remain per pixel, after being masked by the $N_{\text{side}} = 512$ point source mask.

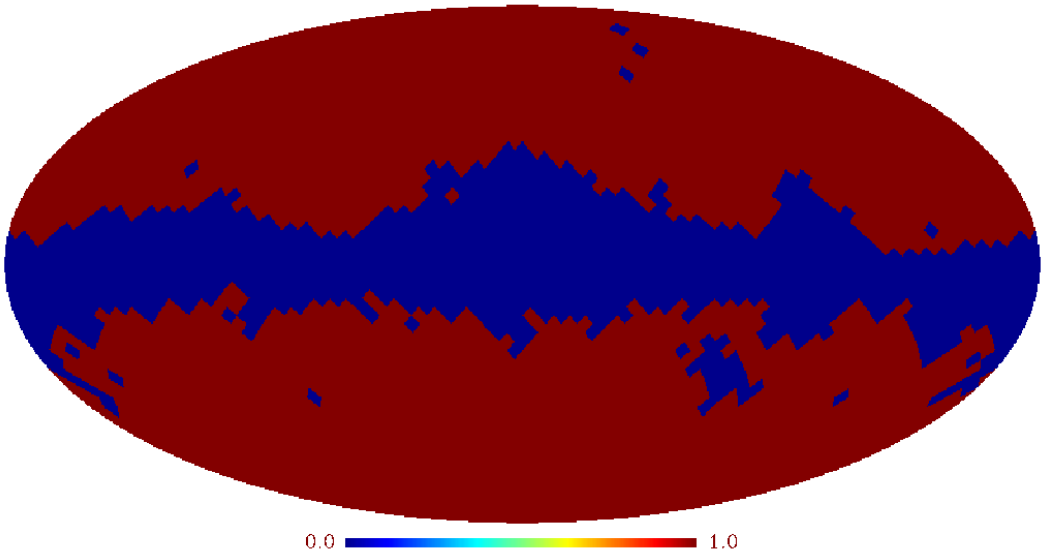

Figure 3.3: The $N_{\text{side}} = 16$ effective mask for the $N_{\text{side}} = 16$ pixels that are fully masked by the 50% masked sub-pixel criteria. $p_i \leq 0.5 \Rightarrow p_i = 0$, $p_i > 0.5 \Rightarrow p_i = 1$

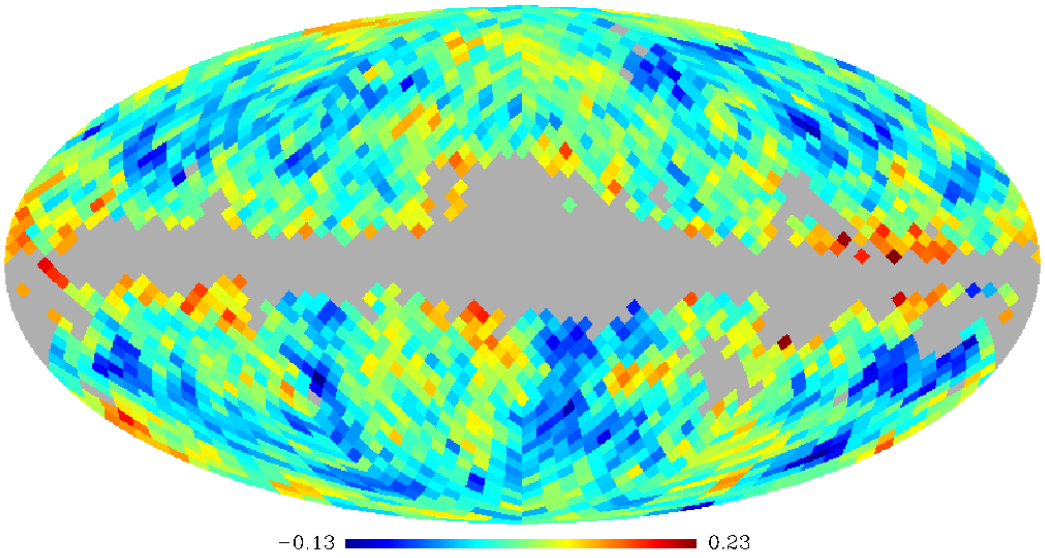

Figure 3.4: The re-binned to $N_{\text{side}} = 16$ data map that is provided to the Likelihood Code.

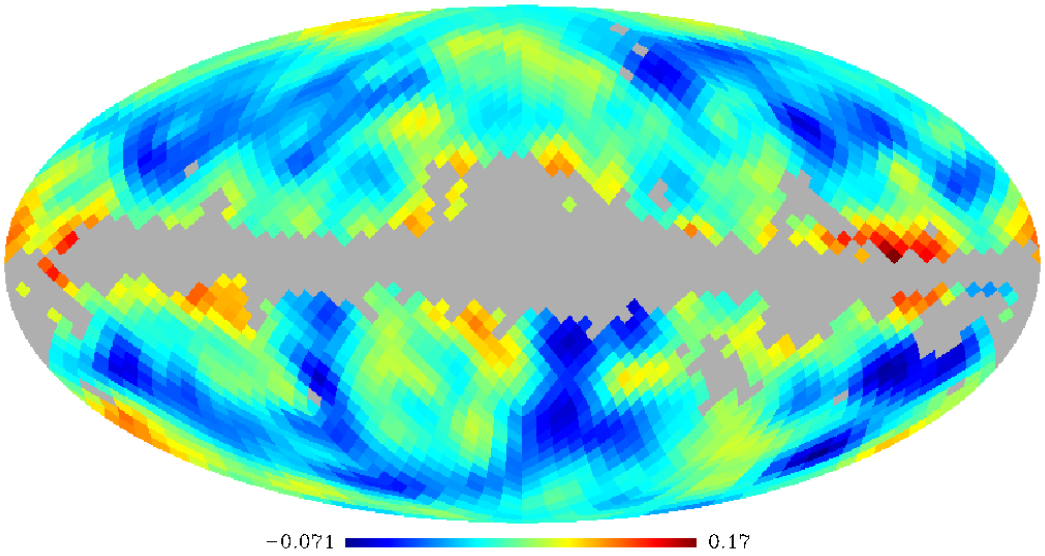

Figure 3.5: The $N_{\text{side}} = 16$ map after it is smoothed by the Gaussian beam with a FWHM= 492.0 *arcmin*

Now that we have the smoothed data map we need to smooth the correlation matrix. We may add an experimental beam *B_exp* if necessary, this is given in pixel space and is derived from the specifications of the experimental apparatus. The experimental beam is necessary as the theoretical correlation matrix must be coherent with the data map, which due to its origin will contain this experimental beam effect. We do not use a WMAP experimental beam since it is insignificant when compared to the large Gaussian beam. Again using the same `HEALPix` routine *generate_beam* another set of l weights are generated but for the experimental beam Ex_l. Only one last component to the beam must be generated before we can smooth the theoretical correlation matrix and that is the pixel window effect. Due to the manner that the theoretical correlation matrix is computed each pixel is simply the value as if it only contained the central point of that pixel. The data pixels are an average of the temperature values contained within that pixel. As such we need to smooth out this singular point such that the correlation matrix ends up with the same effect as the data. Its beam weights are calculated using the `HEALPix` routine *pixel_window* [Górski et al. 2005], which provides another set of l weights, $pixw_l$. Figure 3.7 is the $pixw_l$ weights that are generated. To combine these beams we multiply the three weights.

$$W_l = (G_l)(Ex_l)(pixw_l) \tag{3.1}$$

Now that we have our combined beam weights W_l, the correlation matrix is then smoothed. Again the smoothing is done in lm space, so **CT** is converted from pixel space to lm space and then smoothed, in the following manner.

$$CT^{smoothed}_{lml'm'} = CT_{lml'm'} W_l W_{l'} \tag{3.2}$$

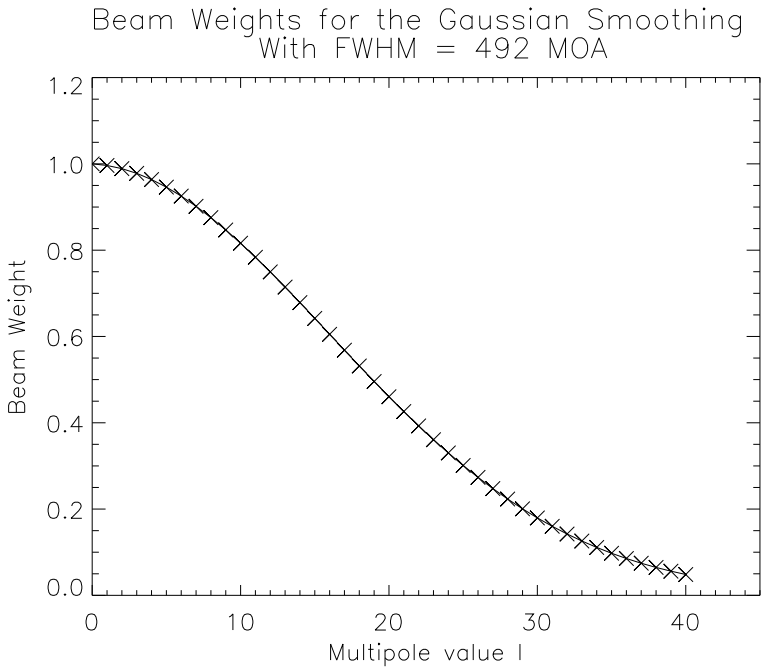

Figure 3.6: The l weights for the Gaussian beam as generated by *generate_beam* with a FWHM= 492.0 *arcmin*.

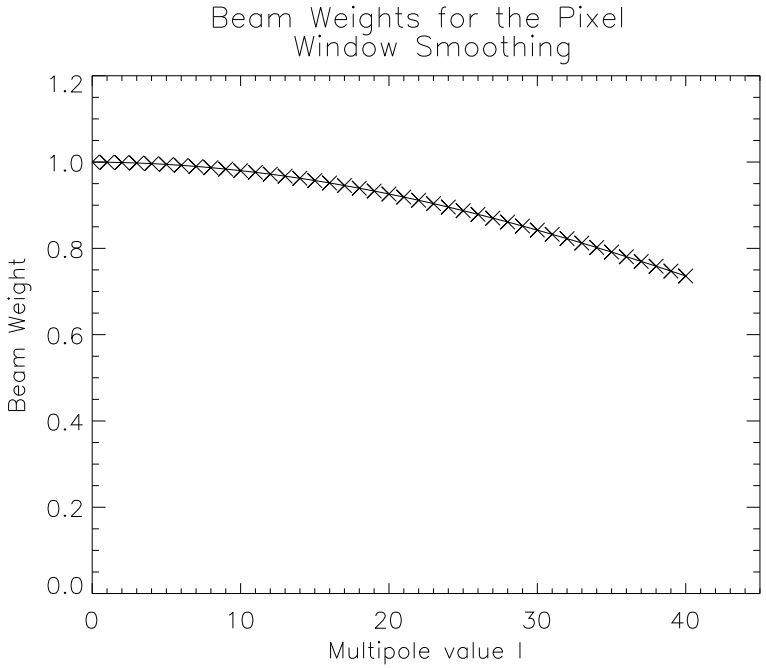

Figure 3.7: The l weights for the pixel window beam as generated by *pixel_window*.

Note that the weights are m independent, therefore all m for a specific l or l' are weighted equally when smoothed. Figure 3.8 and figure 3.9 is the correlation matrix for $\Omega_k = -1.26 \times 10^{-2}$ before and after smoothing respectively.

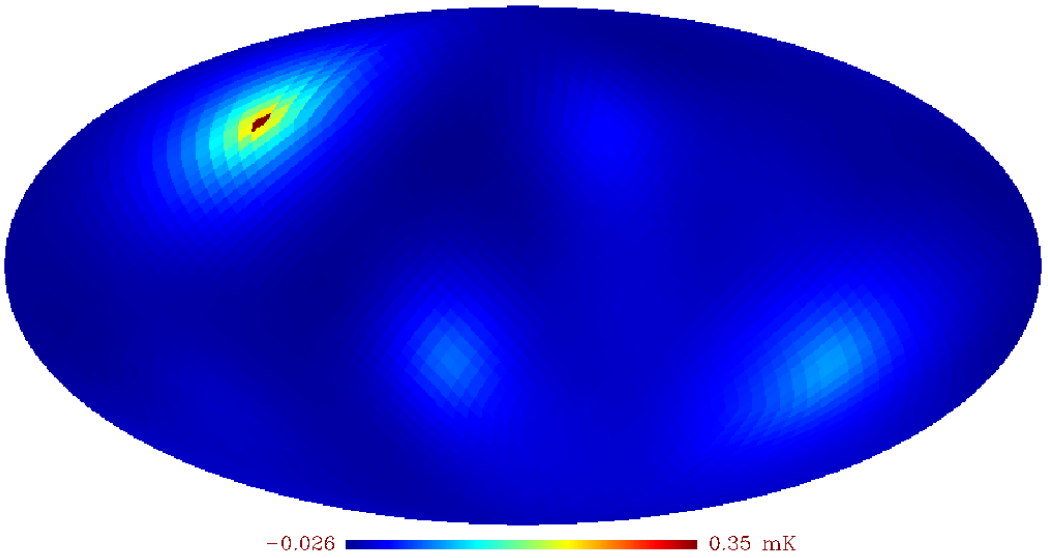

Figure 3.8: Visualization about the 500th pixel for the correlation matrix of space-I with an $\Omega_k = -1.26 \times 10^{-2}$ before smoothing

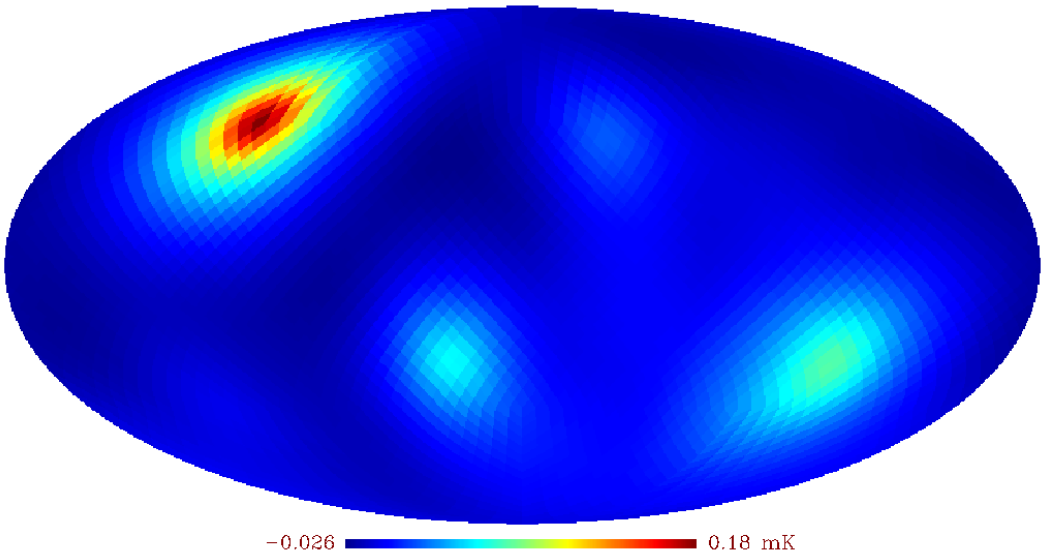

Figure 3.9: Visualization about the 500th pixel for the correlation matrix of space-I with an $\Omega_k = -1.26 \times 10^{-2}$ after smoothing

Now we must mask using our chosen analysis mask, because there are sections that after smoothing have been contaminated and must be removed for accuracy. The final map which is in figure 3.10, only has 1838 out of total 3072 pixels are unmasked. We smooth and then use an additional mask as regions near masked pixels will be corrupted after smoothing, this is because during the smoothing process these zeros will be spread out to the neighboring pixels.

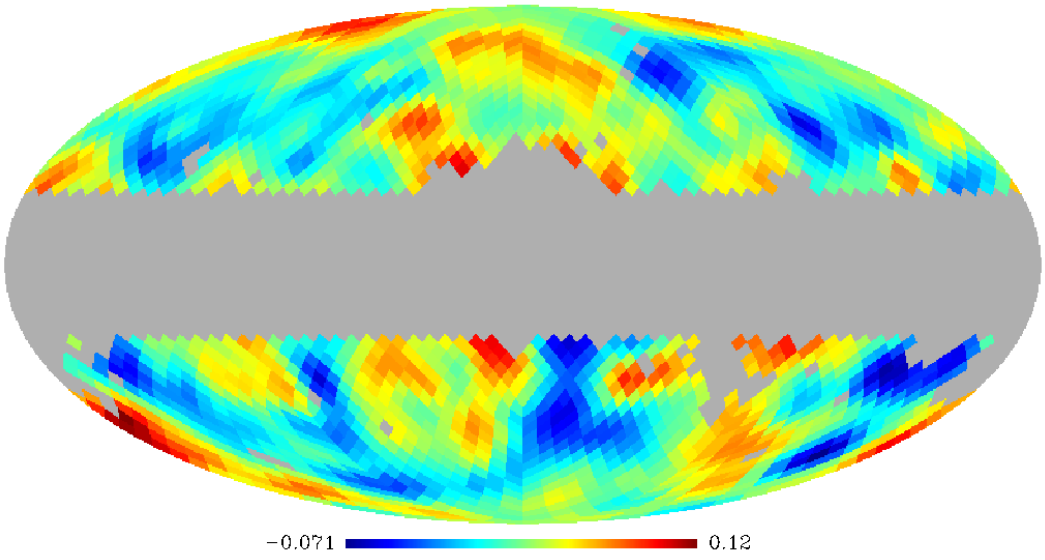

Figure 3.10: The $N_{\text{side}} = 16$ data map after it has been smoothed by the Gaussian beam with a FWHM= 492.0 *arcmin*, and masked by the chosen analysis mask.

3.2 Noise

The level of noise in the observed temperature at a particular pixel is determined by the noise of the instrument and the number of times the pixel has been observed. We calculate the noise variance per pixel n_i from the number of hits on each pixel h_i and the variance in the WMAP time stream data, σ.

$$n_i = \frac{\sigma^2}{h_i} \tag{3.3}$$

Both σ and h_i are quantities provided by the WMAP data release for pixels at the highest WMAP resolution which corresponds to $N_{\text{side}} = 512$. This formula assumes that the noise during each observation of the pixel is independent, which is appropriate since subsequent observations are significantly separated in time. As part of our analysis we re-bin the WMAP maps to lower, $N_{\text{side}} = 16$ resolution and recompute the noise accordingly, taking into account that the pre-masking

can mask out some high resolution pixels from the low resolution ones. Therefore the noise n_i for pixel i at $N_{\text{side}} = 16$ is reduced to,

$$n_i = \frac{\sigma^2}{\sum_j h_j}, \text{ where, } j \text{ is the index of the subpixels contained in pixel } i$$

Figure 3.11 shows the $N_{\text{side}} = 16$ noise map, with the typical noise level being around $1\mu K$, given that our ΔT from the data are around $100\mu K$, we have that the noise is about 1% of the signal.

The noise per pixels, observed multiple times is practically uncorrelated between the pixels. Therefore the noise correlation matrix is a diagonal matrix where the diagonal is simply, $\frac{\sigma^2}{h_i}$. The noise has to be smoothed and masked for consistency, which uses the same beam as the data smoothing. This is done using the same method as on the correlation matrix. Smoothing induces some cross correlation as can be seen in figure 3.12 which is the visualization of the correlation of the 500th pixel for the smoothed noise correlation matrix.

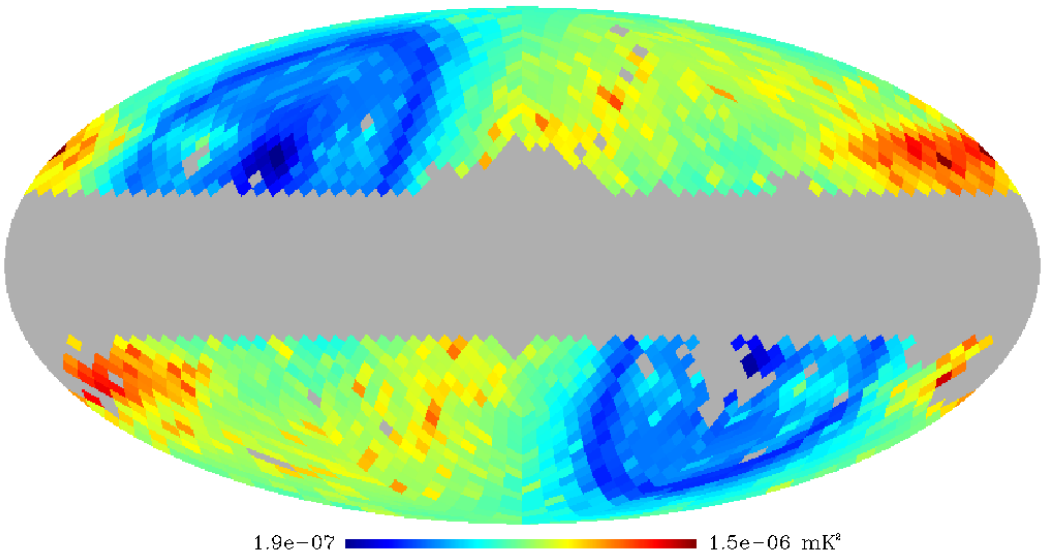

Figure 3.11: This is a visualization of the noise variance for each pixel, which are weighted by the number of observations in that pixel.

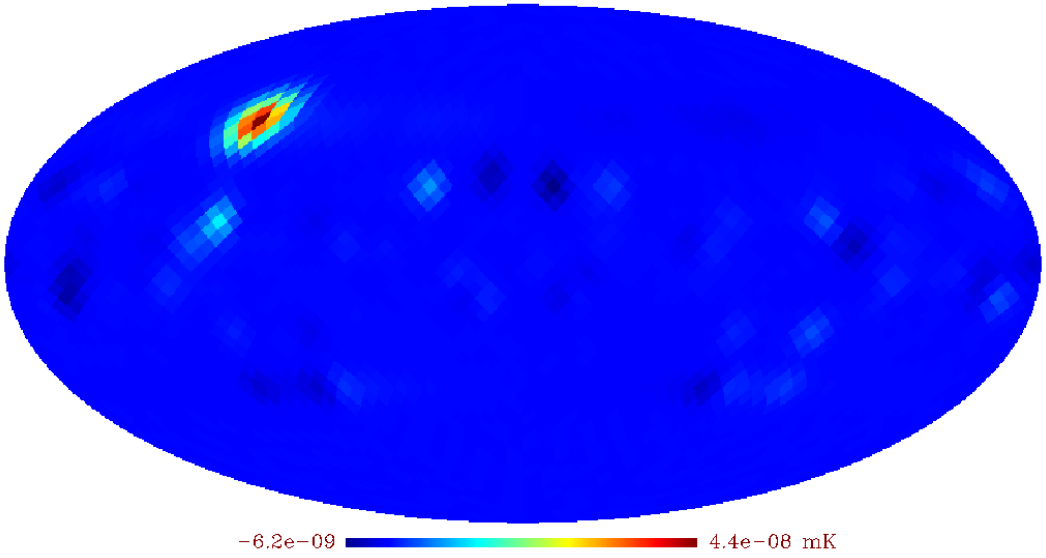

Figure 3.12: This is the visualization of the noise correlation matrix for pixel 500 after the smoothing. The correlation to other pixels is now noticeable.

3.3 The Basis Modes

Do to the nature of the likelihood function and its relation to the number of eigenmodes in the model, as seen in section 2.2.2, it can be difficult to compare models as their set of eigenvectors for **CT** can be different. To standardize all models with each other we use a set of basis eigenvectors such that we project all maps and matrices onto this basis and conduct the likelihood run in this projected mode space. This basis set of eigenvectors is from the fiducial model which corresponds to a flat isotropic Universe. A flat isotropic model was chosen as the fiducial model because all models can be extrapolated to this limit. When Ω_k approaches 0, this corresponds to the fundamental domain size approaching infinity, which increases isotropy of the observed Universe.

The correlation matrix of the fiducial map is constructed from the C_l values, which are obtained from the CAMB program using the LAMBDA website interface[3]. The cosmological parameters used are those from the 9-year WMAP data release when Ω_k is set to zero, this is Table 4 from the paper [Hinshaw et al. 2012]. The maximum log-likelihood value for this model was calculated and was determined to be $\ln(\mathcal{L}) = 3049.30$. This is indeed an isotropic space as can be seen from figure 3.13 which is the correlation for the 500th pixel of the fiducial model. Now that we have the set of basis eigenvectors we project the map and correlation

[3]Thanks to the lambda website for providing the online interface for the CAMB developed by Antony Lewis and Anthony Challinor, `http://lambda.gsfc.nasa.gov/toolbox/tb_camb_form.cfm`

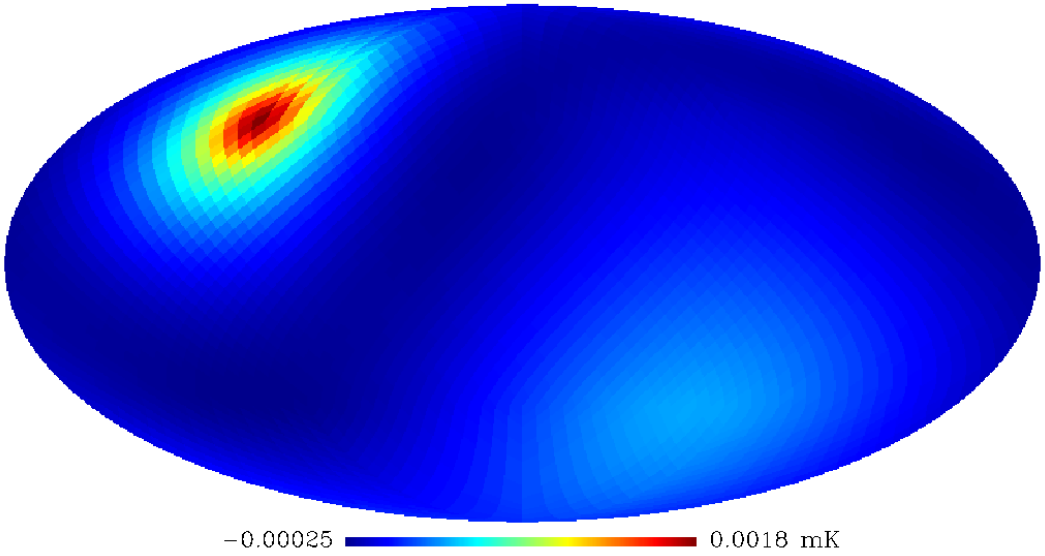

Figure 3.13: Visualization of the correlation for the 500th pixel for the fiducial model after smoothing.

matrices onto them. The number of modes used in the projection has to be chosen and the rest of the modes are simply projected out. For the correlation matrices,

$$\widetilde{\mathbf{C}} = \mathbf{\Psi C \Psi}^T \tag{3.4}$$

$\mathbf{\Psi}$ is a *nmodes* by *npix* matrix where each column of this matrix is a chosen eigenvector of the fiducial theoretical correlation matrix and $\mathbf{C}$ is our *npix* by *npix* correlation matrix, therefore we are left with $\widetilde{\mathbf{C}}$ which is a *nmodes* by *nmodes* matrix. For the map we have,

$$\widetilde{\mathbf{x}} = \mathbf{\Psi x} \tag{3.5}$$

Therefore the likelihood equation that we use for the computation of the likelihood value is then,

$$\ln(\mathcal{L}) = -\frac{1}{2}\left[np\ln(2\pi) + \ln(\det(\widetilde{\mathbf{CT}} + \widetilde{\mathbf{CN}})) + \widetilde{\mathbf{x}}^{\mathrm{T}}(\widetilde{\mathbf{CT}} + \widetilde{\mathbf{CN}})^{-1}\widetilde{\mathbf{x}}\right] \tag{3.6}$$

The number of modes that was chosen to be used in the computation of our likelihood is 837, the value of *nmodes* can be increased to 1200 before the degeneracy of the matrix makes it not behave properly.

3.4 Convergence

During the creation of the theoretical correlation matrix, we do not have any statistical knowledge for the orientation of our model to the data map. (α, β, γ)

represent the Euler angles for the orientation of the model to the sky, this provides three degrees of freedom when determining our maximum likelihood value. The amplitude for our theory A from model to model may vary slightly, therefore we must determine the best amplitude as well.

$$\ln(\mathcal{L}) = -\frac{1}{2}\ln(\det(A\widetilde{\mathbf{CT}}(\alpha,\beta,\gamma)+\widetilde{\mathbf{CN}})) + -\frac{\widetilde{\mathbf{x}}^T(A\widetilde{\mathbf{CT}}(\alpha,\beta,\gamma)+\widetilde{\mathbf{CN}})^{-1}\widetilde{\mathbf{x}}}{2} \quad (3.7)$$

To find the maximum likelihood value we must find the best amplitude at the best orientation for the model. For simplicity this is actually computed by minimizing the $-\ln(\mathcal{L})$ function[4]. Finding the best amplitude is simple, as the log-likelihood curve as a function of amplitude only has one peak, figure 3.14. We use the numerical recipes routine *brent* [Press et al. 2001] for the determination of the best amplitude. *Brent* is a useful routine for a one dimensional minimization, because there is no need to calculate any derivatives, also we can be sure of convergence from the start. Another useful option that *brent* offers is the *tol* option, which allows the user to set the precision for the minimization condition, where usually this is set to the machine's floating point precision. When we create the theoretical correlation matrix we know what the amplitude should roughly be, but since we are dealing with ln we do not want our best amplitude to be 1, as this would make $\ln(A) = 0$. As such we normalize our theory so that the best amplitude will be around 0.1.

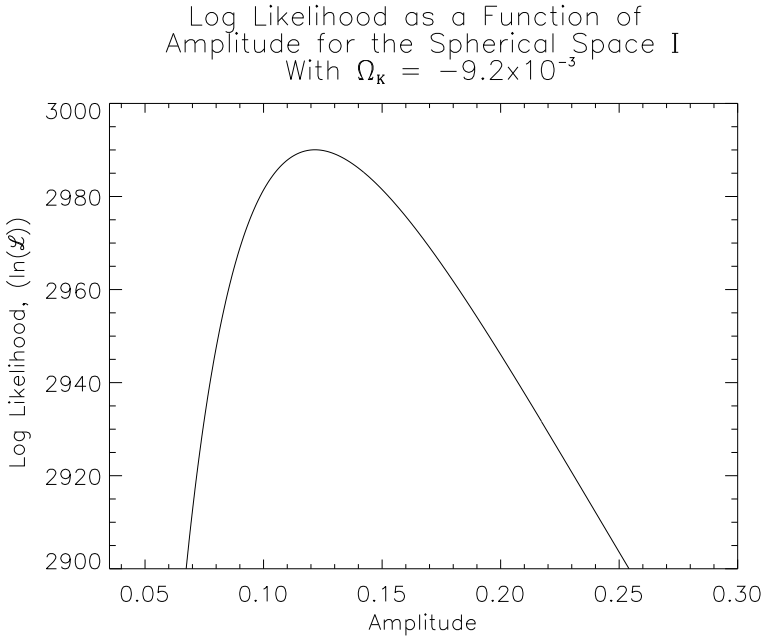

Figure 3.14: Log-likelihood value as a function of the amplitude for the spherical space I with $\Omega_k = -9.2 \times 10^{-3}$.

[4]This is because computationally it is easier since we using Numerical Recipes minimizing routines [Press et al. 2001]

The best orientation is significantly more troublesome to determine. There are three degrees of freedom, for the relative orientation of the model, as such we can not simply bracket the minimum and solve as with *brent*. For this, the numerical recipes routine *amoeba* is used [Press et al. 2001]. *Amoeba* is a down hill simplex method and in our case the simplex is a tetrahedron. This routine has a good convergence, and has the benefit of not requiring the calculation of derivatives in the rotation space, which in our case is not possible. The orientation of the model is described in Euler angles, because they describe the rotation of any three dimensional object. Euler angles unfortunately come with degeneracy, as such we actually minimize in a projected non-degenerate rotation space, to be sure that we will not have the case where two vertices of the simplex have different Euler angles that are in fact degenerate. To convert the Euler angles to the projected non-degenerate rotation space they are first converted into a unit quaternion q.

$$
\begin{aligned}
q_0 &= \cos(\frac{\beta}{2})\cos(\frac{\alpha+\gamma}{2}) \\
q_1 &= \sin(\frac{\beta}{2})\sin(\frac{\gamma-\alpha}{2}) \\
q_2 &= \sin(\frac{\beta}{2})\cos(\frac{\gamma-\alpha}{2}) \\
q_0 &= \cos(\frac{\beta}{2})\sin(\frac{\alpha+\gamma}{2})
\end{aligned}
$$

The unit quaternion lies on a 3-sphere of unit radius, which has a two to one correspondence of all possible rotations of the fundamental domain, therefore only half of the sphere is needed to describe all possible rotations. Unfortunately this rotation space is not very useful, so we project the hemisphere into $\mathbb{R}^3$, by stereographic projection from the south pole of the northern hemisphere[5]. The formula is exactly that for a 2-sphere case projected onto $\mathbb{R}^2$.

$$
u_i = \frac{q_i}{2/(1+q_0)}, \quad \text{for } i = 1, 2, 3 \tag{3.8}
$$

This is the projected non-degenerate rotation space where the *amoeba* simplex walks. For each orientation we have to run the *brent* routine and determine its best amplitude, thus determining the maximum log-likelihood value for that specific orientation. The likelihood space of angles is not a nice smooth domain, but is riddled with many local minima and maxima. This poses a problem as *amoeba* tends to get stuck in these local minima. Figure 3.15 shows a slice of the $\mathbb{R}^3$ non-degenerate rotation space.

The obvious choice to correct this would be with the use of an annealing parameter, but this parameter would not solve this problem as the minima are

[5]From the south pole we draw a line to the rotation point on the northern hemisphere, where the line intersects with $\mathbb{R}^3$ is the value for our rotation u.

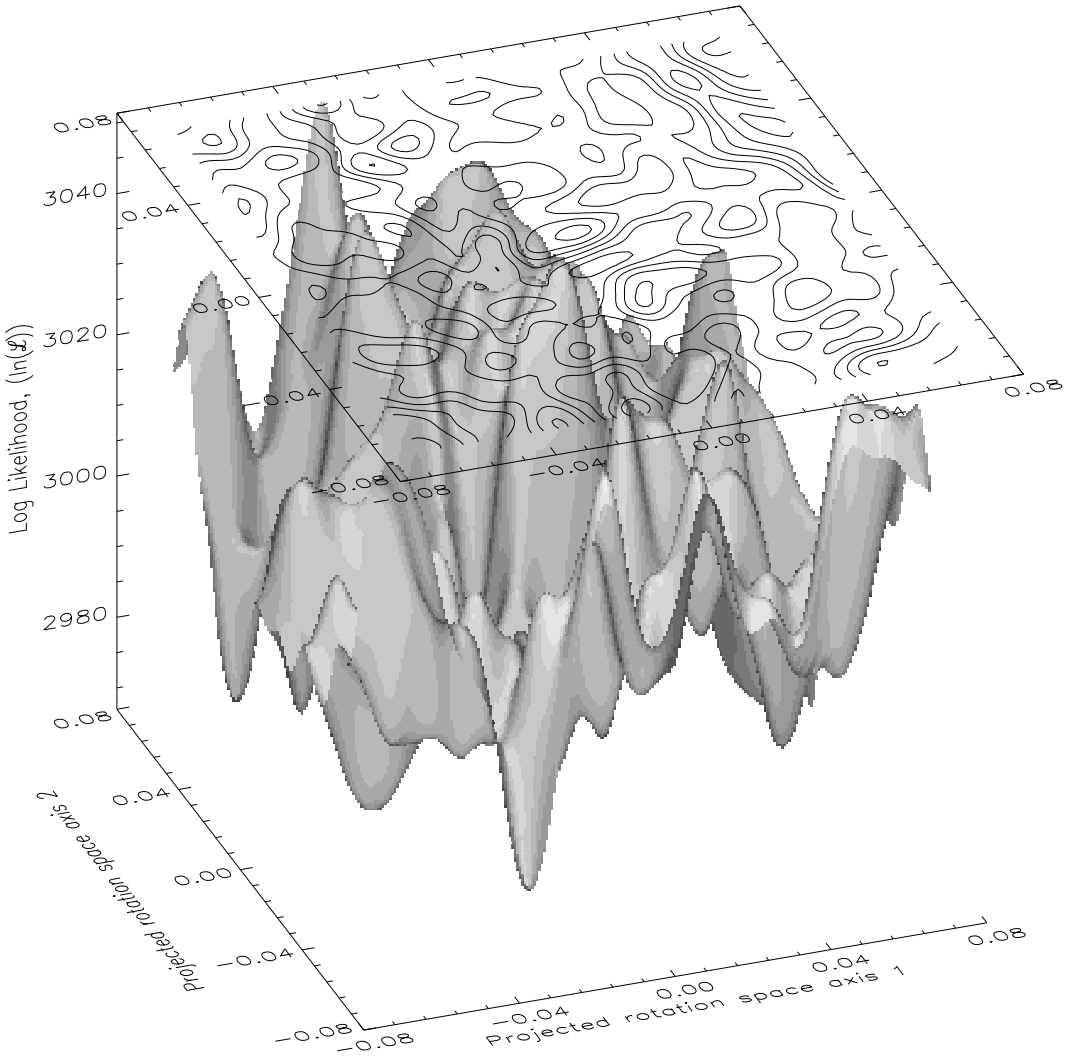

Figure 3.15: The maximum log-likelihood value as a function of two projected non-degenerate rotation space coordinates $u(1)$ and $u(2)$ for the spherical space I with $\Omega_k = 9.2 \times 10^{-3}$. Note: the slice is of the plane where $u(3) = 0.0$ and has a resolution of $\Delta u = 0.0014$.

quite localized and not board enough to make this method effective. The initial starting position and size of the simplex, has an effect on the convergence to a specific minima. Therefore to solve this problem we have chosen to run a set of likelihood runs, given different and randomly chosen initial simplexes, where the largest likelihood value out of these runs is then chosen as our final maximum log-likelihood for the model. In our investigation we started with 20 randomly chosen simplexes. During the investigation a few runs were done to a higher iteration count but with little effect, as such 20 iterations will most likely contain the maximum log-likelihood value for the model.

3.5 Map Making

It is useful to be able to randomly realize a map based on a theoretical correlation matrix, as you can then use the generated map as a test for a positive case result [Planck Collaboration et al. 2013b]. To realize a map from a correlation matrix $\mathbf{C}$, a set of random values $\mathbf{y}$ which follow a univariant and uncorrelated Gaussian distribution with zero mean, $\langle \mathbf{y}\mathbf{y}^T \rangle = \mathbf{I}$, is used. Let $\mathbf{x} = \mathbf{C}^{\frac{1}{2}}\mathbf{y}$, where $\mathbf{C} = \mathbf{C}^{\frac{1}{2}}\mathbf{C}^{\frac{1}{2}}$. $\mathbf{C}$ is positive semidefinite and symmetric, therefore $\mathbf{C}^{\frac{1}{2}}$ will also be positive semidefinite and symmetric. We compute the following to see if the relation $\langle \mathbf{x}\mathbf{x}^T \rangle = \mathbf{C}$ still holds.

$$\langle \mathbf{x}\mathbf{x}^T \rangle = \left\langle [\mathbf{C}^{\frac{1}{2}}\mathbf{y}][\mathbf{C}^{\frac{1}{2}}\mathbf{y}]^T \right\rangle = \left\langle \mathbf{C}^{\frac{1}{2}}\mathbf{y}\mathbf{y}^T\mathbf{C}^{\frac{1}{2}T} \right\rangle = \mathbf{C}^{\frac{1}{2}} \langle \mathbf{y}^T\mathbf{y} \rangle \mathbf{C}^{\frac{1}{2}T} = \mathbf{C}$$

Therefore we can realize a map based on the correlation matrix $\mathbf{CT}$ by,

$$\boxed{\mathbf{x} = \mathbf{CT}^{\frac{1}{2}}\mathbf{y}} \tag{3.9}$$

Taking a square root of the covariance matrix is easily achieved in eigenmode decomposition $\mathbf{CT} = \mathbf{\Psi}\mathbf{\Lambda}\mathbf{\Psi}^T$. $\mathbf{\Psi}$ is a $np \times np$ matrix and the columns of this matrix are the $\mathbf{CT}$'s eigenvectors. $\mathbf{\Lambda}$ is a $np \times np$ diagonal matrix consisting of the eigenmodes.

$$\mathbf{CT} = \mathbf{\Psi}\mathbf{\Lambda}\mathbf{\Psi}^T = \mathbf{CT}^{\frac{1}{2}}\mathbf{CT}^{\frac{1}{2}} \tag{3.10}$$

$$\therefore \ \mathbf{CT}^{\frac{1}{2}} = \mathbf{\Psi}\mathbf{\Lambda}^{\frac{1}{2}} \tag{3.11}$$

$\mathbf{\Lambda}$ is a diagonal matrix therefore,

$$\mathbf{\Lambda}^{\frac{1}{2}} = \begin{bmatrix} \lambda_{12}^{\frac{1}{2}} & 0 & \cdots & 0 \\ 0 & \lambda_{22}^{\frac{1}{2}} & \cdots & 0 \\ \vdots & \vdots & \ddots & \vdots \\ 0 & 0 & \cdots & \lambda_{np\,np}^{\frac{1}{2}} \end{bmatrix} \tag{3.12}$$

The noise component of the matrix can also be realized, in exactly the same manner by using another set of random univariate Gaussian numbers $\mathbf{y}'$. The noise is not correlated with the signal, therefore our final map realization is:

$$\mathbf{map} = \mathbf{CT}^{\frac{1}{2}}\mathbf{y} + \mathbf{CN}^{\frac{1}{2}}\mathbf{y}' \tag{3.13}$$

Figures 3.16, 3.17, 3.18 and 3.19 are some realized maps for different $\mathbf{y}$ and $\mathbf{CT}$.

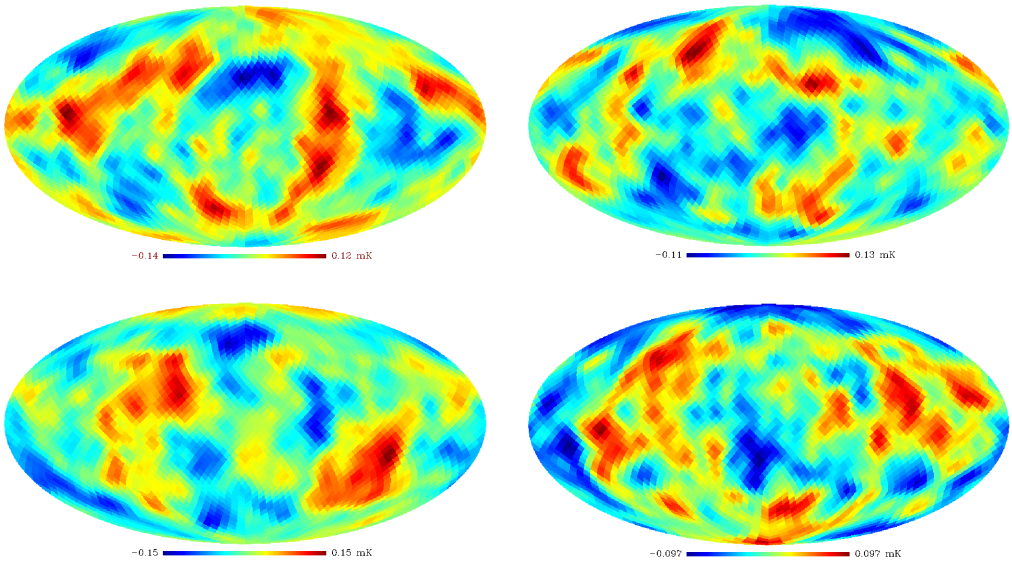

Figure 3.16: Four randomly generated maps for the space-I with $\Omega_k = -5.4 \times 10^{-3}$.

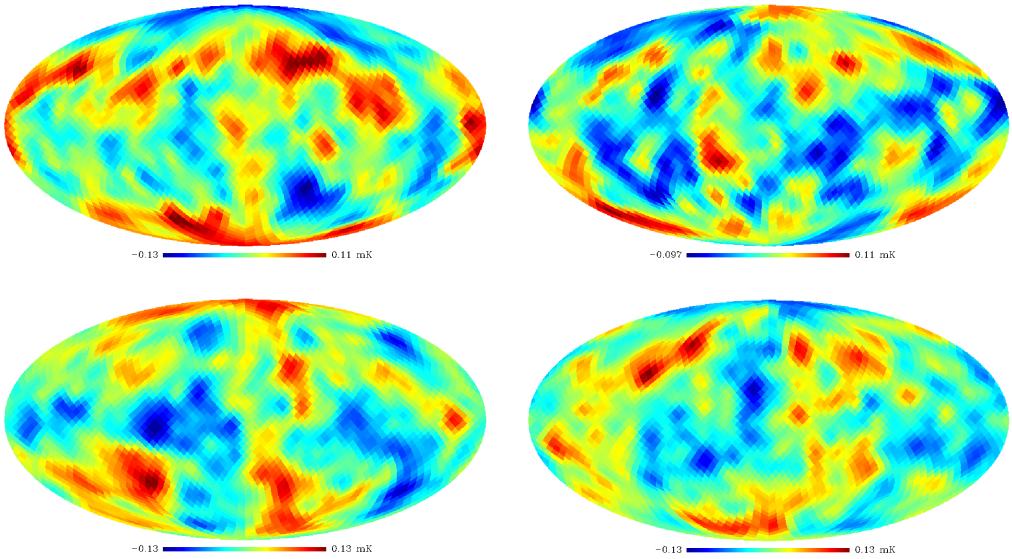

Figure 3.17: Four randomly generated maps for the space-I with $\Omega_k = -9.0 \times 10^{-3}$.

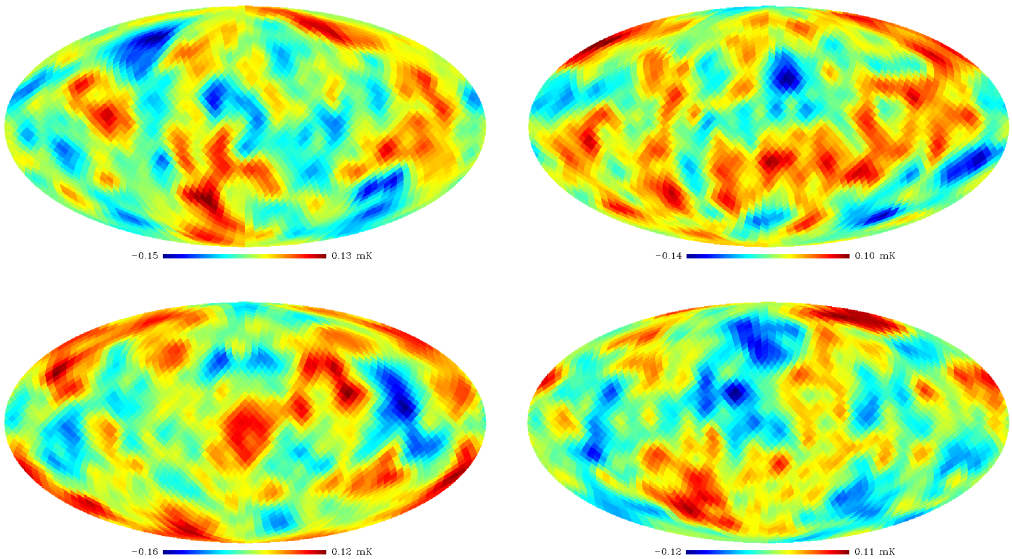

Figure 3.18: Four randomly generated maps for the space-I with $\Omega_k = -1.28 \times 10^{-2}$.

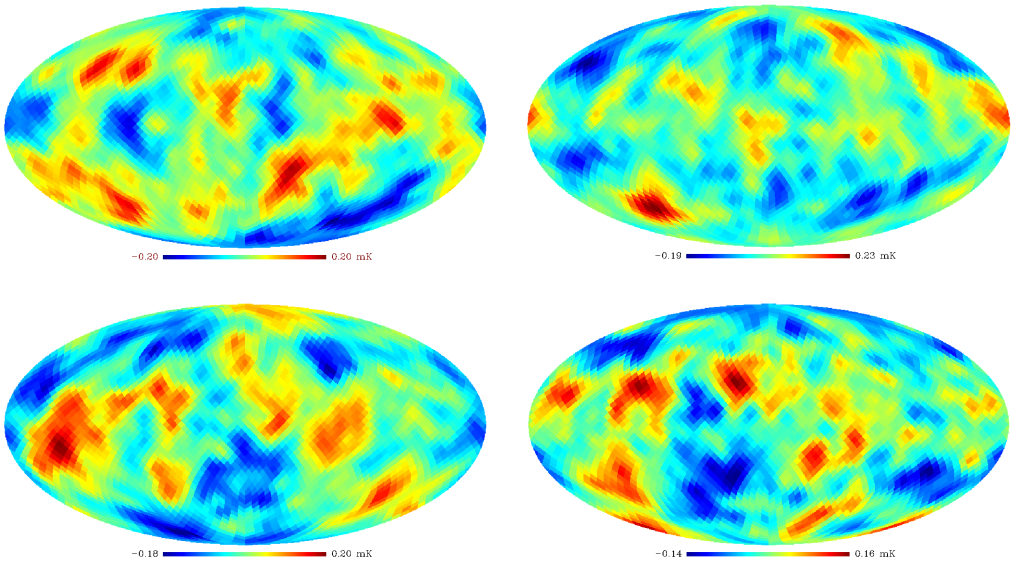

Figure 3.19: Four randomly generated maps for the isotropic fiducial map.

Chapter 4

Investigation

The region of parameter space where the curvature of the Universe is such that the horizon of last scattering approaches the boundary of the domain is of particular interest. It is in this region where the size of domain decreases below the last scattering radius, that the visible Universe looses its isotropy and the correlations between sections of the sky, become more prominent.

There is a reference point at which the boundary of the domain and the horizon intersect. This occurs at a specific Ω_k value for the specific multiconnected space. This point is where Ω_k is such that the horizon of last scattering first touches the boundary of the fundamental domain, i.e is equal to the radius of the sphere *inscribed* into domain, χ_{insc}.

To construct the **CT** matrix we have the set of isometries that describe the tiling of the universal cover by the fundamental domain. This information provides the distance between the two nearest image domains, which is directly related to χ_{insc}. With the value of χ_{insc} for the given multiconnected space, we can then compare to the distance of the last scattering horizon, and determine at which respective Ω_k value is where the last scattering surface has a radius corresponding to the inscribed sphere of the fundamental domain.

The likelihood code was then run for a sampling of discrete Ω_k values near the inscribed region and beyond to where boundary and horizon intersect. The main results were obtained with the parameters values that are on what is called the degeneracy line, shown in figure 4.1. Along the degeneracy line the parameters change in such way as to keep the position of power spectrum peaks and therefore most of high l modes fixed as Ω_k varies. This is important, as previously stated we do not use higher frequency l in our investigation. These higher frequencies are well known and contain much of the information about the cosmological parameters of the Universe, as such we want these high l to remain constant as we vary Ω_k. Along this degeneracy line Ω_Λ is calculated using equation 4.1. The value of the Hubble constant also changes with Ω_k along this degeneracy line,

following equation 4.2.

$$\Omega_\Lambda(\Omega_k) = \Omega_\Lambda(0) + 2.7049\ \Omega_k \tag{4.1}$$

$$H_0(\Omega_k) = H_0(0) + \Omega_k\ (388.0 + 1200.0\Omega_k) \tag{4.2}$$

Ω_m is calculated from Ω_k and Ω_Λ using the equation, $\Omega_m = 1.0 - \Omega_k - \Omega_\Lambda$. We also obtained runs for when Ω_Λ and the Hubble constant are held constant as Ω_k varies. Both parameter lines used are shown in figure 4.1. The fiducial model lies at their intersection with the flat space line.

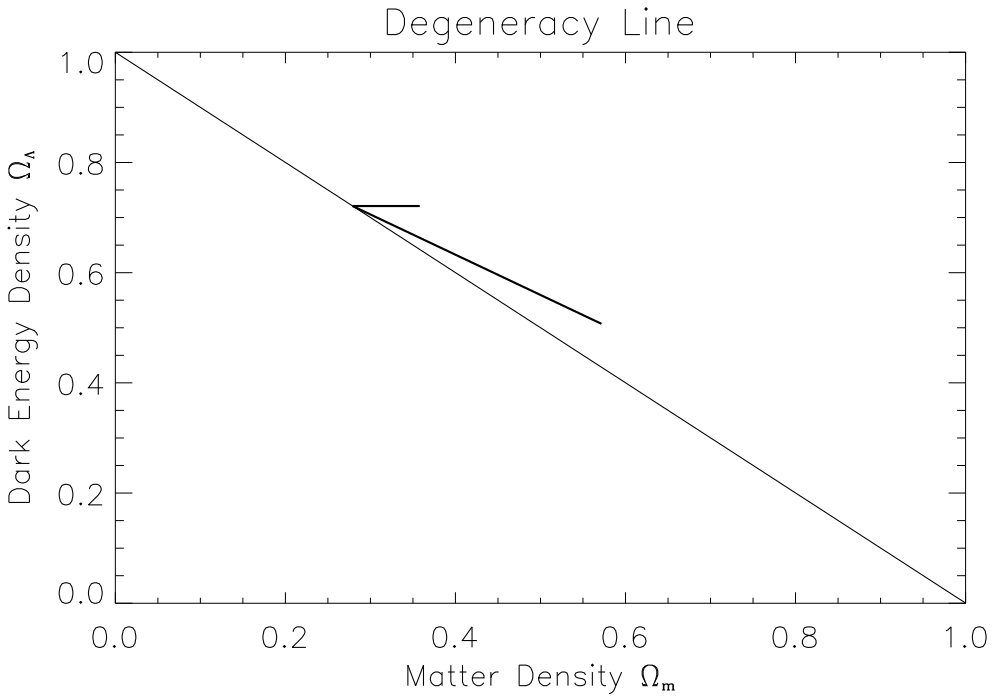

Figure 4.1: Plot of the parameter degeneracy line for $\Omega_k \in [-0.079, 0]$, this is inside the acceptable range for Ω_k as measured by WMAP (table 1.1). Above the diagonal line $\Omega_m + \Omega_\Lambda = 1.0$ is the closed space, and below is the open space. Along the line is the flat space. The horizontal line at $\Omega_\Lambda = 0.721$ corresponds to the parameters of the models when Ω_Λ is held constant.

4.1 Results for the Three Multiconnected Spaces

Three multiconnected spaces for the spherical universal cover are investigated. These three were chosen and out of the five for the spherical universal cover, as these three are more restrictive than the lens and polyhedral domains, that have infinitely many possibilities both in size and in shape. The results for likelihood analysis presented in this section are the main results of this thesis. They are discussed and tested in the following sections.

4.1.1 Space-I

This is a popular multiconnected space used when investigating the shape of our Universe, as it fits reasonably well to the quadrapole and octupole suppression as observed in the COBE and WMAP data [Luminet et al. 2003]. This is a multiconnected space with a fundamental domain shape that consists of a regular dodecahedron. Using our knowledge of the distribution of domains, we have that

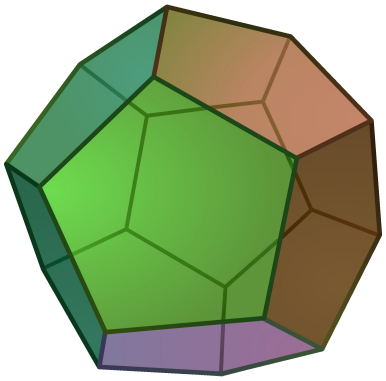

Figure 4.2: Shape of a regular dodecahedron as seen in flat space. Image taken from `http://upload.wikimedia.org/wikipedia/commons/6/66/POV-Ray-Dodecahedron.svg`, used under the terms of the GNU Free Documentation License.

the distance between the two closest domains is $0.2R_0$, R_0 being the curvature radius. Since the inscribed sphere touches the center of each face we therefore determine that $\chi_{insc} = 0.1R_0$. By calculating when χ_{insc} and the distance to the surface of last scattering are equal we can determine the respective Ω_k value when this happens. We calculated that for this multiconnected space, $\Omega_k \approx -9.9 \times 10^{-3}$ when the horizon has a radius that corresponds to χ_{insc}. Figure 4.3 shows the maximum log-likelihood curve for the varying Ω_k along the parameter degeneracy line, the lower panel is for a wider range of Ω_k, and upper panel zoomed in near the transition region. There are three features to this curve worth taking note of, the smooth region up to the vertical line, the bump at the vertical line and the disjointed decreasing region after the vertical line. The table 4.1 contains a portion of the Ω_k sampling values with corresponding relevant distances and cosmological parameters, as such we can see how varying Ω_k affects the parameters of the Universe.

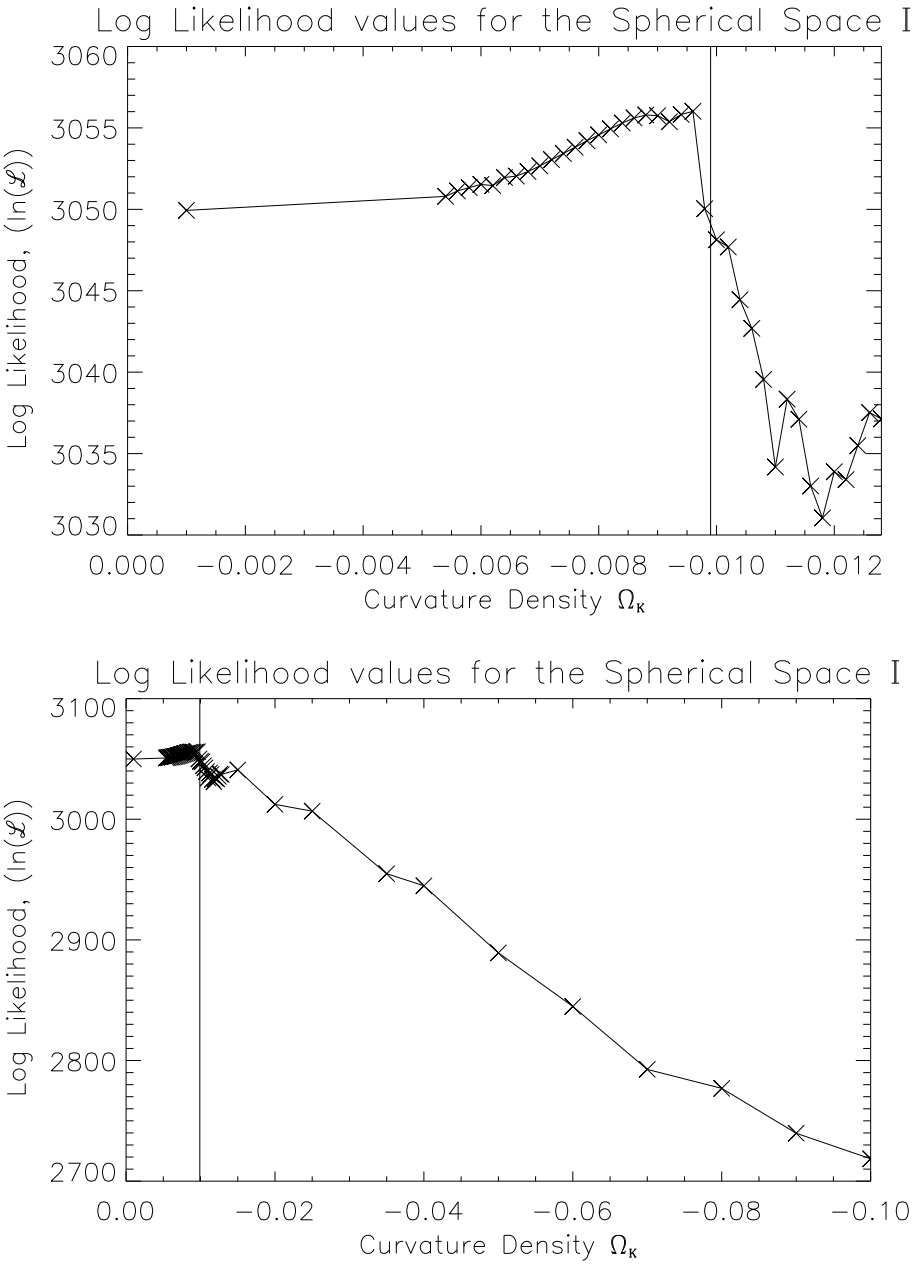

Figure 4.3: Maximum log-likelihood for the spherical multiconnected space-I as the function of Ω_k varying along the degeneracy line. The vertical line is the value of Ω_k when the horizon first touches the boundary of the fundamental domain.

Table 4.1: Parameters for the Ω_k Sampling Along the Degeneracy Line for Space-I

Ω_k	χ_{LSS} $(\frac{c}{H_0})$	χ_{Bound} $(\frac{c}{H_0})$	$\frac{\chi_{LSS}}{\chi_{Bound}}$ $(\frac{Km/s}{Mpc})$	H_0	Ω_Λ	Ω_m
-.0010	3.2888	9.9346	0.3310	69.6132	.7253	.2756
-.0054	3.2176	4.2752	0.7526	67.9398	.7134	.2919
-.0056	3.2145	4.1981	0.7657	67.8648	.7129	.2927
-.0058	3.2114	4.1251	0.7785	67.7900	.7123	.2934
-.0060	3.2083	4.0558	0.7910	67.7152	.7118	.2941
-.0070	3.1930	3.7549	0.8503	67.3428	.7091	.2978
-.0076	3.1839	3.6037	0.8835	67.1205	.7074	.3001
-.0082	3.1749	3.4693	0.9151	66.8991	.7058	.3023
-.0084	3.1720	3.4278	0.9254	66.8255	.7053	.3030
-.0086	3.1690	3.3877	0.9354	66.7520	.7047	.3038
-.0088	3.1660	3.3489	0.9454	66.6785	.7042	.3045
-.0090	3.1631	3.3115	0.9552	66.6052	.7037	.3052
-.0092	3.1602	3.2753	0.9648	66.5320	.7031	.3060
-.0094	3.1572	3.2403	0.9744	66.4588	.7026	.3067
-.0096	3.1543	3.2064	0.9838	66.3858	.7020	.3075
-.0098	3.1514	3.1735	0.9930	66.3128	.7015	.3082
-.0100	3.1485	3.1416	1.0022	66.2400	.7010	.3090
-.0102	3.1456	3.1106	1.0112	66.1672	.7004	.3097
-.0104	3.1427	3.0806	1.0202	66.0946	.6999	.3104
-.0106	3.1398	3.0514	1.0290	66.0220	.6993	.3112
-.0108	3.1370	3.0230	1.0377	65.9496	.6988	.3119
-.0122	3.1172	2.8443	1.0960	65.4450	.6950	.3171
-.0124	3.1144	2.8212	1.1039	65.3733	.6945	.3178
-.0126	3.1116	2.7988	1.1118	65.3017	.6939	.3186
-.0128	3.1088	2.7768	1.1196	65.2302	.6934	.3193
-.0200	3.0141	2.2214	1.3568	62.7200	.6739	.3460
-.0250	2.9537	1.9869	1.4866	61.0500	.6604	.3645
-.0350	2.8442	1.6793	1.6937	57.8900	.6333	.4015
-.0400	2.7944	1.5708	1.7789	56.4000	.6198	.4201
-.0500	2.7028	1.4050	1.9237	53.6000	.5928	.4571
-.0600	2.6205	1.2825	2.0432	51.0400	.5657	.4941
-.0700	2.5461	1.1874	2.1442	48.7200	.5387	.5312
-.0800	2.4782	1.1107	2.2312	46.6400	.5116	.5682
-.0900	2.4161	1.0472	2.3072	44.8000	.4846	.6052
-.1000	2.3588	0.9935	2.3744	43.2000	.4575	.6423

χ_{Bound} is the distance to the boundary.

4.1.2 Space-T

Space-T is a multiconnected space where the fundamental domain shape is that of a regular octahedron. It is shown in Figure 4.4. From the tiling of the 3-sphere

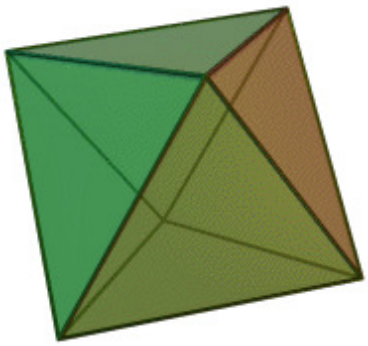

Figure 4.4: Shape of a regular octahedron as seen in flat space. Image taken from `http://upload.wikimedia.org/wikipedia/commons/0/07/Octahedron.svg`, used under the terms of the GNU Free Documentation License.

by these domains we have that the distance between the two closest domains is $0.\bar{3}R_0$. Therefore the inscribed radius is $\chi_{insc} = 0.1\bar{6}R_0$. Just as for Space-I, we calculated that when the horizon first touches the boundary occurs when $\Omega_k \approx -3.30 \times 10^{-2}$. Figure 4.5 shows the maximum log-likelihood curve for the chosen Ω_k sampling, for space-T, along the parameter degeneracy line. There are three features to this curve that are the same as for space-I. The table 4.2 contains a portion of the Ω_k sampling values with corresponding relevant distances and cosmological parameters.

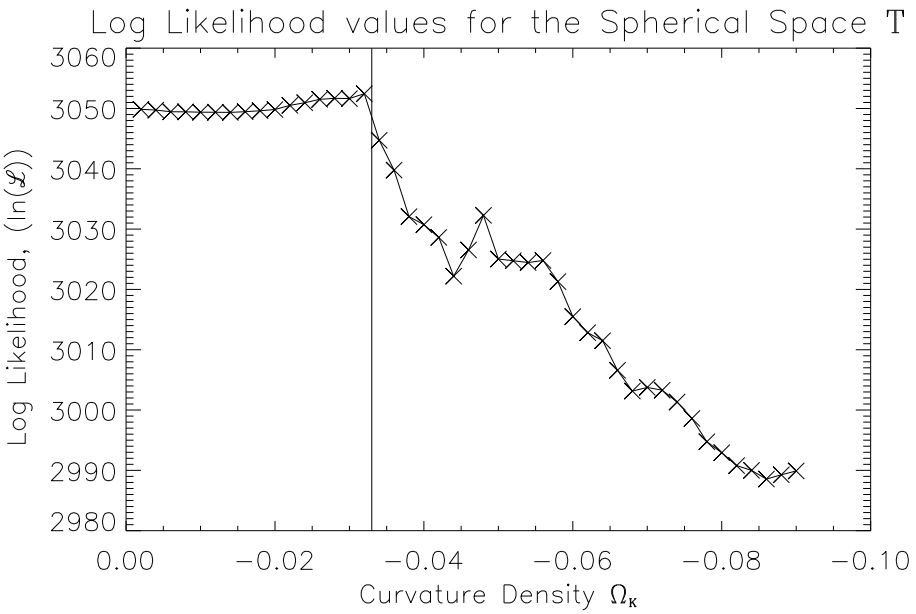

Figure 4.5: Maximum log-likelihood for the spherical multiconnected space-T as the function of Ω_k varying along the parameter degeneracy line. The vertical line is the value of Ω_k when the horizon first touches the boundary of the fundamental domain.

Table 4.2: Parameters for the Ω_k Sampling Along the Degeneracy Line of Space-T

Ω_k	χ_{LSS} $(\frac{c}{H_0})$	χ_{Bound} $(\frac{c}{H_0})$	$\frac{\chi_{LSS}}{\chi_{Bound}}$ $(\frac{Km/s}{Mpc})$	H_0	Ω_Λ	Ω_m
-.0020	3.2721	11.7080	0.2795	69.2288	.7226	.2793
-.0040	3.2397	8.2788	0.3913	68.4672	.7172	.2867
-.0060	3.2083	6.7596	0.4746	67.7152	.7118	.2941
-.0100	3.1485	5.2360	0.6013	66.2400	.7010	.3090
-.0120	3.1200	4.7798	0.6527	65.5168	.6955	.3164
-.0140	3.0923	4.4252	0.6988	64.8032	.6901	.3238
-.0160	3.0655	4.1394	0.7406	64.0992	.6847	.3312
-.0200	3.0141	3.7024	0.8141	62.7200	.6739	.3460
-.0220	2.9894	3.5301	0.8468	62.0448	.6685	.3534
-.0240	2.9654	3.3798	0.8774	61.3792	.6631	.3608
-.0260	2.9421	3.2472	0.9060	60.7232	.6577	.3682
-.0300	2.8972	3.0230	0.9584	59.4400	.6469	.3830
-.0320	2.8756	2.9270	0.9824	58.8128	.6414	.3904
-.0340	2.8546	2.8396	1.0053	58.1952	.6360	.3978
-.0360	2.8340	2.7596	1.0270	57.5872	.6306	.4053
-.0400	2.7944	2.6180	1.0674	56.4000	.6198	.4201
-.0420	2.7752	2.5549	1.0862	55.8208	.6144	.4275
-.0440	2.7565	2.4962	1.1043	55.2512	.6090	.4349
-.0460	2.7382	2.4413	1.1216	54.6912	.6036	.4423
-.0500	2.7028	2.3416	1.1542	53.6000	.5928	.4571
-.0520	2.6856	2.2961	1.1696	53.0688	.5873	.4645
-.0540	2.6688	2.2532	1.1845	52.5472	.5819	.4719
-.0560	2.6524	2.2126	1.1988	52.0352	.5765	.4793
-.0600	2.6205	2.1376	1.2259	51.0400	.5657	.4941
-.0620	2.6050	2.1028	1.2388	50.5568	.5603	.5015
-.0640	2.5899	2.0697	1.2513	50.0832	.5549	.5089
-.0660	2.5750	2.0381	1.2634	49.6192	.5495	.5164
-.0700	2.5461	1.9790	1.2865	48.7200	.5387	.5312
-.0720	2.5320	1.9513	1.2976	48.2848	.5332	.5386
-.0740	2.5182	1.9248	1.3083	47.8592	.5278	.5460
-.0760	2.5046	1.8993	1.3187	47.4432	.5224	.5534
-.0800	2.4782	1.8512	1.3387	46.6400	.5116	.5682
-.0820	2.4654	1.8285	1.3483	46.2528	.5062	.5756
-.0840	2.4527	1.8066	1.3577	45.8752	.5008	.5830
-.0860	2.4403	1.7855	1.3668	45.5072	.4954	.5904
-.0900	2.4161	1.7453	1.3843	44.8000	.4846	.6052

χ_{Bound} is the distance to the boundary.

4.1.3 Space-O

Space-O is a multiconnected space where the fundamental domain shape consists of a regular truncated cube, as shown in Figure 4.6. Using the distribution of

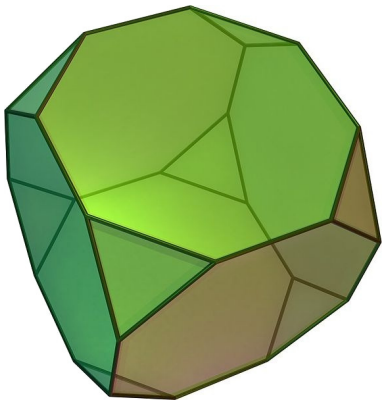

Figure 4.6: Shape of a regular truncated cube as seen in flat space. Image taken from `http://upload.wikimedia.org/wikipedia/commons/c/c0/Truncatedhexahedron.jpg`, used under the terms of the GNU Free Documentation License.

domains we have that the distance between the two closest domains is $0.25R_0$ and that the radius of the inscribed sphere is $\chi_{insc} = 0.125R_0$. Just as for space-I and space-T we are able to calculate that $\Omega_k \approx -1.65 \times 10^{-2}$ for when the horizon of last scattering first touches the boundary of the multiconnected space. Figure 4.7, is the maximum log-likelihood curve for the chosen Ω_k sampling in space-O, along the parameter degeneracy line. There are three features to this curve that are the same as the previous 2 multiconnected spaces. Table 4.3 contains a portion of the Ω_k sampling values with corresponding relevant distances and cosmological parameters.

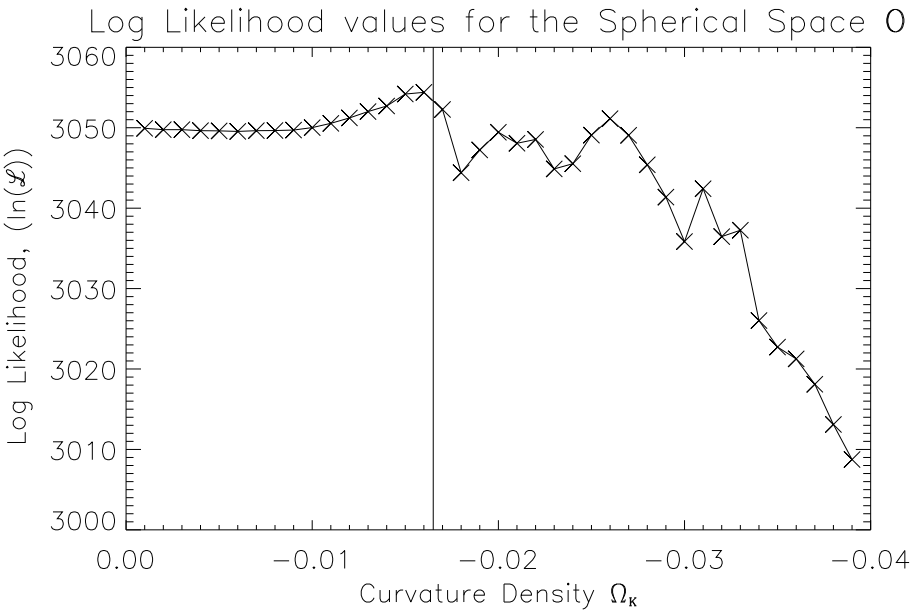

Figure 4.7: Maximum log-likelihood for the spherical multiconnected space-O as a function of Ω_k varying along the parameter degeneracy line. The vertical line is the value of Ω_k when the horizon first touches the boundary of the space.

Table 4.3: Parameters for the Ω_k Sampling Along the Degeneracy Line for Space-O

Ω_k	$\chi_{\rm LSS}$ $(\frac{c}{H_0})$	χ_{Bound} $(\frac{c}{H_0})$	$\frac{\chi_{LSS}}{\chi_{Bound}}$ $(\frac{Km/s}{Mpc})$	H_0	Ω_Λ	Ω_m
-.0010	3.2888	12.4182	0.2648	69.6132	.7253	.2756
-.0020	3.2721	8.7810	0.3726	69.2288	.7226	.2793
-.0030	3.2558	7.1697	0.4541	68.8468	.7199	.2830
-.0040	3.2397	6.2091	0.5218	68.4672	.7172	.2867
-.0050	3.2239	5.5536	0.5805	68.0900	.7145	.2904
-.0060	3.2083	5.0697	0.6328	67.7152	.7118	.2941
-.0070	3.1930	4.6937	0.6803	67.3428	.7091	.2978
-.0080	3.1779	4.3905	0.7238	66.9728	.7064	.3015
-.0090	3.1631	4.1394	0.7641	66.6052	.7037	.3052
-.0100	3.1485	3.9270	0.8018	66.2400	.7010	.3090
-.0110	3.1341	3.7442	0.8371	65.8772	.6982	.3127
-.0120	3.1200	3.5848	0.8703	65.5168	.6955	.3164
-.0130	3.1060	3.4442	0.9018	65.1588	.6928	.3201
-.0140	3.0923	3.3189	0.9317	64.8032	.6901	.3238
-.0150	3.0788	3.2064	0.9602	64.4500	.6874	.3275
-.0160	3.0655	3.1046	0.9874	64.0992	.6847	.3312
-.0170	3.0523	3.0119	1.0134	63.7508	.6820	.3349
-.0180	3.0394	2.9270	1.0384	63.4048	.6793	.3386
-.0190	3.0266	2.8489	1.0624	63.0612	.6766	.3423
-.0200	3.0141	2.7768	1.0854	62.7200	.6739	.3460
-.0210	3.0017	2.7099	1.1077	62.3812	.6712	.3497
-.0220	2.9894	2.6476	1.1291	62.0448	.6685	.3534
-.0230	2.9774	2.5894	1.1498	61.7108	.6658	.3571
-.0240	2.9654	2.5349	1.1699	61.3792	.6631	.3608
-.0250	2.9537	2.4836	1.1893	61.0500	.6604	.3645
-.0260	2.9421	2.4354	1.2081	60.7232	.6577	.3682
-.0270	2.9307	2.3899	1.2263	60.3988	.6550	.3719
-.0280	2.9194	2.3468	1.2440	60.0768	.6523	.3756
-.0290	2.9082	2.3060	1.2612	59.7572	.6496	.3793
-.0300	2.8972	2.2672	1.2779	59.4400	.6469	.3830
-.0310	2.8864	2.2304	1.2941	59.1252	.6441	.3867
-.0320	2.8756	2.1953	1.3099	58.8128	.6414	.3904
-.0330	2.8650	2.1617	1.3253	58.5028	.6387	.3941
-.0340	2.8546	2.1297	1.3404	58.1952	.6360	.3978
-.0350	2.8442	2.0991	1.3550	57.8900	.6333	.4015
-.0360	2.8340	2.0697	1.3693	57.5872	.6306	.4053
-.0370	2.8239	2.0415	1.3832	57.2868	.6279	.4090
-.0380	2.8139	2.0145	1.3968	56.9888	.6252	.4127
-.0390	2.8041	1.9885	1.4101	56.6932	.6225	.4164

χ_{Bound} is the distance to the boundary.

4.1.4 Summary of the Three Spaces Results

All three spaces show the same three distinct features in their log-likelihood curves. There are two distinct regions to the curve, a smooth region when Ω_k is close to 0 and a disjointed non-monotonically decreasing tail region when Ω_k is such that the distance to the horizon of last scattering is larger than the size of the compact space. All three curves have a bump of $\Delta \ln \mathcal{L} = 6.0$ for space-I, $\Delta \ln \mathcal{L} = 2.6$ for space-T, and $\Delta \ln \mathcal{L} = 4.5$ for space-O. This bump occurs at the region where the horizon first intersects with the boundary. The fact that all three show this bump is interesting and is an indication that this is not a detection for a specific topology but rather the possibility of some alignment of features of our single realization of the CMB sky that we observe.

4.2 Discussion

One of the most intriguing features that all obtained likelihood curves exhibit is some (at the level of $\Delta \ln L = few$) enhancement of the likelihood for models with the space size just near the diameter of LSS versus the infinite isotropic models. This enhancement slowly accumulates as Ω_k reaches this critical value, while for smaller spaces the likelihood quickly drops. This enhancement is equally observed in all topological models studied, and even when the multiconnected $\mathbf{CT}_{pp'}$ is compared with a random realization from knowingly isotropic model. Thus it cannot be understood as a detection of a specific topology, but what is then the origin of the effect?

Each realization of the CMB sky has some distinct features to it, which can be seen in figure 3.4. Even though the mechanism of CMB generation might be isotropic statistically, there still exists some non-isotropic features in a single realization. The smooth bump that is observed in the maximum log-likelihood curve for all three spaces (figures 4.3, 4.5, 4.7) occurs when the diameter of the observable Universe $2\chi_{\rm LSS}$ increases to reach the size of the fundamental domain. What is occurring in this region of the parameters, is an alignment of our anisotropic model to some non-isotropic features in the single realization of CMB map that we observe. When a theory has a small $|\Omega_k|$ the fundamental domain is quite large compared to the size of the observable Universe, as such the theory predicts that the observable Universe is mostly isotropic with no correlation features in the theoretical correlation matrix, like that in igure 2.1. As $|\Omega_k|$ becomes larger the distance between the boundary and the horizon narrows, this increases the correlation pattern between different pixels in our theory. This increase occurs gradually, starting with very weak and few large scale correlation patterns. It seems that such weak patterns are always able to adjust to some features in our CMB map leading to a slight increase in the maximum likelihood value. I.e as the theory tends to develop some anisotropic correlations, there exists an orientation

that fits specific features of the CMB map more precisely than a model with no anisotropic correlation features to it.

There is a limit to this increase in the maximum likelihood value. As the fundamental domain becomes smaller, the complexity of the correlations in the theory increases. This creates the need for too many features to be aligned in the CMB map. Ultimately this hampers the maximum likelihood value, because one feature in the map may align well with the theory, where as the rest will not, this causes an overall decrease in the maximum likelihood value as $|\Omega_k|$ gets larger. This is the reason why most of this tail region is below the more smooth region as in the smooth region the observable Universe is more isotropic and as such there are no specific correlations to align the features with. The maximum likelihood curve, in the tail region is quite non-monotonic. This is expected and is attributed to the alignment of the the features in the CMB and our theory's correlation patterns. In the more isotropic region there is very little in the theory to restrict the alignment, leading to a smooth like curve. In the tail region, the change in the correlation patterns from Ω_k to Ω_k can be quite severe. Some models may have a certain set of correlations patterns in them that fits features on the CMB sky better than their neighbors, as such they will have a larger maximum likelihood value, and leads to the disjointed nature of the tail region.

The results that we obtained are quite similar to those obtained in the investigation done by the *Planck* team [Planck Collaboration et al. 2013b]. From their data they also observed a small increase in the maximum likelihood at and around when the horizon is near the boundary of the fundamental domain. In their investigation they marginalized over all likelihood values and observed that the bump disappeared [Planck Collaboration et al. 2013b]. They also ran a test on a randomly generated map from a topological model with a given Ω_k to examine the effect on the likelihood curve. In this case there is a noticeable increase in the maximum likelihood value at the Ω_k of the model. This increase remains strong even after the marginalisation over the orientation of the model to the map.

We also obtained a marginalized log-likelihood run for space-I only which can be seen in figure 4.8. This was done along the parameter degeneracy line and for the same Ω_k sampling as for space-I. The bump is now significantly reduced to just $\Delta \ln \mathcal{L} = 1.3$, well within the range of variance between models which follows what was observed by the *Planck* team. The *Planck* team also examined the maximum likelihood curve for a randomly generated map based on a purely isotropic model. They found that even for the isotropic model this bump is still present [Planck Collaboration et al. 2013b]. This indicates that this bump is not due to a specific topological model.

As an additional test we also obtained a run for the likelihood values over the same Ω_k samplings, but with Ω_Λ held constant. The maximum log-likelihood curves for the three spaces are, figure 4.9 for space-I, figure 4.11 for space-O,

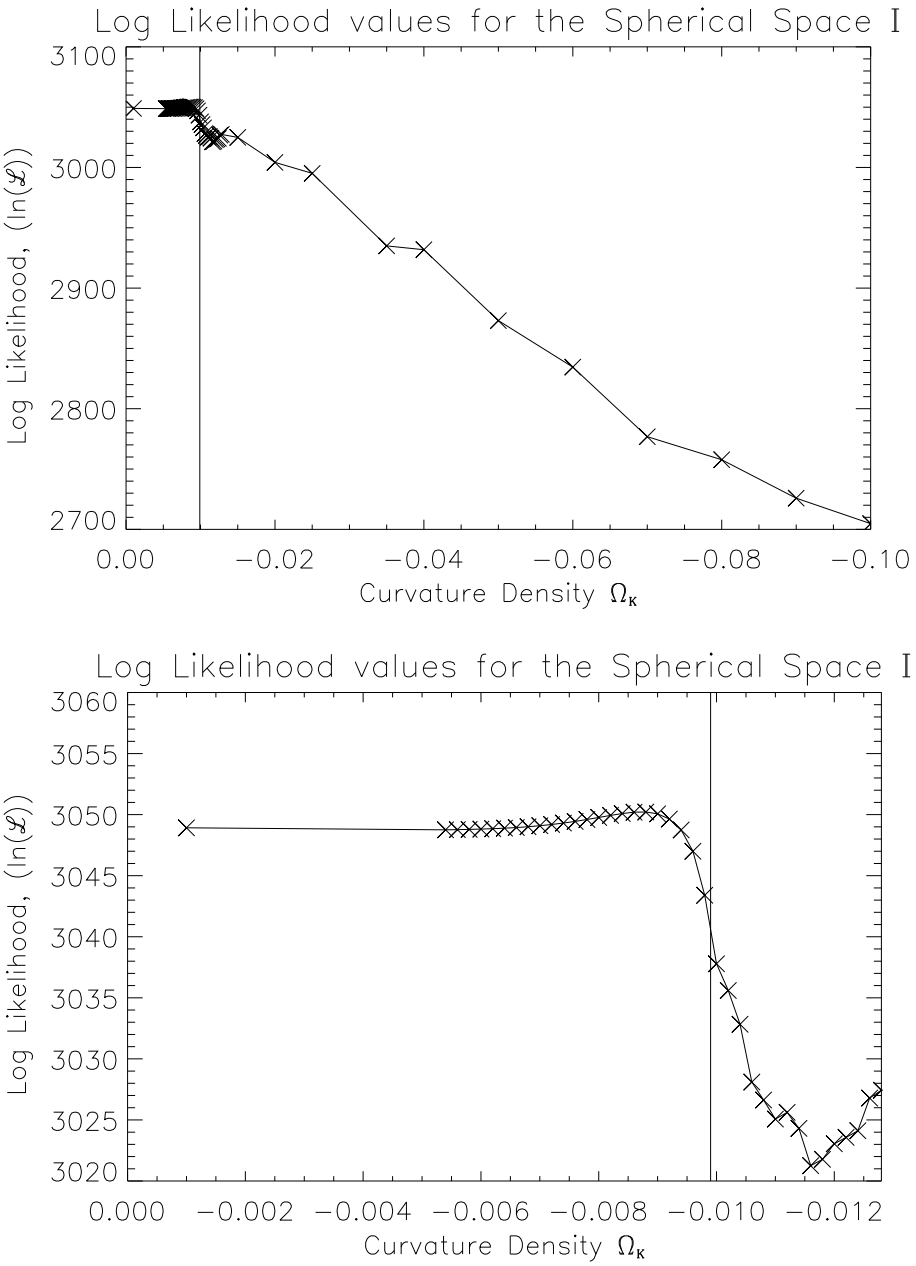

Figure 4.8: Marginalized log-likelihood over rotation, for a sampling of Ω_k over the inscribed region of the spherical multiconnected space-I. The vertical line corresponds to the Ω_k value when the horizon corresponds to the inscribed sphere of the multiconnected domain.

and figure 4.10 for space-T. They all have the same features as in the previous cases, the smooth small $|\Omega_k|$ region, the bump which occurs when the horizon first touches the boundary of the space and the disjointed, non-monotonically decreasing tail region. This indicates that the features that we are observing in the likelihood curve are not model dependant and do not demonstrate a detection of a particular multiconnected topology.

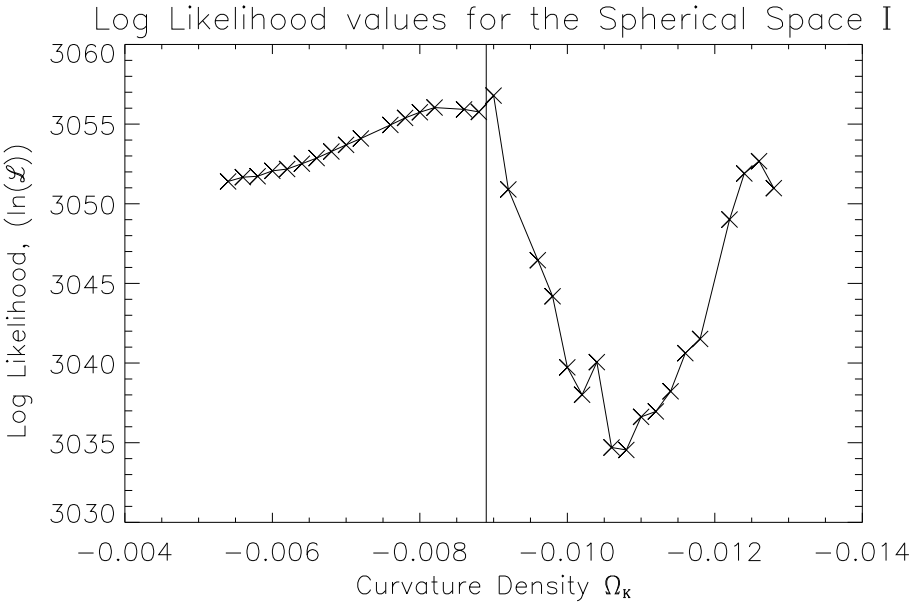

Figure 4.9: Maximum log-likelihood for the spherical multiconnected space-I as the function of Ω_k, holding Ω_Λ constant. The vertical line is the value of Ω_k when the horizon first touches the boundary of the fundamental domain.

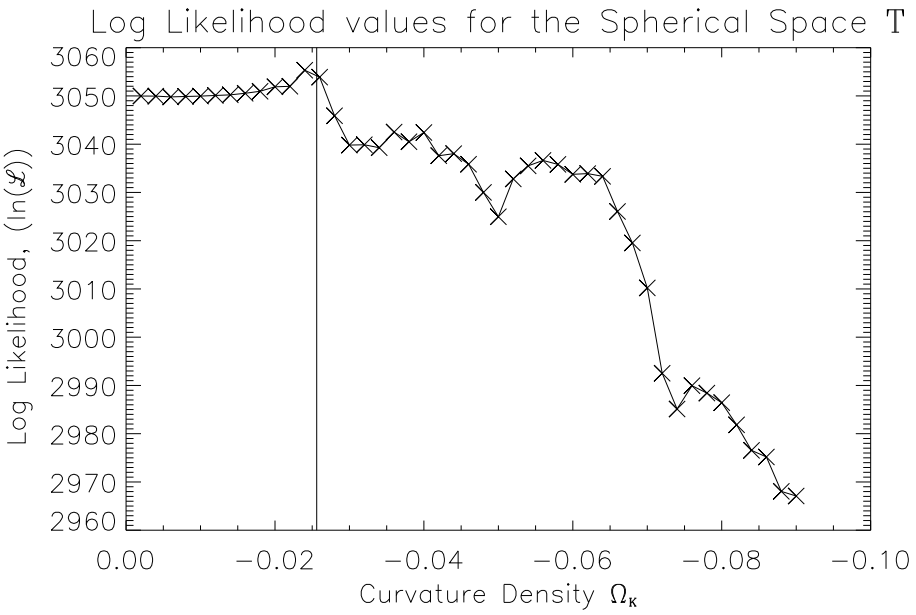

Figure 4.10: Maximum log-likelihood for the spherical multiconnected space-T as the function of Ω_k, holding Ω_Λ constant. The vertical line is the value of Ω_k when the horizon first touches the boundary of the fundamental domain.

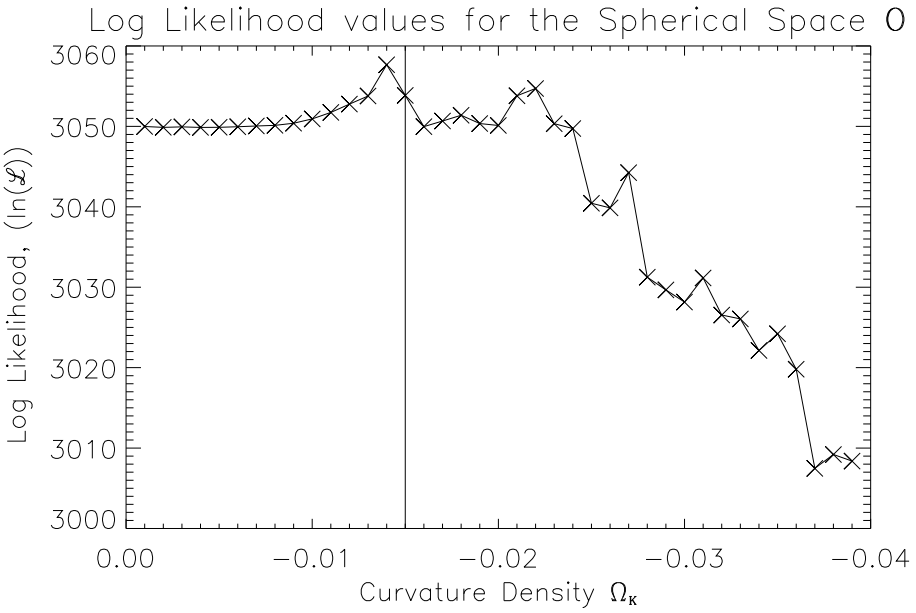

Figure 4.11: Maximum log-likelihood for the spherical multiconnected space-O as the function of Ω_k, holding Ω_Λ constant. The vertical line is the value of Ω_k when the horizon first touches the boundary of the fundamental domain.

4.3 The effect of the Mask

After the re-binning that is done to obtain the data map at $N_{\text{side}} = 16$ (section 3.1) some of the pixels that are near the galactic plane can be quite hot. The pixels in this region have a large variance when compared to the pixels that are in the rest of the map, due to the point source masking, figure 3.1. As such we do not trust the temperature values of these pixels in this region, therefore they are masked out for the analysis.

We use a very conservative mask, that is the mask which is in figure 4.12 called our analysis mask. This mask consists of two parts. When we re-bin the mask to $N_{\text{side}} = 16$ from the point source mask at $N_{\text{side}} = 512$, we require that for a pixel to be unmasked no less than 70% of its sub-pixels be unmasked. The final mask for this condition is shown in figure 4.13. The 70% criteria was chosen as it provides an even layer of masked pixels around the galactic bulge which is corrupted after smoothing. The second part of this mask is a band mask of the galactic plane which is a 20° band from the galactic equator. Both these conditions together provide the mask that we use in our analysis.

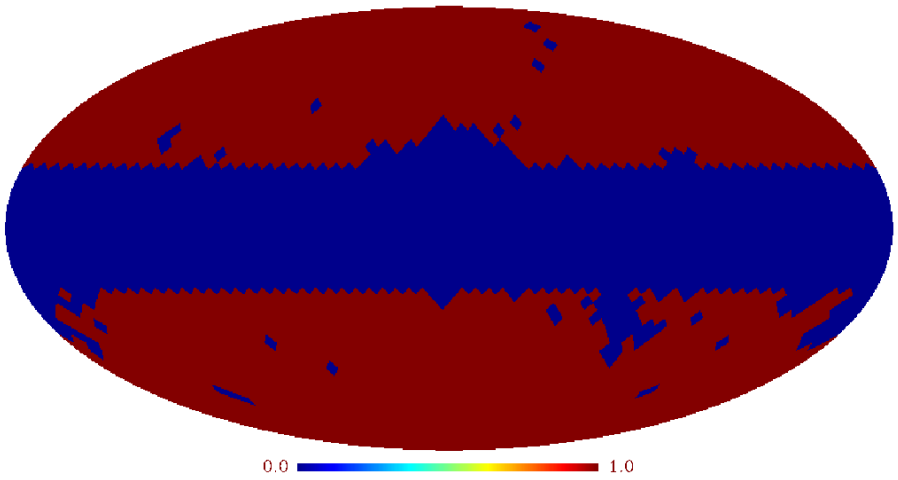

Figure 4.12: The 70% criterion mask with the 20° band mask. This is the analysis mask that is used in the determination of the maximum likelihood value in our main results.

The choice of mask is important. Masking too much or too little can seriously affect the maximum likelihood curve. A run using the same Ω_k sampling was done for space-I along the parameter degeneracy line, but with a mask without the 20° band from the galactic equator, called the 70% criterion mask, the resulting curve in figure 4.15. The maximum log-likelihood curve figure 4.15 shows a $\Delta \ln \mathcal{L} = 14.6$, which is twice more than the value when using the analysis mask. Care has to be taken because as stated in section 4.2 the model's correlations do

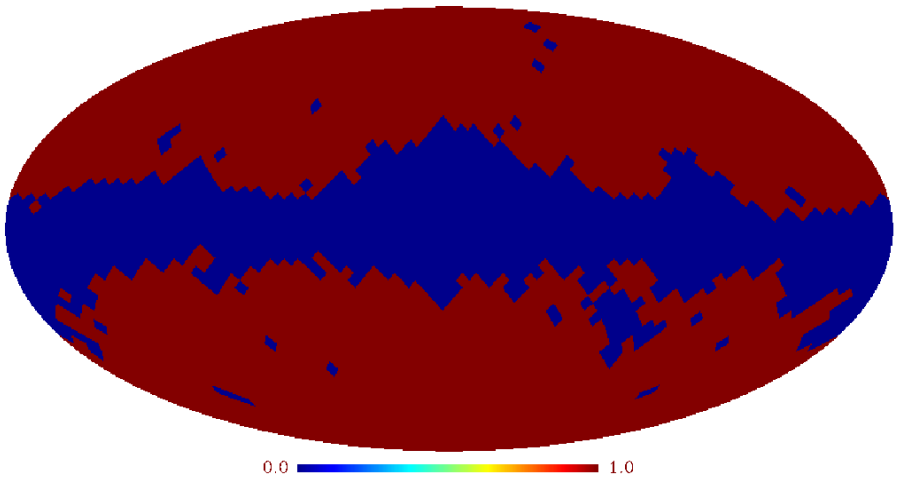

Figure 4.13: The 70% criterion mask.

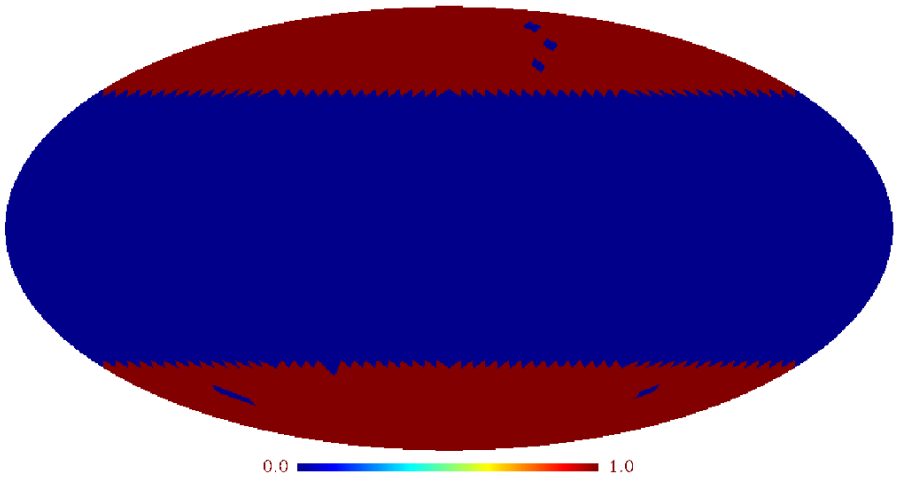

Figure 4.14: The 70% criterion mask with the 45° band mask.

align themselves to features in the CMB map causing an increase in the maximum likelihood value. The difference between the analysis mask and the 70% criterion mask is that we unmasked pixels close to the galactic plane. It seams that these temperature pixels aid in the alignment with the correlation patterns predicted by the model at the Ω_k corresponding to the bump, increasing the maximum likelihood value. These pixels are close to the galactic plane and as previously stated retain some corruption from the galactic plane, this is why we use the analysis mask for our main results. We have a run for space-I using the 70% criterion mask where Ω_Λ is held constant the resulting curve is figure 4.16.

In the tail section of the likelihood curve in figure 4.9, there is a large increase of the maximum likelihood value around $\Omega_k = -0.0126$, this is significantly reduced when using the 70% criterion mask, indicating that we actually unmasked some features that make the map more restrictive in the alignment, than when we ran with the analysis mask.

What if the mask is too large? Another run was done on space-I, but we increased the band mask from 20° to 45° seen in figure 4.14. Unfortunately due to the loss of pixels the number of modes had to be reduced to 437. As can be seen in figure 4.17 the value of the likelihood changed but not the characteristic features of the curve that we have seen in the other likelihood runs. Instead of a bump we have the steady increase to where the bump should be, but instead of decreasing, the maximum likelihood keeps increasing, though retaining the disjointed nature that is expected within this tail region. By reducing the sky to such a small section we have reduced the restrictiveness of the map. When the model's correlations become more complex they are able to fit the features that are retained in these smaller sections of the sky. Therefore when the map is less restrictive the more complex correlation patterns in the model can then fit the rest of the features in the data more easily, providing an overall plateaux like nature to the maximum likelihood curve in the tail region.

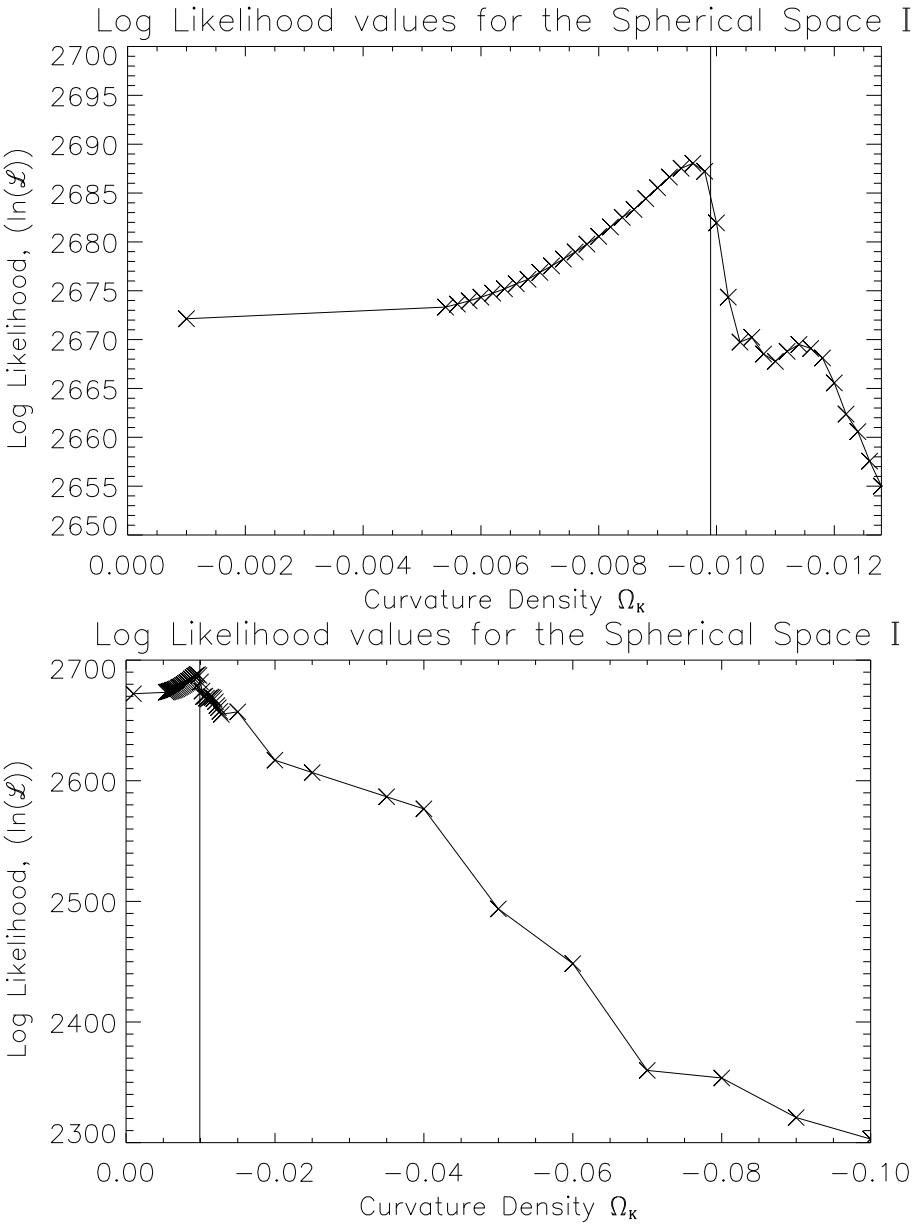

Figure 4.15: Maximum log-likelihood for the spherical multiconnected space-I as the function of Ω_k varying along the degeneracy line. Using the 70% criterion mask. The vertical line is the value of Ω_k when the horizon first touches the boundary of the space.

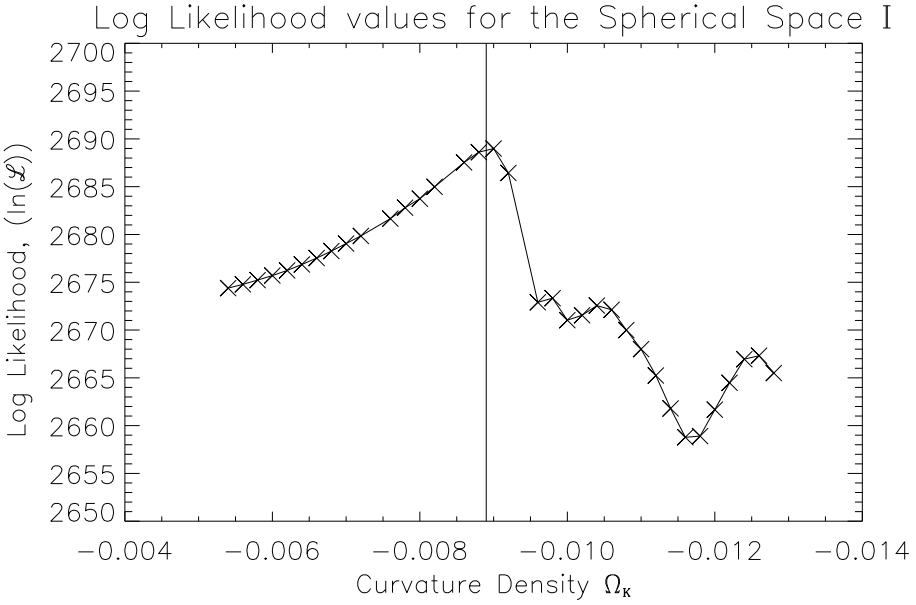

Figure 4.16: Maximum log-likelihood for the spherical multiconnected space-I as the function of Ω_k, holding Ω_Λ constant. Using the 70% criterion mask. The vertical line is the value of Ω_k when the horizon first touches the boundary of the space.

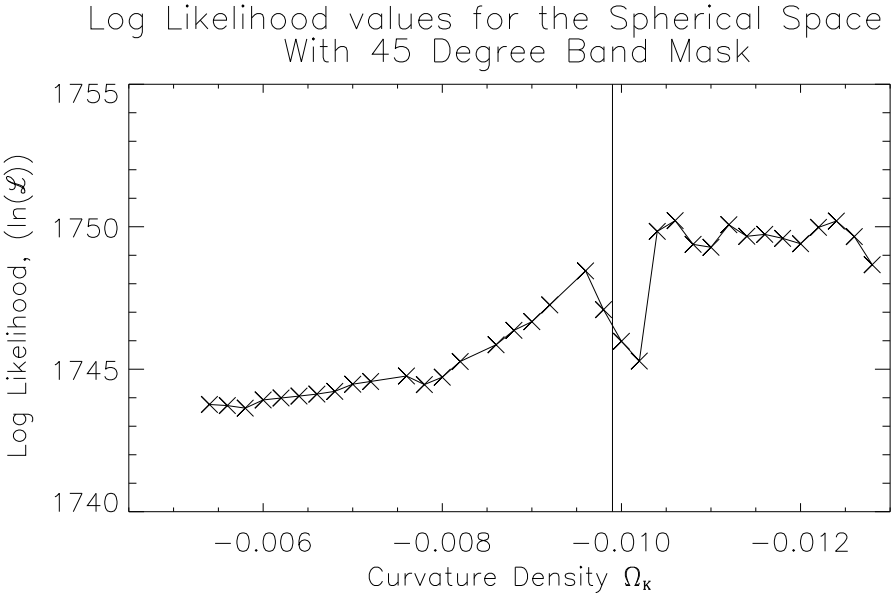

Figure 4.17: Maximum log-likelihood for the spherical multiconnected space-I as the function of Ω_k varying along the degeneracy line. Using the 45° band mask. The vertical line is the value of Ω_k when the horizon first touches the boundary of the space.

Chapter 5

Conclusion

The shape of the Universe is what has been investigated. Multiconnected spaces are of particular interest because they provide a compactification of the Universe, while retaining the constant universal curvature that fits our observations so well. We investigated three spherical multiconnected spaces called, space-I, space-T and space-O. The investigation of closed geometry was done because the latest observations from WMAP determine that the Ω_k value is more closed than open. The measured value from WMAP is $\Omega_k = -0.037^{+0.044}_{-0.042}$. These three spaces were chosen out of the possible five multiconnected spaces for a positive curvature Universe corresponding to a universal cover of $\mathbb{S}^3$, as the other two being the prism and lens spaces are infinite in number. The chosen spaces are also more "equally proportioned" without the more drastic anisotropy of the prism and lensed spaces.

A sampling over Ω_k in the region where the last scattering horizon intersects with the boundary of the space was chosen for each multiconnected space. For each Ω_k a maximum likelihood value was obtained, this involved determining the best amplitude at the best orientation of our model in relation to the data. All the Ω_k together form what is called the maximum likelihood curve of the model.

There are three prominent features to this curve, the smooth region up to when the horizon intersects with the boundary of the space, the bump at the intersection point and the disjointed non-monotonically decreasing likelihood value after the intersection. The bump occurs at the location when Ω_k is such that the horizon intersects with the boundary of the space. This bump is in all the maximum likelihood curves for all three spaces, whether it be on the parameter degeneracy line or for Ω_Λ held constant. This is in agreement with what was observed by the *Planck* investigation team during their topological investigation from the *Planck* data [Planck Collaboration et al. 2013b]. The bump is not a detection of a topological signal, but is due to an alignment of the model to some features that are contained in our CMB map. The disjointed non-monotonically decreasing likelihood tail region is when the horizon becomes larger with respect

to the distance to the boundary of the space. The correlation patterns in this tail region becomes more complex and can change significantly from Ω_k to Ω_k. This results in the deceasing disjointed nature of the likelihood curve in the tail region. The smooth section of the likelihood curve is due to the lack of complex correlations in the model. As such there is no large great change from Ω_k to Ω_k only a slight gradual increase in the existing correlations, which leads to the smooth nature in this regime.

The choice of mask is very important in the analysis. We obtained two maximum likelihood curves for the space-I, one using a small more liberal mask and the other using a larger more conservative mask. This difference between the two masks showed a change in the maximum likelihood curve. For the smaller more liberal mask the $\Delta \ln \mathcal{L}$ at the bump increased around two times the $\Delta \ln \mathcal{L}$ from our analysis mask. We also saw by decreasing the amount of masked sky a significant peak that existed in the tail region using the analysis mask disappeared. This indicates that the analysis mask cuts some features in the map reducing the restrictiveness of the fit. This allowed a model with a more complex correlation pattern to align more easily and increased its maximum likelihood value. For the larger more conservative mask the maximum likelihood in the tail region was no longer decreasing in the disjointed manner but rather plateaued in the same disjointed manner. This again is attributed to the reduction of restrictions that occurs when we remove large sections of the map. All likelihood runs for the three different masks showed the same basic features a smooth start, a bump and a disjointed tail, all properties attributed to the alignment of the changing correlations to the CMB map.

A final test was done on space-I where rather than determining the best orientation for a given Ω_k, we marginalized over the orientation space of the model. The likelihood curve's bump was significantly reduced, down to the level of acceptable variance between models. The *Planck* collaboration did an investigation using a random realization for a given topological model and determined, that even when marginalized a likelihood bump at the Ω_k of the model remains significantly present in the curve [Planck Collaboration et al. 2013b]. The *Planck* collaboration also did an investigation of a random realization of the sky for a given isotropic model and the resulting likelihood curve still showed this bump. This is not a detection of a specific multiconnected topology but of an alignment to some features in the CMB sky which could be the result of the fact that this is a single realization and as such it is expected to contain some features in it.

The next step in this investigation would be the addition of a prior to the likelihood value, such as the higher frequency l likelihood fit. Further investigation into which features are being aligned and their origin, could be of benefit in the deeper understanding of the origin of these features.

Bibliography

Alpher, R. & Herman, R. (1948). Evolution of the Universe. *Nature*, *162*, 774–775.

Aurich, R., Lustig, S., Steiner, F., & Then, H. (2007). Cosmic microwave background alignment in multi-connected universes. *Classical and Quantum Gravity*, *24*, 1879–1894.

Beutler, F., Blake, C., Colless, M., Jones, D. H., Staveley-Smith, L., Campbell, L., et al. (2011). The 6dF Galaxy Survey: baryon acoustic oscillations and the local Hubble constant. *MNRAS*, *416*, 3017–3032.

Boggess, N. W., Mather, J. C., Weiss, R., Bennett, C. L., Cheng, E. S., Dwek, E., et al. (1992). The COBE mission - Its design and performance two years after launch. *ApJ*, *397*, 420–429.

Bond, J. R., Pogosyan, D., & Souradeep, T. (1998). Computing CMB anisotropy in compact hyperbolic spaces. *Classical and Quantum Gravity*, *15*, 2671–2687.

Bond, J. R., Pogosyan, D., & Souradeep, T. (2000a). CMB anisotropy in compact hyperbolic universes. I. Computing correlation functions. *Physical Review D*, *62*(4), 043005.

Bond, J. R., Pogosyan, D., & Souradeep, T. (2000b). CMB anisotropy in compact hyperbolic universes. II. COBE maps and limits. *Physical Review D*, *62*(4), 043006.

Boughn, S. P. & Jahoda, K. (1993). A comparison of the cosmic microwave and cosmic X-ray backgrounds - Constraints on local sources of the fluctuations observed by COBE. *Astrophysical Journal, Part 2 - Letters*, *412*, L1–L4.

Carroll, S. M. (2004). *An Introduction to General Relativity Spacetime an Geometry*. Addison Wesley.

Cornish, N. J., Spergel, D. N., & Starkman, G. D. (1998). Circles in the sky: finding topology with the microwave background radiation. *Classical and Quantum Gravity*, *15*, 2657–2670.

de Bernardis, P., Ade, P. A. R., Artusa, R., Bock, J. J., Boscaleri, A., Crill, B. P., et al. (1999). Mapping the CMB sky: THE BOOMERanG experiment. *New Astronomy Reviews*, *43*, 289–296.

Dicke, R. H., Peebles, P. J. E., Roll, P. G., & Wilkinson, D. T. (1965). Cosmic Black-Body Radiation. *ApJ*, *142*, 414–419.

Fixsen, D. J. (2009). The Temperature of the Cosmic Microwave Background. *ApJ*, *707*, 916–920.

Fixsen, D. J., Cheng, E. S., Gales, J. M., Mather, J. C., Shafer, R. A., & Wright, E. L. (1996). The Cosmic Microwave Background Spectrum from the Full COBE FIRAS Data Set. *ApJ*, *473*, 576.

Gamow, G. (1948). The Evolution of the Universe. *Nature*, *162*, 680–682.

Gausmann, E., Lehoucq, R., Luminet, J.-P., Uzan, J.-P., & Weeks, J. (2001). Topological lensing in spherical spaces. *Classical and Quantum Gravity*, *18*, 5155–5186.

Górski, K. M., Hivon, E., Banday, A. J., Wandelt, B. D., Hansen, F. K., Reinecke, M., & Bartelmann, M. (2005). HEALPix: A Framework for High-Resolution Discretization and Fast Analysis of Data Distributed on the Sphere. *ApJ*, *622*, 759–771. http://healpix.sourceforge.net/documentation.php.

Hinshaw, G., Larson, D., Komatsu, E., Spergel, D. N., Bennett, C. L., Dunkley, J., et al. (2012). Nine-Year Wilkinson Microwave Anisotropy Probe (WMAP) Observations: Cosmological Parameter Results. *ArXiv e-prints*.

Hu, W. (1996). Concepts in CMB Anisotropy Formation. *470*, 207.

Hu, W. & Dodelson, S. (2002). Cosmic Microwave Background Anisotropies. *ARA&A*, *40*, 171–216.

Hu, W. & White, M. (1996). Acoustic Signatures in the Cosmic Microwave Background. *ApJ*, *471*, 30.

Hubble, E. (1936). Effects of Red Shifts on the Distribution of Nebulae. *Astrophysical Journal*, *84*, 517.

Lehoucq, R., Lachieze-Rey, M., & Luminet, J. P. (1996). Cosmic crystallography. *Astronomy and Astrophysics*, *313*, 339–346.

Lehoucq, R., Weeks, J., Uzan, J.-P., Gausmann, E., & Luminet, J.-P. (2002). Eigenmodes of three-dimensional spherical spaces and their application to cosmology. *Classical and Quantum Gravity*, *19*, 4683–4708.

Luminet, J.-P. (2006). The Shape of Space after WMAP data. *Brazilian Journal of Physics*, *36*, 107–114.

Luminet, J.-P., Weeks, J. R., Riazuelo, A., Lehoucq, R., & Uzan, J.-P. (2003). Dodecahedral space topology as an explanation for weak wide-angle temperature correlations in the cosmic microwave background. *Nature*, *425*, 593–595.

MacTavish, C., Ade, P., Bock, J., Bond, J., Borrill, J., et al. (2006). Cosmological Parameters from the 2003 flight of Boomerang. *Astrophysical Journal*, *647*, 799–812.

NASA/WMAP Science Team (2010). Online: `http://map.gsfc.nasa.gov/mission/observatory_spec.html`.

Partridge, R. (1988). The angular distribution of the cosmic background radiation. *Reports on Progress in Physics*, *51*(7), 647–705.

Penzias, A. A. & Wilson, R. W. (1965). A Measurement of Excess Antenna Temperature at 4080 Mc/s. *ApJ*, *142*, 419–421.

Planck Collaboration, Ade, P. A. R., Aghanim, N., Armitage-Caplan, C., Arnaud, M., Ashdown, M., Atrio-Barandela, F., et al. (2013a). Planck 2013 results. I. Overview of products and scientific results. *ArXiv e-prints*.

Planck Collaboration, Ade, P. A. R., Aghanim, N., Armitage-Caplan, C., Arnaud, M., Ashdown, M., Atrio-Barandela, F., et al. (2013b). Planck 2013 results. XXVI. Background geometry and topology of the Universe. *ArXiv e-prints*.

Press, W., Teukolsky, S., Vetterling, W., & Flannery, B. (2001). *Numerical Recipies in Fortran 77 The Art of Scientific Computing* (Second ed.). Press Syndicate of the University of Cambridge.

Rabii, B., Winant, C. D., Collins, J. S., Lee, A. T., Richards, P. L., et al. (2006). MAXIMA: A balloon-borne cosmic microwave background anisotropy experiment. *Review of Scientific Instruments*, *77*(7), 071101.

Sachs, R. K. & Wolfe, A. M. (1967). Perturbations of a Cosmological Model and Angular Variations of the Microwave Background. *Astrophysical Journal*, *147*, 73.

Seager, S., Sasselov, D. D., & Scott, D. (2000). How Exactly Did the Universe Become Neutral? *The Astrophysical Journal Supplement Series*, *128*, 407–430.

Smoot, G., Bennett, C., Weber, R., Maruschak, J., Ratliff, R., Janssen, M., et al. (1990). COBE Differential Microwave Radiometers - Instrument design and implementation. *ApJ*, *360*, 685–695.

Smoot, G. F., Bennett, C. L., Kogut, A., Wright, E. L., Aymon, J., Boggess, N. W., et al. (1992). Structure in the COBE differential microwave radiometer first-year maps. *ApJ Let.*, *396*, L1–L5.

Smoot, G. F., Gorenstein, M. V., & Muller, R. A. (1977). Detection of anisotropy in the cosmic blackbody radiation. *Physical Review Letters*, *39*, 898–901.

Sokolov, D. D. & Shvartsman, V. F. (1974). An estimate of the size of the universe from a topological point of view. *JETP*, *39*, 196.

Spergel, D. N., Verde, L., Peiris, H. V., Komatsu, E., Nolta, M. R., Bennett, C. L., et al. (2003). First-Year Wilkinson Microwave Anisotropy Probe (WMAP) Observations: Determination of Cosmological Parameters. *The Astrophysical Journal Supplement Series*, *148*, 175–194.

Szapudi, I., Prunet, S., Pogosyan, D., Szalay, A. S., & Bond, J. R. (2001). Fast Cosmic Microwave Background Analyses via Correlation Functions. *The Astrophysical Journal*, *548*, L115–L118.

The Planck Collaboration (2005). PLANCK The Scientific Programme. Online: `http://www.rssd.esa.int/SA/PLANCK/docs/Bluebook-ESA-SCI(2005)1\_V2.pdf`, Accessed August 2013.

Uzan, J.-P., Lehoucq, R., & Luminet, J.-P. (1999). A new crystallographic method for detecting space topology. *Astronomy and Astrophysics*, *351*, 766–774.

Weeks, J. R. (1998). Reconstructing the global topology of the universe from the cosmic microwave background. *Classical and Quantum Gravity*, *15*, 2599–2604.

White, M., Scott, D., & Silk, J. (1994). Anisotropies in the Cosmic Microwave Background. *ARA&A*, *32*, 319–370.